

Opto-electronic Characterization of Perovskite Solar Cells

Arman Mahboubi Soufiani

A THESIS IN FULFILMENT OF THE REQUIREMENTS FOR THE DEGREE OF
DOCTOR OF PHILOSOPHY



School of Photovoltaic and Renewable Energy Engineering

Faculty of Engineering

The University of New South Wales

May 2017

THE UNIVERSITY OF NEW SOUTH WALES
Thesis/Dissertation Sheet

Surname or Family name: **Mahboubi Soufiani**

First name: **Arman**

Other name/s:

Abbreviation for degree as given in the University calendar: **PhD**

School: **School of Photovoltaic and Renewable Energy Engineering** Faculty: **Engineering**

Title: **Opto-electronic Characterization of Perovskite Solar Cells**

Abstract 350 words maximum:

Since the first report, in 2009, on solar cells based on organic-inorganic metal halide perovskites as the active light absorber, intensive research on performance improvement of these types of solar cells has led to a dramatic rise in their power conversion efficiencies from 3-4% to the recently certified efficiency of 22.1% for laboratory-scale devices. Researchers from various fields of physics, chemistry, material science and engineering have been attempting to understand the opto-electronic properties of these materials to (i) develop new fabrication techniques of the perovskite layer to optimise their photovoltaic characteristics; (ii) synthesize stable and energetically appropriate carrier selective contacts; (iii) unravel the underlying reasons of the current-voltage hysteresis in these solar cells; and (iv) overcome their long-term operational stability and to lessen the toxicity issues of the lead component.

In two separate sections, this thesis is dedicated to understand both the optical characteristics of most studied photovoltaic perovskites, with the focus being on the exciton binding energy influencing light absorption, and also to develop fast, reliable and standard characterization technique for electrical examination of the corresponding solar cells which is based on the luminescence properties of perovskites. The absorption spectrum of these materials with and without the inclusion of excitonic effects is elaborated. The experimental values for the binding energies extracted from temperature-dependent absorption spectra of high-quality $\text{CH}_3\text{NH}_3\text{PbI}_3$ and $\text{CH}_3\text{NH}_3\text{PbBr}_3$ thin films are compared with theory. In the theory employed, the interaction of electrons and holes with an effective longitudinal optical phonon was considered for the first time in these semiconductors to better estimate the theoretical values. Good agreement between theory and experiments was shown to be achievable.

Performance characterization of perovskite solar cells was initiated in this thesis by exploration of the generalized Planck's radiation law for planar structured devices both under light- and electrical-bias conditions (photoluminescence, PL, and electroluminescence, EL, respectively). In hysteresis affected devices, light-soaking was found to be an essential prerequisite in order to be able to correlate luminescence intensity and the device internal voltage. Long-term behaviour of planar solar cells with $\text{CH}_3\text{NH}_3\text{PbI}_3$ active layer was investigated using full device EL imaging and it was realized that interfacial deterioration even when the device is stored in dark under glovebox condition (devices only used for light current-voltage measurements) is the critical factor suppressing the fill factor.

In the last section, using PL and EL imaging, the immediate response and long-term electrical evolution of the perovskite bulk and compact TiO_2 /perovskite and perovskite/Spiro-OMeTAD interfaces after the initial short and prolonged selective illumination of the device is elaborated. Perovskite structure buckling over time resulting in the interfacial decoupling at the titanium dioxide/perovskite is demonstrated and the associated mechanism is discussed in detail. The latter is explained by the intrinsic ion migration feature of $\text{CH}_3\text{NH}_3\text{PbI}_3$ perovskite which is influenced principally due to the change in the internal electric field of the device.

Declaration relating to disposition of project thesis/dissertation

I hereby grant to the University of New South Wales or its agents the right to archive and to make available my thesis or dissertation in whole or in part in the University libraries in all forms of media, now or here after known, subject to the provisions of the Copyright Act 1968. I retain all property rights, such as patent rights. I also retain the right to use in future works (such as articles or books) all or part of this thesis or dissertation. I also authorise University Microfilms to use the 350 word abstract of my thesis in Dissertation Abstracts International (this is applicable to doctoral theses only).

.....
Signature

.....
Witness Signature

.....
Date

The University recognises that there may be exceptional circumstances requiring restrictions on copying or conditions on use. Requests for restriction for a period of up to 2 years must be made in writing. Requests for a longer period of restriction may be considered in exceptional circumstances and require the approval of the Dean of Graduate Research.

FOR OFFICE USE ONLY

Date of completion of requirements for Award:

COPYRIGHT STATEMENT

'I hereby grant the University of New South Wales or its agents the right to archive and to make available my thesis or dissertation in whole or part in the University libraries in all forms of media, now or here after known, subject to the provisions of the Copyright Act 1968. I retain all proprietary rights, such as patent rights. I also retain the right to use in future works (such as articles or books) all or part of this thesis or dissertation.

I also authorise University Microfilms to use the 350 word abstract of my thesis in Dissertation Abstract International (this is applicable to doctoral theses only).

I have either used no substantial portions of copyright material in my thesis or I have obtained permission to use copyright material; where permission has not been granted I have applied/will apply for a partial restriction of the digital copy of my thesis or dissertation.'

Signed

Date

AUTHENTICITY STATEMENT

'I certify that the Library deposit digital copy is a direct equivalent of the final officially approved version of my thesis. No emendation of content has occurred and if there are any minor variations in formatting, they are the result of the conversion to digital format.'

Signed

Date

ORIGINALITY STATEMENT

'I hereby declare that this submission is my own work and to the best of my knowledge it contains no materials previously published or written by another person, or substantial proportions of material which have been accepted for the award of any other degree or diploma at UNSW or any other educational institution, except where due acknowledgement is made in the thesis. Any contribution made to the research by others, with whom I have worked at UNSW or elsewhere, is explicitly acknowledged in the thesis. I also declare that the intellectual content of this thesis is the product of my own work, except to the extent that assistance from others in the project's design and conception or in style, presentation and linguistic expression is acknowledged.'

Signed

Date

Acknowledgements

Below, I would like to gratefully and humbly express my gratitude to those who greatly contributed to the journey that led to the accomplishment of an important step in my career life but not in the traditional form.

I start my acknowledgment being firstly and deeply grateful to my lovely parents, Raihan and Yousof, who dedicated their life to grow and educate me as a person who aims to be useful both locally and globally and to love surrounding people unconditionally.

The enthusiasm to start and fulfil PhD study could not happen without cultivating the seed of passion for research continuously throughout my educational life. So, I would like to thank all my teachers and lecturers from my very first level teacher at the Isfahan University of Technology primary school, Mrs. Goli, to my last lecturer of the last course I took with Dr. Alison Lennon at the University of New South Wales.

Thanks to an intellectual and supportive friend, Omid Doostmohammadi, and also Masoud Salehi and Dr. Abas Mohsenzadeh who encouraged me to move out of my comfort zone and follow my passion for my PhD.

The three and half years of my PhD journey began with my first contact with Dr. Richard Corkish who warmly and kindly, as has always been since then, brought me in touch with Prof. Gavin Conibeer who accepted and supported me as his student. I am very much thankful to both of them for giving me this opportunity. Being directly supervised by Prof. Gavin Conibeer and Dr. Murad Tayebjee during the first year of my PhD, while working on molecular organic semiconductors, I learnt a lot from both. I am humbly thankful to both of them for their guidance and insightful discussions. My special thanks goes to Murad to whom, with his generosity, kindness and great programing skills helped me to develop various skills such as persistence in research and also coding.

I will never forget my first meeting with Prof. Martin Green in the first month of my PhD during which I understood just a fraction of his scientific points. A year after that, I joined his freshly established perovskite research group after having my second meeting with him when he told me about a great potential of perovskite photovoltaics. Since then he has been and will be a great inspiration in my academic life. With a very kind personality, his enthusiasm and eagerness for research is absolutely amazing. Apart from his expected great scientific support and insights he implicitly taught me two important lessons which I will never forget in my academic and personal life. The first is patience, a key to success and second, is the continuous learning process of life. I would like to thank Dr. Anita Ho-Baillie, another supervisor of mine, for her kindness, support and technical contribution to my research.

Special thanks to my lovely friends, Arastoo Teymouri, Hamid Arandiyan, Alireza Gerami, Sara Mesgari, Maryam Hashemi, Fatemeh Kamali, Sina Moradi for making the tea breaks so much fun and refreshing and all their support.

I would like to thank Dr. Craig Johnson, with his kind and generous personality, who listened to my concerns during some stressful times of my PhD and helped me go through it smoothly.

Special thanks to Dr. Ziv Hameiri, a kind and generous person, a good friend and colleague who I got familiar with during the second year of my PhD. Both of us being Middle East and spending a lot of time on research, I had joyful times with him during weekend lunches, dinners, and also when playing volleyball at the beach. Our sporadic frictions in research and other topics were also fun.

I wish to say a great thanks to all the perovskite group members at the University of New South Wales with whom I had cheerful times in particular during the out-of-school perovskite gatherings for dinner. Dr. Jae Song Yun, who was not only a colleague but also a good friend having lots of fun time together, Dr. Yajie Jiang, a kind and helpful person, Rui Sheng, with

whom we were the first student members of the freshly established perovskite group at UNSW in 2014, Jincheol Kim and Qingshan Ma are those I could not miss naming.

Special thanks to Nitin Nampalli a kind and good friend who I discussed more than just work related subjects such as culture, politics and Persian poetry. Additional thanks for helping in formatting my thesis.

Thanks to many friends, colleagues, researchers and staff at SPREE for making the huge photovoltaic research centre at UNSW a vibrant and friendly place to work in: Anastasia Soeriyadi, Nancy Sharopeam, Joyce Ho, Robert Largent, Jill Lewis, Alan Yee, Nicholas Shaw, Dr. Bernhard Mitchell, Dr. Thorsten Trupke, Dr. Hamid Mehrvarz, Dr. Henner Kampwerth, Dr. Ivan Perez Wurfl, Dr. Robert Patterson, Dr. Binesh Puthen-Veettil, Dr. Mattias Juhl, Dr. Peter Reece, Dr. Hongze Xia, Dr. Michael Pollard, Oliver Kunz and Dr. Shujuan Huang.

Last but not least, my lovely and gorgeous parents, who are my heroes, and my two amazing brothers, Amir and Arash, who I missed so much their presence and their great sense of humour. They have been always a great support and source of love for me and encouragement for my challenge-loving attitude in life.

Abstract

Since the first report, in 2009, on solar cells based on organic-inorganic metal halide perovskites as the active light absorber, intensive research on performance improvement of these types of solar cells has led to a dramatic rise in their power conversion efficiencies from 3-4% (in 2009) to the recently certified efficiency of 22.1% for laboratory-scale devices. Researchers from various fields of physics, chemistry, material science and engineering have been attempting to understand the opto-electronic properties of these attractive crystalline semiconductors to (i) improve and develop new fabrication techniques of the perovskite layer so as to optimise their photovoltaic characteristics; (ii) develop stable and energetically appropriate charge carrier selective contacts; (iii) understand the underlying reasons of the current-voltage hysteresis in these solar cells; and (iv) overcome their long-term operational stability and to lessen the toxicity issues of the perovskite layer.

In two separate sections, this thesis is dedicated to the understanding of both the optical characteristics of most studied photovoltaic perovskite semiconductors, with the focus being on the exciton binding energy influencing light absorption, and also to develop fast, reliable and standard characterization technique for electrical examination of the corresponding solar cells which is based on the luminescence properties of perovskites. An attempt has been made to cover many of the reported binding energy values for polycrystalline perovskite thin films (methylammonium lead triiodide and tribromide) and further, the methods employed in the literature are discussed. The absorption spectrum of these materials with and without the inclusion of excitonic effects is discussed in detail. The experimental values for the binding energies extracted from temperature-dependent absorption spectra of high-quality thin films are compared with theory. In the theory employed, the interaction of electrons and holes with an effective optical phonon was considered for the first time in these semiconductors to better estimate the theoretical values for the binding energy. Good agreement between theory and experiments was shown to be achievable.

Performance characterization of perovskite solar cells was initiated in this thesis by exploration of the generalized Planck's radiation law for planar structured devices both under light- and electrical-bias conditions (photoluminescence and electroluminescence, respectively). In hysteresis affected devices, light-soaking was found to be an essential prerequisite in order to be able to correlate luminescence intensity and the device internal voltage. Long-term behaviour of planar solar cells with methylammonium lead triiodide active layer was investigated using full device electroluminescence imaging and it was realized that interfacial deterioration even when the device is stored in the dark under glovebox conditions (devices only used for light current-voltage measurements) is the critical factor suppressing the fill factor. The shortcoming of using titanium dioxide and Spiro-OMeTAD as electron and hole selective contacts was elucidated.

In the last section, using photoluminescence and electroluminescence imaging, the immediate response and long-term electrical evolution of the perovskite bulk and titanium dioxide/perovskite and perovskite/Spiro-OMeTAD interfaces after the initial short and prolonged selective illumination of the device is elaborated. Perovskite structure buckling over time resulting in the interfacial decoupling at the titanium dioxide/perovskite is demonstrated and the associated mechanism is discussed in detail. The latter is explained by the intrinsic ion migration feature of methylammonium lead triiodide perovskite which is influenced principally due to the change in the internal electric field of the device.

Table of Contents

Acknowledgements	i
Abstract	iv
Abbreviations and Symbols.....	viii
1 Introduction	1
1.1 Motivations and Significance	4
1.2 Thesis Outline.....	5
1.2.1 Exciton Binding Energy	5
1.2.2 Performance of Perovskite Solar Cells	6
2 Polaronic-Exciton Binding Energy in Methylammonium Lead Trihalide Polycrystalline Thin Films	8
2.1 Background.....	8
2.1.1 Excitons	8
2.1.2 Why Exciton Binding Energy is Important	12
2.2 Literature Review	13
2.2.1 Exciton binding Energy Values and Extraction Methods.....	13
2.2.2 Discussion about the Literature Values	18
2.3 Experimental Methods.....	23
2.3.1 Material Synthesis and Precursor Preparation	23
2.3.2 Sample Fabrication	24
2.3.3 Optical Measurement.....	24
2.4 Results and Discussion	25
2.4.1 Elliot Theory for Exciton Binding Energy Measurement.....	25
2.4.2 Assessment of the Excitonic Nature of the Absorption Band-edge.....	28
2.4.3 Carrier-phonon Interaction Consideration.....	31
2.4.4 Comparison of Theory with Experiment	38
3 Electro- and photo-luminescence Imaging of Perovskite Solar Cells	45
3.1 Background.....	45
3.2 Experimental Methods.....	46
3.2.1 Materials	46
3.2.2 Solar Cell Preparation.....	47
3.2.3 J-V Characterization	47
3.2.4 Steady-state Spectral Photoluminescence Measurement	48

3.2.5	Electroluminescence and Photoluminescence Imaging	48
3.3	Evaluating the Generalized Planck's Emission Law in Planar Structured Perovskite Solar Cells.....	48
3.3.1	Required Corrections to the Images	50
3.3.2	Photoluminescence Measurement.....	51
3.3.3	Electroluminescence Measurement.....	53
3.4	Luminescence Imaging as Fast Screening Technique of Layer Uniformity	54
3.5	Luminescence Imaging as Fast Screening Technique of Device Degradation in the Dark	62
4	Illumination-induced Immediate Response and Long-term Evolution of CH ₃ NH ₃ PbI ₃ Planar Perovskite Solar Cells.....	67
4.1	Background	67
4.2	Introduction.....	69
4.3	Experimental Methods	71
4.3.1	Materials	71
4.3.2	Solar Cell Preparation	71
4.3.3	J-V characterization	71
4.3.4	Electro- and photoluminescence Imaging.....	71
4.3.5	Transmission Microscopy Measurement	72
4.4	Regular Measurement Conditions and Procedures	72
4.5	Results and Discussion	73
4.5.1	Initial Effect of Light Current-Voltage Measurements	73
4.5.2	Long-term Impact of Light Current-Voltage Measurements	81
4.5.3	Impact of Light-Soaking at Open-circuit Condition	88
4.5.4	Cross-sectional TEM and EDS	93
4.6	Mechanistic Interpretation	96
4.6.1	Perovskite Degradation Assessment	96
4.6.2	Ionic Species Involved	98
4.6.3	Mechanism Description	99
5	Conclusions and Future Work.....	105
	List of Publications	111
	References.....	115

Abbreviations and Symbols

PV	Photovoltaic
PSC	Perovskite solar cell
OILHP	Organic-inorganic lead halide perovskite
CH₃NH₃PbI₃	Methylammonium lead triiodide perovskite
CH₃NH₃PbBr₃	Methylammonium lead tribromide perovskite
MA	Methylammonium cation
OD	Optical density
α	Absorption Coefficient
Ry₀	Exciton binding energy (effective Rydberg)
E_g	Semiconductor band gap
μ	Electron-hole reduced effective mass
ϵ_∞	Optical dielectric constant
ϵ_s	Static dielectric constant
k_b	Boltzmann constant
\hbar	Reduced Planck's constant
$m_{e,h}$	Electron or hole effective rigid (band) mass
J-V	Light current density-voltage
V_{oc}	Open-circuit voltage
J_{sc}	Short-circuit current density
FF	Fill factor
R_s	Series resistance
PL	Photoluminescence
EL	Electroluminescence
ETL	Electron transport layer
HTL	Hole transport layer
XRD	X-ray diffraction
TEM	Transmission electron microscopy
SEM	Scanning electron microscopy
c-TiO₂	Compact titanium dioxide

1 Introduction

As the world population grows larger, the concomitant provision of the preliminary needs, such as food, healthcare and energy, gets larger; however, this has also become a great challenge. The reliance of the energy sector on non-renewable fossil fuels not only risks the energy supply of the future generations but has been vastly debated that can also harm the existing environment endangering humans' health. The actuality of the risks posed by global warming and in general climate change and its rising trend in addition to the new economic opportunities provided by the transition to the clean-energy era drove many countries recently to reach the unprecedented Paris Agreement in December 2015. As a consequence of this Agreement, the major greenhouse gas producing countries are aiming to reduce their net greenhouse gas emission by more than 25% by 2030 [1]. An alternative and/or complementary source of energy is the freely and largely available solar energy hitting the earth surface with the theoretical potential of this solar power being $\sim 89,000$ Tera-watts [2].

Solar photovoltaic (PV) is a promising approach to utilize the abundant solar energy, convert it to electricity for transport, household electricity and industrial use. As an example of the significance of PV, Green recently stated [3] that photovoltaics is predicted to account for 35% of the additional electricity generation capacity installed globally by 2040, at a value of US\$3.7 trillion.

Currently, silicon solar cells (in the form of multi-crystalline, crystalline and amorphous) constitute about 90% of the PV market share. According to Green [3], the incremental improvement in silicon solar cells performance and the reduction in their production cost (due to increased manufacturing volume) over the past five years has made the entrance of the emerging PV technologies more difficult, but not implausible. Interestingly, the largest portion of the silicon solar cell modules prices is now from the solar cell encapsulation. The latter will become even more crucial for highly oxygen and moisture sensitive technologies such as,

organic PV, dye-sensitized solar cells and recently widely investigated perovskite solar cells (PSCs) [3-7].

In the last six years, the photovoltaic research community has seen the emergence of an astonishingly high performance, highly compositionally versatile, and easy to fabricate organic-inorganic metal halide perovskite (OIMHP) semiconductor material [4, 8, 9] with promising efficiencies achieved above 20% recently demonstrated [8, 10-12] for corresponding solar cells. Although at the first glance the significance of perovskite technology is deemed to be due to the low-deposition-cost of this solution-processed technique, it is in fact the high rate of yearly efficiency improvement which has made the technology very appealing to researchers [3, 12] in the PV community.

High efficiencies of commercial solar cell modules have been proposed to be the future of photovoltaic technology [3] with the potential value being 35% in 2050. These power conversion efficiencies are, however, achievable using multiple absorption threshold devices such as tandem solar cell structures. In the context of the next-generation tandem solar cells, OIMHPs are expected to have a great role to play due to their appropriate optical and electronic characteristics [4, 7, 13, 14]. One important property of photovoltaic perovskites which makes them a potential candidate for tandem solar cells is their bandgap tunability characteristic through compositional engineering [10, 15, 16] and also crystal size manipulation [17, 18]. This allows their application in multiple-junction perovskite-silicon tandem solar cells [3]. Recent limiting efficiency calculations [19], when neglecting the optical losses, have highlighted the maximum ideally attainable power conversion efficiency (PCE) of widely studied single-junction methylammonium lead triiodide ($\text{CH}_3\text{NH}_3\text{PbI}_3$) perovskite solar cells, with the optical bandgap of ~ 1.55 eV for the active layer, to be more than 31%. Calculations, by the same group [19], for the dual-junction perovskite/silicon tandem solar cells, excluding optical and resistive losses, resulted in PCEs as high as 40% which drops to efficiencies up to 30% when the losses are taken into account for various types of commercial silicon solar cells as the bottom cell.

The unique opto-electronic properties of OIMHPs which have allowed their corresponding solar cells to deliver high efficiencies include (but are not limited to): the reportedly low exciton binding energy [20-23], long charge carrier diffusion lengths surpassing the perovskite layer thickness in the device [24, 25], relatively high optical absorption coefficients on the order of those in III-V semiconductors [4, 26] and their high radiative recombination efficiencies delivering high voltages [24, 27]. The chemical formula of OIMHPs is ABX_3 (see Figure 1.1 for the high-temperature cubic structure of perovskites) [4], where A is a monovalent cation such as methylammonium, $CH_3NH_3^+$, formamidinium, $HC(NH_2)_2^+$, or Caesium, Cs^+ ; B is a divalent heavy metal cation such as lead, Pb^{2+} or tin, Sn^{2+} and X is a monovalent halogen ion such as iodide, I^- , bromide, Br^- or chloride, Cl^- . In addition to the perovskite structures consisting of single ionic components stated above at their A, B, and X positions, the pioneering work by Seok and colleagues [10], in which combination of organic cations and halogen ions used to achieve high PCEs, initiated the successful deployment of various combinatory chemical compositions for perovskite solar cells [28-30].

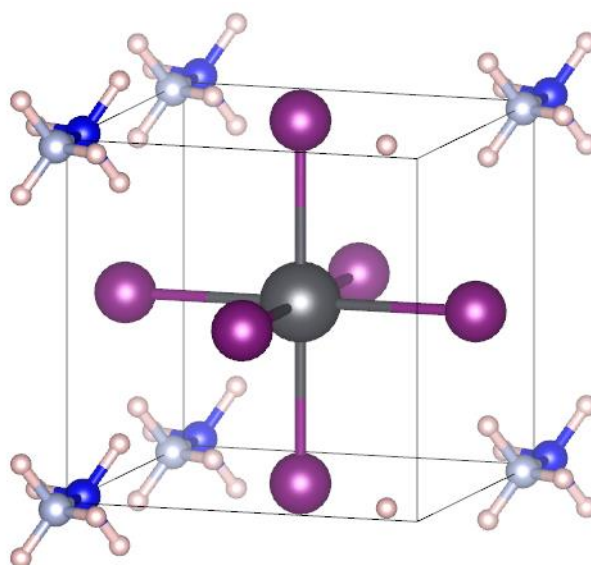


Figure 1.1 Perovskite crystal structure. A unit cell of the cubic perovskite crystal structure adapted at temperatures higher than 330 K and 240 K for $CH_3NH_3PbI_3$ [20, 31, 32] and $CH_3NH_3PbBr_3$ [32, 33], respectively. Within the temperature ranges of 160 to 330 K respective 150 to 240 K the two materials

possess tetragonal structural phase whereas, orthorhombic phase is adapted at temperatures lower than 160 K and 150 K for $\text{CH}_3\text{NH}_3\text{PbI}_3$ and $\text{CH}_3\text{NH}_3\text{PbBr}_3$ [32, 34], respectively.

To deploy these semiconductors to their maximum potential as the active layer in PSCs, a full understanding of their fundamental properties and also issues associated with their long-term operational implementation are necessary. This thesis is a step toward this goal.

1.1 Motivations and Significance

In this thesis we have performed insightful investigation on the optical and electronic properties of methylammonium lead trihalide perovskites as both standalone polycrystalline thin films and within a solar cell structure.

We believe that the article published in the Journal of Applied Physics Letters in association with the first part of this thesis [20], aimed at calculating the theoretical and experimental exciton binding energy in the organic-inorganic lead trihalide perovskite materials, was the first to explore the effect of polarons upon this energy, giving an explanation for the observed values intermediate between those previously calculated [35, 36]. The values calculated are in turn in reasonable agreement with those we measured on good quality tribromide and triiodide samples. Most polaronic theories treat the case with only one longitudinal optical (LO) phonon mode. However, due to the multiple LO modes in these materials, we have rationally used the effective LO energy theory of Hellwarth and Biaggio [37] to deduce this effective value from a fit to the frequency dependent material permittivity over a large frequency range, including dipolar, ionic (lattice displacement) and electronic contributions.

Secondly, we aimed to take the very first steps in developing the spatially-resolved luminescence imaging technique for full device characterization of PSCs. For this purpose, the application of PL and electroluminescence (EL) imaging techniques, which have been greatly contributing to the silicon solar cell performance improvement both at research and industrial scales [38], were reported for the first time in the paper published in the journal of Progress in

Photovoltaics [39]. The validity of the generalized relationship between luminescence intensity and device voltage was investigated. We then attempted to link the photovoltaic parameters of the planar structured PSCs to their characteristic PL and EL images. The technique was further used to explore the behaviour of the device performance over time when stored in benign condition (the related study was published in ref. [20]). At last, by using this useful technique, a detailed study was conducted to understand the evolution of the perovskite active layer and the interfaces of the solar cell upon its very first relatively long light-exposure.

1.2 Thesis Outline

This thesis is divided into two main sections. In the first part, a fundamental physical parameter of organic-inorganic lead halide perovskites, exciton binding energy, is investigated in detail. The second part is devoted to the understanding of short- and long-term performance of PSCs using spatially-resolved luminescence imaging technique.

1.2.1 Exciton Binding Energy

An appropriate knowledge of the exciton binding energy of a semiconductor – or the attractive coulombic force binding the photo-generated electron and hole together – is important since it can have remarkable influence on the shape and strength of the absorption spectrum and the nature of the instantaneously photo-generated species (neutral versus charged free carriers) [4]. The latter would then affect the transport properties of the carriers in the corresponding solar cell and consequently the optimum device design. Various methods have been employed to measure/calculate this parameter (the description of the different techniques used is covered in Chapter 2) with different degree of accuracy both for polycrystalline thin films [20, 22, 23, 36] and single crystals [40, 41] of OIMHPs. The versatility of the fabrication methods used for these materials, which allows the growth of films with wide range of morphologies, motivated researchers to also investigate the influence of the molecular microstructure on the magnitude of exciton binding energy [17].

1.2.2 Performance of Perovskite Solar Cells

Amongst a variety of deposition techniques used for high performance PSCs [10, 42-45], the majority of research groups employ solution-processed methods for active layer and/or selective contact deposition [10, 15, 44, 46, 47]. However, solution-processing is prone to spatial variations of both the electrical and optical properties of thin films, particularly within a large area device [48]. While there has been an enormous effort to improve device performance and understand the optoelectronic properties of the OIMHP materials [24, 49, 50], less work is focussed on developing fast and reliable full device characterization methods which is required for this technology to rapidly move forward for commercialization purposes. High-resolution fluorescence mapping techniques [51, 52] are useful for analysing laboratory scale devices and stand-alone perovskite films/single crystals but require long measurement time which is not suitable for fast characterization of large-area devices. Therefore, fast characterization techniques, which facilitate resolution of possible device non-uniformities across a large area, are deemed necessary. Additionally, imaging techniques could also be used to analyse performance changes of PSCs during their operational lifetime, in particular as PSCs are still lacking sufficient long-term stability under environmental conditions [6, 53, 54]. Thus, fast mapping techniques would be very useful to better understand the impact of local changes within the device on its overall performance [55, 56]. Identifying the sources of performance loss to improve device stability is of critical importance for the development of commercially deployable PSCs [3].

Chapter 2 describes the concept of excitons in semiconductors. A literature survey on the reported values of exciton binding energy for methylammonium lead trihalide perovskites ($\text{CH}_3\text{NH}_3\text{PbX}_3$; X = iodide, I, or bromide, Br⁻) is presented and the techniques used and the reported values are briefly discussed. With regards to the contribution of this thesis, first, the experimental method used to extract the exciton binding energy from the absorption spectrum of polycrystalline thin films of perovskites is formulated. Then, the consistency of the measured

values is checked with the theoretical calculation considering the electron-phonon cloud interaction.

Chapter 3 evaluates the validity of Planck's emission law for planar structured PSCs using both PL and EL imaging methods. These techniques, in particular EL imaging, are used to correlate the PV parameters obtained from light current-voltage measurements with the features observed in the images. In the last part of this chapter the degradation of the planar solar cells upon storage in dark and low-oxygen and -water (< 1 ppm) conditions is investigated.

Chapter 4 investigates the immediate and long-term response of the planar structured $\text{CH}_3\text{NH}_3\text{PbI}_3$ -based PSCs to spatially selective illumination of the device. The evolution of the bulk and interfaces are monitored after the initial illumination using EL and PL at open-circuit and short-circuit (PL_{OC} and PL_{SC} , respectively) conditions. The shortcomings of $\text{CH}_3\text{NH}_3\text{PbI}_3$ -based PSCs, showing noticeable ion migration potential, using TiO_2 as the electron selective contact are elaborated.

Finally, *Chapter 5* summarizes the key results and conclusions of this thesis. It presents suggestions for future studies which would allow extension of the results in this thesis to more OIMHP materials and device architectures.

2 Polaronic-Exciton Binding Energy in Methylammonium Lead Trihalide Polycrystalline Thin Films

2.1 Background

2.1.1 Excitons

When an electron (or hole, which simply is a quasi-particle formed in the absence of electron in the semiconductor valence band having an effective positive charge) moves in a semiconductor, crystal electrostatic forces from other electrons and ions in addition to any external forces will act on it. Forces from different ions are collectively defined as the crystal periodic potential (with its eigenstates properly described through Bloch waves) resulting in an energy-momentum (E - k) dispersion relation [57] for an electron. Therefore, the motion of an electrons (or hole) is commonly considered as a wave packet under an external field in a periodic potential where in a non-relativistic case the particle-like electron/hole would have an effective mass (m_{eff} ; which is a tensor depending on the direction the particle travels in the crystal):

$$\frac{1}{m_{eff}} = \frac{1}{\hbar^2} \frac{\partial^2 E}{\partial k^2} = \frac{1}{\hbar^2} \frac{\partial^2 E}{\partial k_i \partial k_j}; \quad i, j = x, y, z \quad (2.1)$$

In the vicinity of the band structure extrema in the semiconductor crystal, the dispersion relation normally tends to be parabolic. The parabolicity assumption in this region (i.e. bottom of the conduction band (CB) and top of the valence band (VB)), which is most important for the optical and transport properties of a semiconductor, results in a constant effective mass considering the second derivative of the E - k relationship. This forms the basis of the effective mass approximation. As formulated in equation (2.1), smaller curvature of the band would result in a larger effective mass.

Upon photoexcitation of a semiconductor system, an optical transition occurs where an electron from the VB is excited to the CB, leaving behind a hole, and bringing the system from ground to the excited state (Figure 2.1a). This optical transition is a two-particle process which, in the simplest form, is well defined by the effective mass approximation. This allows one to treat the photo-excited two-particle system, with its quanta called *exciton*, as a hydrogen-like problem where a Coulomb potential term can describe the interaction between the negatively-charged electron (in CB) and positively-charged hole (in VB). Solving the Schrodinger equation for a direct and parabolic band semiconductor, where the total motion of the exciton can be separated into a centre-of-mass translational and electron-hole relative motion, the exciton dispersion relation would become:

$$E_{ex}(n, K) = E_g - \frac{Ry_0}{n^2} + \frac{\hbar^2 K^2}{2M}; \quad n = 1, 2, 3, \dots \quad (2.2)$$

At band centre, the energy of the exciton, E_{ex} , is less than the bandgap, E_g , by $\frac{Ry_0}{n^2}$ where

$$Ry_0 = \frac{\mu e^4}{2\hbar^2 (4\epsilon_0 \epsilon)^2} \quad (2.3)$$

is the effective Rydberg (i.e. exciton binding energy) of the electron-hole system having a

reduced mass of $\mu = \frac{m_e \times m_h}{m_e + m_h} m_0$ (m_0 is the electron free mass, m_e and m_h are the electron and

hole masses as a fraction of the m_0) and moving in a medium with dielectric constant of ϵ . n is

the principal quantum number, \hbar the reduced Planck's constant, e the unit charge and $\frac{\hbar^2 K^2}{2M}$ is

the translational kinetic energy of the centre-of-mass ($M = m_e + m_h$) with wave vector of $K = k_e + k_h$.

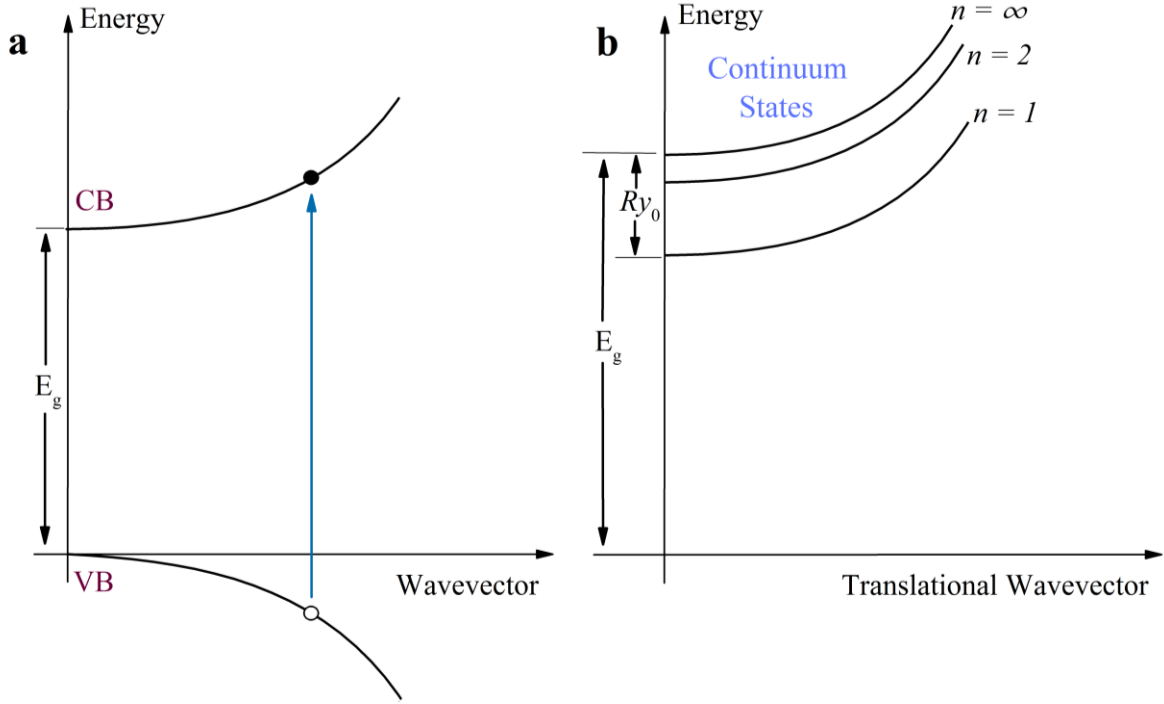


Figure 2.1 Electron-hole photo-excitation illustration using parabolic energy bands. a) Optical transition of an electron from VB to the CB by absorbing a photon having a minimum energy of E_g , leaving a hole in VB. b) The dispersion relation (E - K) of the quasi-particle exciton immediately after photoexcitation. The first excitonic transition located below the bandgap by Ry_0 [57].

Another important parameter adapted from the hydrogen model is the Bohr radius. Excitonic

Bohr radius is defined as: $a_B = \frac{\hbar^2 (4\pi\epsilon_0\epsilon)}{\mu e^2}$. Its importance lies in the fact that it acts as the

determining factor for the type of the exciton. If the excitonic Bohr radius is larger than the lattice constant, the wavefunction of the exciton is distributed over several unit cells forming weakly bonded Wannier-Mott excitons. If so, this would self-consistently confirm the credibility of the initial effective mass approximation. Wannier excitons are commonly created in III-V and II-VI inorganic semiconductors [58-62] and their exciton binding energy is defined using equation (2.3). Wannier excitons have been shown to be created in organic-inorganic lead halide perovskite as well [4, 20, 41]. In case of a confined wavefunction within the unit cell of the crystal (Bohr radius is less than the lattice parameter), the exciton is called Frenkel exciton (which are tightly bound), commonly formed in organic semiconductors due mainly to their

very low dielectric constant [63] which is insufficient to screen the attractive Coulombic interaction of the electron-hole system.

The excitonic Bohr radius has an additional critical role in the correct evaluation of the binding energy of Wannier excitons which requires its comparison with the polaron radius. According to Devreese [64], a CB electron (or VB hole) together with its self-induced lattice polarization in a polar semiconductor such as OIMHPs (or an ionic crystal) creates a quasiparticle, called a polaron.

In cases where lattice polarization can fully follow the motion of the electron and hole, the attractive potential between the two is completely screened and therefore, the static dielectric constant (ϵ_s) should be used in the Wannier model for binding energy calculation (equation 2.3). This occurs when the longitudinal optical (LO) phonon energy is larger than the exciton binding energy (the carriers' effective masses would then be replaced by their polaronic masses). The polaronic effective mass for both electron and hole ($m_{e,h}^p$) is defined in relation to the effective rigid mass ($m_{e,h}$) as [65]:

$$m_{e,h}^p \approx m_{e,h} \left(1 + \frac{a}{6}\right) \quad (2.4)$$

where the polaron coupling constant, a , encompasses the effects of LO frequency, ω_{LO} , optical (ϵ_∞) and static dielectric constants, and is given by:

$$a = \left(\frac{1}{\epsilon_\infty} - \frac{1}{\epsilon_s} \right) \frac{e^2}{2\hbar\omega_{LO}} \sqrt{\frac{2m_{e,h}\omega_{LO}}{\hbar}}. \quad (2.5)$$

When the exciton binding energy is equal to or larger than the LO phonon energy, the lattice polarization can only partially follow the electron-hole system in which case, an effective dielectric constant falling in between the optical and static values should be employed (the

carriers' effective masses would also adopt values between the rigid and polaron ones). The latter is the subject of this chapter.

Therefore, it is important that any spectroscopic characterization technique which allows direct calculation of the R_{y0} , should ensure its self-consistency with the LO phonon energy.

2.1.2 Why Exciton Binding Energy is Important

An appropriate knowledge of the value of the exciton binding energy is essential since it can determine the nature of the majority of the photo-generated species (i.e. free carriers versus excitons) in a semiconductor. Even within the context of Wannier excitons, binding energies greater than the probability of thermal dissociation at the working temperature (with thermal energy of $k_b \times T \approx 26$ meV at room temperature) would require an additional mechanism for exciton dissociation into free carriers through which they can readily contribute to the photocurrent [66]. Where the binding energies are so low that their influence on the transport mechanism of the charge carrier is negligible, the n- and p-type contacts in the heterojunction structure of the solar cell (like in most perovskite solar cells) would only act as selective contacts (blocking the undesirable carriers) for the photo-generated electrons and holes, respectively. In extreme instances of π -conjugated polymers used in organic photovoltaics and light-emitting diodes, the large binding energies in the order of few hundreds of milli-electronvolts, would result in extra loss in the open-circuit voltage of the device (with respect to the bandgap of the absorbing layer) due to the free energy required for the dissociation of the Frenkel excitons [67, 68] in addition to a low illumination-induced current generation.

Most spectroscopy measurements (such as transient absorption spectroscopy [24, 69], photo-induced terahertz conductivity [70, 71]) have so far shown the predominant concentration of photo-generated free charge carriers and their bimolecular recombination nature in the archetypical $\text{CH}_3\text{NH}_3\text{PbI}_3$ perovskites whereas, a considerable population of excitons is reported for $\text{CH}_3\text{NH}_3\text{PbBr}_3$ containing bromide [69].

2.2 Literature Review

2.2.1 Exciton binding Energy Values and Extraction Methods

2.2.1.1 Absorption Band-edge Modelling

One frequently used approach for excitonic binding energy determination in organic-inorganic lead halide perovskites is to model the absorption spectrum band edge [20, 33, 72-77]. When the correlated electron-hole Coulombic interaction is overlooked, an approach known as the Tauc plot is often used to determine the bandgap for allowed transitions of direct bandgap semiconductors (This is wrongly applied in semiconductors with excitonic effects and large spectrum broadening):

$$\alpha = \frac{A}{E} (E - E_g)^{\frac{1}{2}} \quad (2.6)$$

α is the absorption coefficient, E , the photon energy and A is a relatively energy independent term dependent on the semiconductor's reduced optical mass and transition probabilities for excitations from the valence to conduction band. The square of absorption coefficient (often multiplied by the photon energy) is plotted as a function of energy and the intercept of a linear fit to the absorption edge is found and identified as the bandgap. A more comprehensive treatment by Elliott [78] taking electron-hole interaction into account produces a fundamentally different result. The theory of Elliott is described in section 2.4.1 and only Ry_0 values reported in the literature employing this approach are presented in this section.

The excitonic binding energy value reported by Even *et al.* [72] at both low-temperature (LT; orthorhombic) and high-temperature (HT; tetragonal) phases, that being 15 meV and 5 meV, respectively, and were extracted by fitting the published absorption spectra of Ishihara *et al.* (in 1994; cubic crystals of $\text{CH}_3\text{NH}_3\text{PbI}_3$ dispersed in poly(methylmetacrylate)) [79] with the theory of Elliot. These were found to be relatively temperature-independent in both structural phase

temperature ranges. Yamada and co-workers used the absorption band-edge modelling approach to fit the absorption spectrum of $\text{CH}_3\text{NH}_3\text{PbI}_3$ infiltrated into the mesoporous titanium dioxide (mp-TiO₂) [73] and obtained R_{y_0} of 30 meV at 13 K and 6 meV at 300 K. This use of mesoporous structured substrate prevented the resolution of the pronounced excitonic resonances at the absorption onset [36].

Saba *et al.* [76] modified the theory of Elliot [78] to account for small deviations in the conduction and valence band-edge parabolic dispersion. By introducing an extra parameter in the fitting procedure as non-parabolicity constant, c_{np} , a modified optical joint-density of states was derived from a newly defined electron-hole dispersion relationship: $E(k) - E_g = E_e(k) + E_h(k) - E_g = \hbar^2 k^2 / 2\mu - c_{np} k^4$ (k is wavevector). Relatively high value of R_{y_0} , 25 ± 3 meV, was measured at 170 K and 300 K, indicating its independency within the HT phase of $\text{CH}_3\text{NH}_3\text{PbI}_3$ as opposed to refs. [20, 73].

Sestu *et al.* [75] suspected that the discrepancy observed in the values extracted this way could originate from the difference in the underlying mechanisms contributing to the absorption spectrum line-shape broadening [66, 75]. In order to overcome this, the following approach was proposed. Regardless of the degree of smearing, the normalised integral of the absorption

coefficient versus energy (i.e. $\int_0^{E_2} \alpha(E) dE / \alpha(E_2)$) is independent of the degree of smearing,

depending only on R_{y_0} , if the upper energy end, E_2 , is selected in a region where smearing is ineffective (such as at energies several half-width at half maximum above bandgap in a Gaussian broadened theoretical absorption spectrum, and somewhat further in a Lorentzian broadened one). A temperature-independent binding energy was calculated in the orthorhombic phase (34 meV), which dropped by 20% to 29 meV at the orthorhombic-to-tetragonal phase transition temperature (~ 160 K) which remained constant in the tetragonal phase as well [75]. Modifications due to band non-parabolicity introduced by the same group in ref. [76] was also adapted in their new formalism in ref. [75].

To sum up this section, when the unmodified theory (or minimally modified as presented in the Result and Discussion section – section 2.4.4) had been used to model the absorption onset of the polycrystalline thin films of triiodide perovskite at room temperature (~298 K), binding energies of 10 ± 3 meV had been obtained [20, 77, 80].

2.2.1.2 Magneto-absorption Measurement

The continuous study on the experimental measurement of the exciton binding energy (Ry_0) of 3D organic-inorganic lead halide perovskites was initiated by Hirasawa *et al.* [81] using the diamagnetic shift characteristic of the 1S excitonic state (i.e. exciton state associated with the first principle quantum number) in the absorption spectrum of $\text{CH}_3\text{NH}_3\text{PbI}_3$ under magnetic field at low temperature (4.2 K). They measured Ry_0 of 37 meV employing the optical dielectric constant of 6.5 (which is the high frequency relative dielectric function in the near infra-red region). Cubic crystals of $\text{CH}_3\text{NH}_3\text{PbI}_3$ dispersed in poly(methylmetacrylate) were used in that study. About ten years later, by applying similar method, Tanaka *et al.* [82] reported Ry_0 values of 50 meV and 76 meV for $\text{CH}_3\text{NH}_3\text{PbI}_3$ and $\text{CH}_3\text{NH}_3\text{PbBr}_3$, respectively (optical dielectric constants of 6.5 and 4.8 were used, respectively). In the latter study, the samples were polycrystalline films deposited via single-step solution process. In both abovementioned studies, the shift in energy of the pronounced excitonic feature in the polarized magneto-absorption spectra were fitted using $E = E_0 \pm \frac{1}{2} g_{\perp} \mu B + c_0 B^2$ (B is the magnetic field strength, E_0 is the excitonic ground state energy at $B = 0$, g_{\perp} is the effective g factor and c_0 the diamagnetic coefficient). Knowing the diamagnetic coefficient, the exciton binding energy was calculated for a 3D Wannier exciton through [81, 82]:

$$\frac{Ry_0}{Ry_H} = \left(\frac{1}{\epsilon^4 (c_0/c_H)} \right)^{1/3} \quad (2.7)$$

where Ry_H and c_H are the diamagnetic coefficient and Rydberg constants of hydrogen atom. In 2014, Meredith and co-workers reassessed the exciton binding energy of polycrystalline thin

films of $\text{CH}_3\text{NH}_3\text{PbI}_3$ using the measured diamagnetic coefficients in [81, 82] (at low temperature), however, low frequency (20 Hz) dielectric constant of 70 (measured at room temperature) was used instead (which includes the ionic conductivity contribution to dielectric characteristic of perovskites). R_{y_0} of 1.7-2.1 meV was calculated (values of this order and slightly greater, however, could not model the absorption band-edge of $\text{CH}_3\text{NH}_3\text{PbI}_3$ as depicted in Figure 2.8 of Results and Discussion section).

Very recently, Nicholas and colleagues re-considered the use of magneto-absorption spectroscopy of organic-inorganic lead halide perovskite polycrystalline thin films extending the applied magnetic fields up to 150 T [21, 22]. At LT (2 K; orthorhombic phase), they managed to resolve both 1S, excitonic ground state, and 2S, the first excitonic excited states upon increasing the magnetic field. The ability to resolve the 2S state, as compared to old data set, was mainly attributed to the better quality of the samples. At high enough fields, Landau levels (quantized energy levels formed upon magnetic field perturbation of the continuum part of the energy states) were also detected. Modelling the full data set, R_{y_0} of 16 meV and 25 meV were measured at LT phase (2 K) for $\text{CH}_3\text{NH}_3\text{PbI}_3$ [21] and $\text{CH}_3\text{NH}_3\text{PbBr}_3$ [22], respectively. Large spectrum thermal broadening prevented a credible similar analysis at high temperature phase (although values of 10-12 meV were proposed for triiodide at 160 K and higher). Importantly, it was realized that the exciton reduced mass only slightly change upon structural phase transition which indicates the critical role that an appropriate choice of dielectric constant plays in determination of the binding energy using Wannier-Mott model (equation 2.3). Considering the temperature dependence of the dielectric function in methylammonium lead halide perovskites [32, 83], the dependency of excitonic binding energy on temperature in both triiodide and tribromide is expected [20].

Noticeably, Nicholas and colleagues observed a linear trend in the Landau levels over a relatively large energy range, implying that a constant effective mass used in their modelling is reasonable and therefore, the non-parabolicity effects are expected to be fairly small in the

conduction and valence band [21]. This outcome, however, allows the application of the absorption band-edge modelling using the Elliot theory (as employed in the studies discussed in the previous section) up to fair amount of energy above the bandgap.

2.2.1.3 Temperature-dependent Photoluminescence Measurement

An alternative controversial approach [84] for the determination of exciton binding energy in trihalide perovskites is to fit the temperature-dependence of the spectrally-integrated photoluminescence intensity [85-88] using

$$I(T) = \frac{I(0)}{1 + A \exp(-E_b/k_b T)} \quad (I \text{ is the luminescence intensity, } T, \text{ temperature, } I(0), \text{ luminescence intensity at 0 K, } A \text{ is a constant, } E_b \text{ and the exciton binding energy (similar to } Ry_0)).$$

Applying this technique, Wu et al. [87] calculated a large value of $Ry_0 \approx 62$ meV for thin film of $\text{CH}_3\text{NH}_3\text{PbI}_{3-x}\text{Cl}_x$ when fitting to the tetragonal phase only [87]. Exploring the full temperature range, values in the order of 19 ± 3 meV has also been reported for $\text{CH}_3\text{NH}_3\text{PbI}_3$ thin films [88]. Performing the fitting from ~ 80 K to 300 K, Savenije *et al.* obtained 32 ± 5 meV for triiodide infiltrated into meso-porous Al_2O_3 [86]. This method has also been adapted for tribromide samples [85] with the reported values of 84 ± 10 meV being 2-3 times greater than most of the literature [20, 22, 33]. The spread of the extracted values implementing a similar technique here, however, would not be surprising noting the following notions forming the basis of this method. This method is based on the assumption that the thermal dissociation of bound excitons, upon increase in temperature, into free carriers would quench the luminescence intensity with an inherent supposition that non-radiative recombination mechanism is temperature independent [84]. These have been recently challenged [66, 84], where Laura Herz discussed [66] the temperature dependent nature of the efficiency of various mechanisms associated with free carrier recombination in mixed organic-inorganic lead halide perovskites [89].

Furthermore, being aware of the likely variation of the exciton binding energy with temperature even within a specific phase (discussed above in section 2.2.1.1) the use of a global fit to the

integrated photoluminescence intensities in a range of temperatures casts doubt on the credibility of applying this approach to determine a single value for binding energy in a temperature range.

2.2.2 Discussion about the Literature Values

The summary of the reported values in the literature is presented in Table 2.1. The topic of exciton binding energy has been controversial in the field of mixed organic-inorganic metal halide perovskites due to a range of values reported from different approaches with varying degrees of validity. One additional reason for this discrepancy in the calculated/measured R_{y0} values could be the crystal quality and also the degree of poly-crystallinity (i.e. impact of microstructure) of the perovskite layer itself. The latter has been recently discussed by few research groups [17, 90, 91]. Moreover, there is no consensus on whether R_{y0} remains unchanged within a single structural phase of $\text{CH}_3\text{NH}_3\text{PbI}_3$ (decreasing in both tetragonal and orthorhombic phases in references [20, 73] versus unchanged values reported in references [72, 75]) whereas, for $\text{CH}_3\text{NH}_3\text{PbBr}_3$ no significant changes were identified so far [20]. When relying on the simple Wannier-Mott model for binding energy calculation, the correct knowledge of reduced mass, and dielectric constant, is important (equation 2.3). The linear proportionality of the reduced mass in equation (2.3) and the experimental evidence that phase transition would only influence this physical parameter slightly [21, 22] reveals the importance of the dielectric constant which has an inverse squared relationship to R_{y0} . In the perovskites of interest, ionic conductivity, molecular dipole (organic cation dipole), ionic permittivity (nucleus vibrations) and charge carrier electronic effects contribute to the full spectrum dielectric function. However, the static limit of the dielectric function for R_{y0} calculation in organic-inorganic metal halide perovskites is not established yet. The dissimilar response of the relative permittivity to temperature at different frequencies is also known [32, 83]. For instance, the dielectric constant at 100 kHz [32] in the tetragonal phase (orthorhombic phase) reduces (increases) with temperature dramatically (only slightly) whereas, at 90 GHz [83] the dielectric

constant rises with temperature in the tetragonal phase (see Figure 2.2). This behaviour was observed in both I- and Br-based perovskites. Recently, La-o-Vorakiat *et al.* conducted temperature-dependent terahertz time-domain spectroscopy and detected four phonon modes in the microwave frequency range (0.3-2.0 THz) at 20 K where the four modes merged into two due to spectrum smearing as the temperature increased [92]. Importantly, the phonon resonance energies increased as the temperature was ramped up. This trend in phonon modes in addition to the increasing tendency of the dielectric constant in the microwave frequency range as opposed to lower frequencies, however, carefully indicates that *the static dielectric constant would most likely include only the electronic and ionic displacement screening effects but not dipolar contribution from the organic cation*. This agrees very well with the very recent theoretical study which concluded that the exciton binding energy in $\text{CH}_3\text{NH}_3\text{PbI}_3$ is principally dependent on the electronic structure of the PbI_3 inorganic cage [93].

We also note that considering the large vibrational modes merely associated with the liberal and torsional motions of the dipolar CH_3NH_3^+ cation (mostly being greater than 100 cm^{-1} or $\geq 12.4\text{ meV}$) [94-96], and the correspondingly high relative dielectric constant values [14, 32], it is unlikely that these modes directly contribute to the screening of the electron-hole Coulombic interaction at room temperature. This would lead to very low binding energies that would be in contrast to the recent observation of coexisting free carrier and exciton populations in $\text{CH}_3\text{NH}_3\text{PbI}_3$ at room temperature [69, 97] and also would not allow modeling of the sharp and excitonic-enhanced absorption band-edge of these semiconductors (this will be elaborated below; see Figure 2.9).

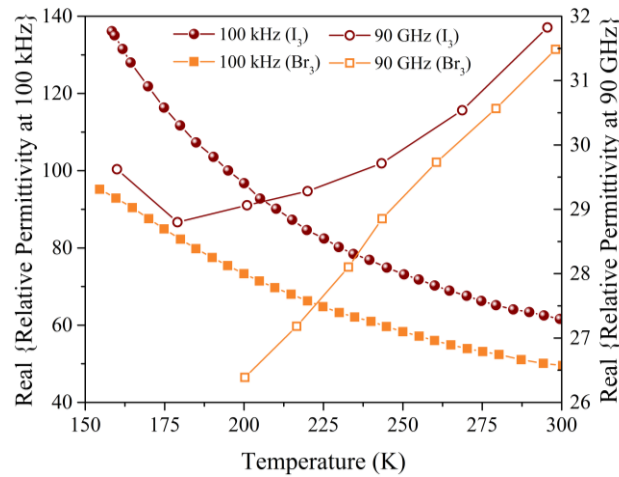


Figure 2.2 Temperature-dependent variation of real part of the relative permittivity of $\text{CH}_3\text{NH}_3\text{PbBr}_3$ and $\text{CH}_3\text{NH}_3\text{PbI}_3$. The data at 100 kHz and 90 GHz are reproduced from ref. [32] and [83], respectively. Solid (hollow) circle symbol represent triiodide data at 100 kHz (90 GHz) and solid (hollow) square symbol represent tribromide data at 100 kHz (90 GHz).

Also, as elaborated above, there exists a fairly large discrepancy in the reported values for the exciton binding energy of the methylammonium lead trihalide perovskites even when similar method is used for its measurement and at a specific temperature. Difference in the sample microstructure could be a potential explanation of the latter. In light of the recent study by Grancini *et al.* [17], where the role of crystal size/quality on the instantaneous electron-hole interaction (i.e. Ry_0) was elucidated, the discrepancy between the extracted values from fitting the absorption band-edge could be explained by the change in the perovskite microstructure. It was concluded using theory and experiments that disordered organic cation dipole domains in small, defective crystals with large portion of poly-crystallinity can create a large electrostatic potential fluctuation which causes a substantial screening of the photo-generated excitons [17] leading to very small R_0 in the order of 2 meV [35] to 5 meV [72] as if the material behaves in the non-excitonic regime whereas, large and defect-free crystals exhibit an order of magnitude greater R_0 [17, 36]. Importantly, a recent study has investigated the extent by which Ry_0 would be affected by the disorder induced by the organic cation molecular dipole. Using interacting

tight-binding model this effect was realized to be small and only ~10% [93]. Although very interesting, the latter requires experimental proof.

Table 2.1 Summary of the reported exciton binding energy in the literature. The perovskite composition, temperature and method of measurement are included.

Method	Perovskite	Phase	Specifications	Temperature (K)	Ry_0 (meV)	Reference
Band-edge modelling by Elliot's theory	$\text{CH}_3\text{NH}_3\text{PbI}_3$	Orthorhombic	Cubic crystals dispersed in PMMA	<160	15	[72]
Band-edge modelling by Elliot's theory	$\text{CH}_3\text{NH}_3\text{PbI}_3$	Tetragonal	Cubic crystals dispersed in PMMA	>200	5	[72]
Band-edge modelling by Elliot's theory	$\text{CH}_3\text{NH}_3\text{PbI}_3$	Orthorhombic	Mesoscopic	13-150	30	[73]
Band-edge modelling by Elliot's theory	$\text{CH}_3\text{NH}_3\text{PbI}_3$	Tetragonal	Mesoscopic	160-300	6	[73]
Band-edge modelling by Elliot's theory	$\text{CH}_3\text{NH}_3\text{PbI}_3$	Tetragonal	Bulk	170, 300	25 ± 3	[76]
Spectrally integrated normalized absorption near Band-edge	$\text{CH}_3\text{NH}_3\text{PbI}_3$	Orthorhombic	Bulk	80-140	34 ± 3	[75]
Spectrally integrated normalized absorption near Band-edge	$\text{CH}_3\text{NH}_3\text{PbI}_3$	Tetragonal	Bulk	170-300	29	[75]
Spectrally integrated normalized absorption near Band-edge	$\text{CH}_3\text{NH}_3\text{PbBr}_3$	Orthorhombic, Tetragonal, Cubic	Bulk	80-300	60 ± 3	[75]
Band-edge modelling by Elliot's theory	$\text{CH}_3\text{NH}_3\text{PbI}_3$	Tetragonal	Bulk	Room Temperature	9 ± 1	[80]
Band-edge modelling by Elliot's theory	$\text{CH}_3\text{NH}_3\text{PbI}_3$	Tetragonal	Bulk	Room Temperature	13.1 ± 0.1	[77]
Band-edge modelling by Elliot's theory	$\text{CH}_3\text{NH}_3\text{PbBr}_3$	Cubic	Bulk	Room Temperature	40.03 ± 0.1	[77]
Diamagnetic shifts in magneto-absorption using optical ϵ	$\text{CH}_3\text{NH}_3\text{PbI}_3$	Orthorhombic	Cubic crystals dispersed in PMMA	4.2	37	[81]
Diamagnetic shifts in magneto-absorption using optical ϵ	$\text{CH}_3\text{NH}_3\text{PbI}_3$	Orthorhombic	Polycrystalline film	4.2	50	[82]
Diamagnetic shifts in magneto-absorption using optical ϵ	$\text{CH}_3\text{NH}_3\text{PbBr}_3$	Orthorhombic	Polycrystalline film	4.2	76	[82]

Diamagnetic shifts in magneto-absorption using static ϵ (at 20 Hz)	$\text{CH}_3\text{NH}_3\text{PbI}_3$	Tetragonal	---	RT	1.7-2.1	[35]
Magneto-absorption spectroscopy	$\text{CH}_3\text{NH}_3\text{PbI}_3$	Orthorhombic	Bulk	2	16	[21]
Magneto-absorption spectroscopy	$\text{CH}_3\text{NH}_3\text{PbBr}_3$	Orthorhombic	Bulk	2	25	[22]
Temperature-dependent Photoluminescence	$\text{CH}_3\text{NH}_3\text{PbI}_{3-x}\text{Cl}_x$	Tetragonal, Cubic	Bulk	160-320	62.3 ± 8.9	[87]
Temperature-dependent Photoluminescence	$\text{CH}_3\text{NH}_3\text{PbI}_3$	Orthorhombic, Tetragonal	Mesoscopic	80-300	32 ± 5	[86]
Temperature-dependent Photoluminescence	$\text{CH}_3\text{NH}_3\text{PbBr}_3$	Tetragonal, Cubic	Bulk	24-350	84 ± 10	[85]
Temperature-dependent Photoluminescence	$\text{CH}_3\text{NH}_3\text{PbI}_3$	Orthorhombic, Tetragonal	Bulk	2-300	19 ± 3	[88]

2.3 Experimental Methods

2.3.1 Material Synthesis and Precursor Preparation

Unless specified otherwise, all materials were purchased from either Alfa Aesar or Sigma-Aldrich and used as received. $\text{CH}_3\text{NH}_3\text{I}$ was synthesized by mixing 24 mL CH_3NH_2 (33% in ethanol) and 10 mL HI (57% in water) in 100 mL ethanol. After stirring for 2 h, the solvent was removed on a rotary evaporator. The white powder was then dried in a vacuum oven at 60 °C for 24 h.

$\text{CH}_3\text{NH}_3\text{Br}$ was synthesized following a previously reported method [98], by mixing methylamine (33% in methanol, Sigma-Aldrich) with hydrobromic acid (48% in water, Sigma-Aldrich) in a 1:1 molar ratio in a 250 ml round bottom flask under continuous stirring at 0 °C for 2 h. The precipitate was recovered by rotary evaporation at 60 °C, and then washed three times with diethyl ether in an ultrasonic bath for 30 min. The final product was collected after dehydration at 60 °C and placed in a vacuum chamber overnight.

2.3.2 Sample Fabrication

$\text{CH}_3\text{NH}_3\text{PbI}_3$ films were deposited on clean thin (1 mm) microscope or thick (3 mm) soda-lime glass substrates using the gas-assisted technique [46]. In brief, 25 μL 45 wt% $\text{CH}_3\text{NH}_3\text{PbI}_3$ dimethylformamide (DMF) solution, prepared from PbI_2 and $\text{CH}_3\text{NH}_3\text{I}$ in a molar ratio of 1:1, was spread on the substrate, then spun at 6500 rpm. After 2 sec a dry argon gas was blown on the solution during the spinning. Finally, the film was annealed at 100°C for 10min to remove the residue solvent and induce the crystallization. In order to control the thickness of the $\text{CH}_3\text{NH}_3\text{PbI}_3$, different concentrations (45 wt% and 55 wt%) of the $\text{CH}_3\text{NH}_3\text{PbI}_3$ dimethylformamide (DMF) solution were used. A thin layer of Poly(methyl methacrylate) (PMMA, Sigma-Aldrich) was coated on the top of the $\text{CH}_3\text{NH}_3\text{PbI}_3$ layer via spin coating at the speed of 2000 rpm in order to preserve the samples against air and moisture in the low-temperature measurements.

$\text{CH}_3\text{NH}_3\text{PbBr}_3$ films were deposited using the vapour-assisted method [98]. Firstly, PbBr_2 solution in DMF with a concentration of 1 M was spin-coated on to a thick (3 mm) borosilicate glass substrate at 2500 rpm for 60 s. After annealing at 70 °C for 30min, the film was treated by $\text{CH}_3\text{NH}_3\text{Br}$ vapour at 150 °C for 10 min in a closed glass petri-dish with $\text{CH}_3\text{NH}_3\text{Br}$ powder surrounded on a hotplate in glovebox. In the final step, the film was rinsed in isopropanol at room temperature. No additional PMMA layer is deposited.

2.3.3 Optical Measurement

For optical density (OD) measurements, samples were mounted, under vacuum, in an optical cryostat (Hansen and Associates) equipped with front and rear sapphire windows. A closed-cycle helium cryostat (CTI Cryogenics) was used to control the temperature of the sample between 10 K and 300 K. Light from a fibre-coupled halogen lamp (Mikropack) was used to illuminate the sample from the backside and the transmitted light was collected using free space optics and coupled to a 0.27 m scanning spectrometer (SPEX 270M) with a 600 gvs/mm grating blazed at 750 nm. The spot size on the sample was estimated to be 300 μm . Spectrally resolved

transmitted light was detected using a thermo-electrically cooled photomultiplier with GaAs photocathode (Hamamatsu). A lock-in amplifier and optical chopper (SRS Instruments) was used to optimise the signal to noise and eliminate background light. Transmission data was referenced against a blank substrate in order to correct for the spectral response of the system. Room temperature absorption coefficient measurements were carried out using Varian Cary 500 Scan UV-Vis-NIR Spectrophotometer using an integrating sphere.

Optical density is a measure of the degree of the light intensity attenuation upon transmission through an absorbing medium. To calculate the OD spectra, the common logarithm of the corrected transmission spectra (T ; the ratio of the transmitted over incident light intensity) were evaluated using: $OD = -\log_{10}(T)$.

2.4 Results and Discussion

2.4.1 Elliot Theory for Exciton Binding Energy Measurement

2.4.1.1 Excitonic-enhanced Absorption Coefficient

Organic-inorganic lead halides of present interest [4, 99, 100] are generally considered direct bandgap [72, 101] semiconductors. Strong spin-orbit coupling creates a split-off band in the conduction, rather than the valence band and improves effective-mass approximations near band-edges [72]. Excitons are expected at band critical points, with Elliott [78] calculating excitonic-enhanced band-edge absorption coefficient α as:

$$\alpha = \frac{A^2 R}{E} \left(\sum_n \frac{N(E-E_g + E_n)}{n} + \frac{Un(E-E_g)}{1 - e^{2\pi R(E-E_g)}} \right) \quad (2.8)$$

A is nominally energy-independent. A encompasses the semiconductor optical reduced masses, transition matrix element and has an inverse relation with the medium refractive index where the latter is presumably a slowly varying function of energy. α is plotted in Figure 2.3a with and

without excitonic effects, with large differences even for above-bandgap, unbound absorption range. The empirical approximation of equation (2.8) is derived, and presented in equation (2.9), which has the advantage of being able to be convolved analytically with Gaussian and Lorentzian distribution functions.

$$\alpha = ARy_0^{1/2} \left(2Ry_0 \sum_{n=1}^N \frac{\delta[E - E_g + Ry_0/n^2]}{n^3} \right) + ARy_0^{1/2} \left(UnitStep[E - E_g] + \left(\frac{E - E_g + Ry_0}{Ry_0} \right) UnitStep[E - E_g - Ry_0]/58 \right) \quad (2.9)$$

It is noted that the first term (top line) of equation 2.9 is the contribution from excitonic transition whereas, the rest of the terms (bottom line) are associated with free carrier transition affected by the exciton binding energy. It is important to note that this expression is accurate to within 1% for $20Ry_0$ above the bandgap. Homogeneous (convolution of equation 2.9 with a Lorentzian distribution; equation 2.10) and inhomogeneous (convolution of equation 2.9 with a Gaussian distribution; equation 2.11) broadening would smear α , with Figure 2.3b showing Lorentzian broadening effects. Once broadening full width at half maximum (FWHM or 2Γ) exceeds $\sim 3Ry_0$, excitonic peaks disappear (similarly for inhomogeneous broadening and combined pseudo-Voigt profile composed of weighted sum of Lorentzian (L) and Gaussian (G) profiles with a common FWHM [102] – $2\Gamma = 2\sqrt{2\ln(2)}\sigma$, where σ is the Gaussian standard deviation). Importantly, this implies that *lack of an excitonic peak does not necessarily mean that excitonic effects upon absorption are small* in organic-inorganic lead halide perovskites.

$$\alpha * L = \frac{ARy_0^{\frac{1}{2}}}{E} \left\{ \frac{2Ry_0}{\pi} \sum_{n=1}^N \frac{\Gamma/n^3}{(E - E_g + Ry_0/n^2)^2 + \Gamma^2} + \left[0.5 + ArcTan\left(\frac{E - E_g}{\Gamma}\right) \right] / \pi \right. \\ \left. ArcTan\left(\frac{E - E_g - Ry_0}{\Gamma}\right) \frac{(E - E_g - Ry_0)}{58\pi Ry_0} - ArcTan\left(\frac{E - E_m}{\Gamma}\right) \left(\frac{(E - E_m)}{58\pi Ry_0} \right) + \frac{(E_m - E_g - Ry_0)}{116Ry_0} - \right. \\ \left. \frac{\Gamma}{116Ry_0\pi} \ln \left[\frac{(E - E_g - Ry_0)^2 + \Gamma^2}{(E - E_m)^2 + \Gamma^2} \right] \right\}$$

(2.10)

$$\alpha * G = \frac{ARy_0^{\frac{1}{2}}}{E} \left\{ 2Ry_0 \sum_{n=1}^N \frac{e^{-\frac{(E-E_g+Ry_0/n^2)^2}{2\sigma^2}}}{n^3 \sqrt{2\pi} \sigma} + \left[1 + \text{Erf} \left(\frac{E-E_g}{\sqrt{2} \sigma} \right) \right] \right\} / 2$$

$$+ \frac{\sigma e^{-\frac{(E-E_g-Ry_0)^2}{2\sigma^2}}}{58\sqrt{2\pi}} + \frac{(E-E_g-Ry_0)}{116 Ry_0} \left[1 + \text{Erf} \left(\frac{E-E_g-Ry_0}{\sqrt{2} \sigma} \right) \right]$$

(2.11)

It is confirmed that a maximum of 100 discrete excitonic states (i.e. $n=100$) suffice, above which changes in the theoretical spectrum are not apparent.

We further considered improving the fits to the experimental spectra by following Toyozawa's derivation of exciton absorption line-shape [103] in which the broadening associated with each excitonic state in the hydrogen-like line series and that of the continuum absorption differ. Commonly, an asymmetry parameter ($\ll 1$) accounting for exciton discrete states interaction with the continuum of states is also introduced, which is not taken into account in the line-shape modelling here. We considered scaling the half width at half maximum (HWHM) of the excited excitonic states [58] through:

$$\Gamma_X^{(n)} = \Gamma_C - \frac{\Gamma_C - \Gamma_X^{(1)}}{n^2} \quad (2.12)$$

where $\Gamma_X^{(1)}$, Γ_C , $\Gamma_X^{(n)}$ and n are the HWHM of the exciton ground state (i.e. $n=1$), continuum of states and the excited excitonic states and the principle quantum number, respectively. Note that the first two are independent free fitting parameters. It is noteworthy that this relationship between the damping parameters of the states is an empirical one giving reasonable fits with acceptable physical parameters for III-V and II-VI semiconductors [58, 59]. This formalism indicates that the damping parameter increases with energy (i.e. quantum number) of the states.

2.4.1.2 Absorption Band-edge Fitting Procedure

In order to apply a consistent approach to all the fittings to the experimental optical density/absorption coefficient spectra and to lessen the effect of valence- and conduction-band non-parabolicity expected in organic-inorganic perovskites [104], we have fitted the data within one binding energy plus a multiple of Γ (i.e. HWHM of the Lorentzian broadening function) above the band gap or parametrically, $E_g + [Ry_0 + f \times \Gamma]$. However, assigning 1.0, 1.25 or 1.5 to f does not affect the extracted fitting parameters noticeably, in particular, the exciton binding energy. As such, all the results presented in this chapter have been obtained using the multiplier, f , equal to 1.0. Matlab R2012b software was used for all the fitting purposes. In order to minimize the chance of trapping in any local minima we primarily covered the full parameter space by using the *multistart* solver – as the global search function – with *lsqcurvefit* as the local solver. The optimum parameters obtained in this way were used as input to the *nlinfit* function, using Levenberg-Marquardt nonlinear least squares algorithm, to extract the final optimum fitting parameters and the corresponding 95% confidence levels.

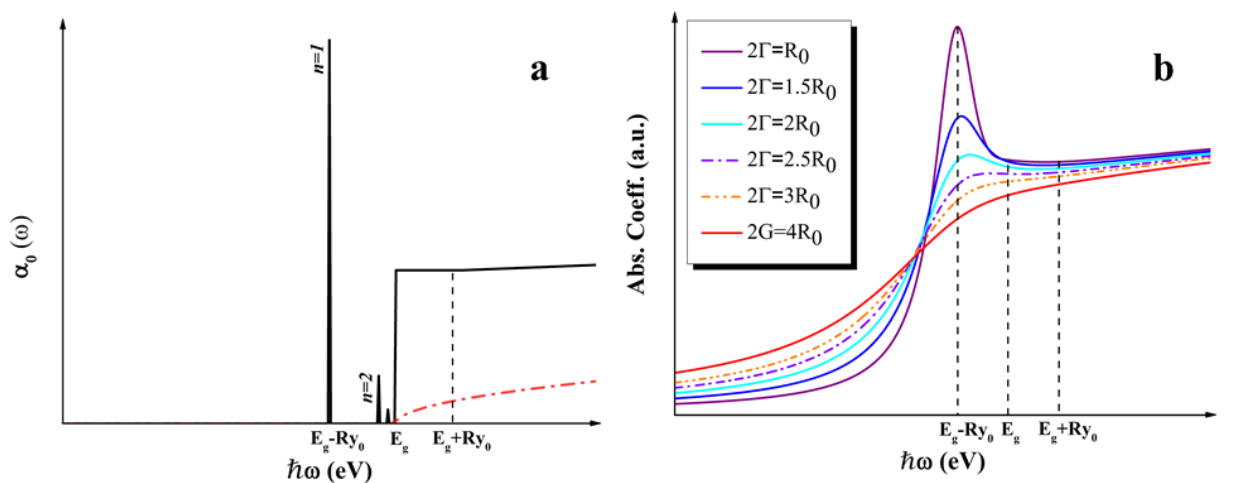
2.4.2 Assessment of the Excitonic Nature of the Absorption Band-edge

As for our measurements using good-quality bromide and iodide samples (Figures 2.3c and 2.3d; see Figure 2.4 for a top-view SEM image of the $\text{CH}_3\text{NH}_3\text{PbI}_3$ sample) the temperature dependent absorption-edge measurements almost invariably resemble Figure 2.2b. The excitonic origin of the common features requires confirmation if excitonic binding energies are extracted by curve-fitting as in recent literature [72, 73, 76]. Apart from visual similarities, other evidence is also compelling. Grancini *et al.* [17] observe room-temperature excitonic signatures in recent pump-probe differential transmittivity measurements. Besides, a recent paper reporting the first broadband ultrafast photomodulated spectroscopy on these perovskites unravelled the *coexistence* of *excitons* and *free carriers* in $\text{CH}_3\text{NH}_3\text{PbI}_3$ upon photoexcitation [69] (by resolving the mid-IR band-like photo-induced absorption). Behaviour as material parameters vary provides additional evidence. In layered perovskites, binding energy and oscillator strength

increase as dimensionality reduces, with obvious 3D feature continuity [79, 105, 106]. Similarly, replacing I by Br reduces permittivity, enhancing excitonic features, as in Figure 2.3c.

Difficulty identifying alternative explanations provides further support, with high joint-density-of-states required over narrow energy ranges. In good-quality crystals, Shi *et al.* [107] fail to observe peaks (weak transmission through thick crystals possibly merging with a largely wavelength-independent background, explaining the unexpected saturation of extracted values at and above the absorption-edge). Attributing the lack of peaks to improved material [107] lacks support from other data, suggesting instead that peaks strengthen as material improves. D’Innocenzo *et al.* [36] report stronger peaks in better quality Cl-doped films than in pure iodide (see Figure 2.5). Our peaks for pure iodide are in turn stronger than reported by D’Innocenzo since prepared using techniques giving better crystal quality [46] (see Figure 2.4 and 2.5).

Although peaks suggest excitons can be generated rapidly at corresponding energies, this does not mean excitonic concentrations are necessarily high, with these rather depending on the rates of recombination and dissociation into unbound carriers [4].



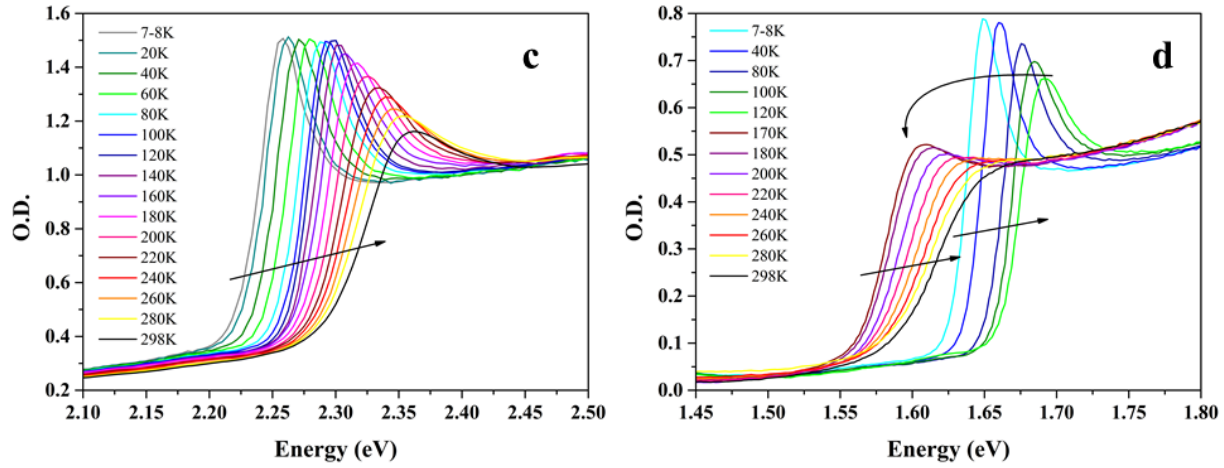


Figure 2.3 Theoretical absorption coefficient and experimental temperature-dependent optical density (OD) spectrum. (a) Solid black lines show the un-smeared theoretical absorption coefficient spectrum of Elliot [78], illustrating the discrete hydrogen-like excitonic transitions (up to three states shown) and the above bandgap correlated absorption. Red dash-dotted line depicts the corresponding uncorrelated above bandgap absorption correctly scaled (i.e. by a factor of $1/2\pi$ at $E-E_g \approx Ry_0$). The latter is a simple square root dependence of joint density of states on energy. (b) Lorentzian-only smeared version of Elliot's theoretical spectrum, showing the effect of various ratios of the full width at half maximum (FWHM or 2Γ) to the exciton binding energy (Ry_0). (c) Optical density spectrum of good quality $\text{CH}_3\text{NH}_3\text{PbBr}_3$ and (d) $\text{CH}_3\text{NH}_3\text{PbI}_3$ perovskite samples, both measured from room temperature down to 7-8 K. The arrows illustrate the direction of the absorption edge displacement with temperature (jump between 120-170 K for iodide is due to phase transition).

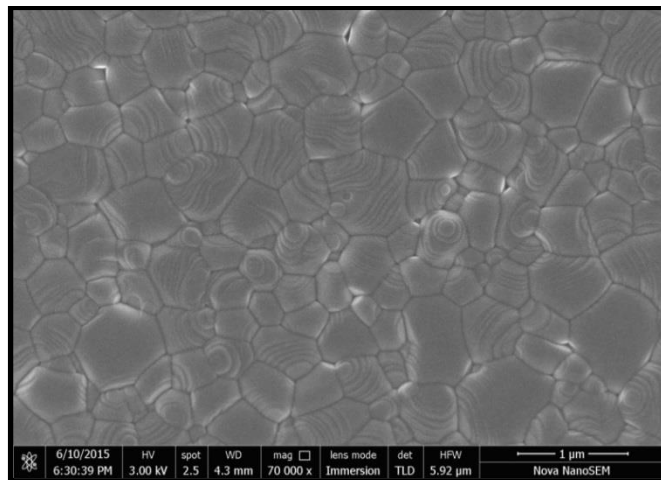


Figure 2.4 $\text{CH}_3\text{NH}_3\text{PbI}_3$ film morphology. The top-view SEM image of a $\text{CH}_3\text{NH}_3\text{PbI}_3$ film illustrating distribution of grains with 300-500 nm in size.

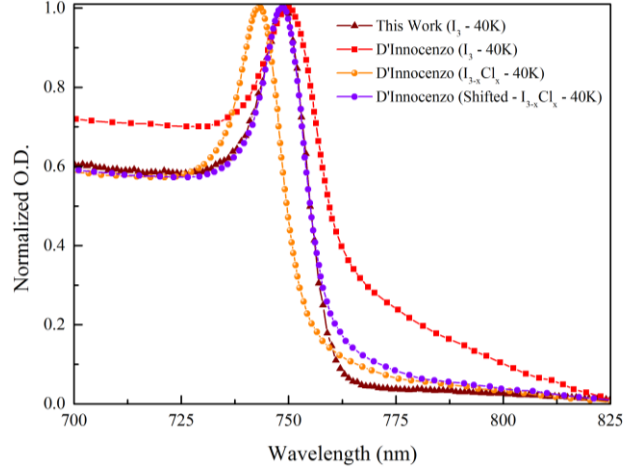


Figure 2.5 Material quality comparison with literature. Optical density spectrum at 40K of $\text{CH}_3\text{NH}_3\text{PbI}_3$ (red) and $\text{CH}_3\text{NH}_3\text{PbI}_{3-x}\text{Cl}_x$ (orange) reported by D'Innocenzo *et al.* [36] and $\text{CH}_3\text{NH}_3\text{PbI}_3$ (brown) used in this study are presented. The shifted spectrum of the $\text{CH}_3\text{NH}_3\text{PbI}_{3-x}\text{Cl}_x$ (purple) towards lower energies is provided for clear comparison of its spectrum broadening with that of the $\text{CH}_3\text{NH}_3\text{PbI}_3$. The comparison shows the high quality of the $\text{CH}_3\text{NH}_3\text{PbI}_3$ material used in this work with much smaller spectrum broadening than that of $\text{CH}_3\text{NH}_3\text{PbI}_3$ reported by D'Innocenzo in ref. [36] (i.e. indicative of its higher crystallinity). The broadening observed for the $\text{CH}_3\text{NH}_3\text{PbI}_3$ material in this work is also comparable to that of the $\text{CH}_3\text{NH}_3\text{PbI}_{3-x}\text{Cl}_x$ in ref. [36].

Additional support for excitonic origins would emerge if extracted binding energies agreed with theory. Ab-initio excitonic calculations pose challenges [72, 101], limiting calculations largely to hydrogenic, invoking effective masses and host medium permittivity. Wide-ranging literature values [35, 36, 72, 99, 108] result from perovskite permittivity varying enormously from microwave to optical frequencies as dipolar then ionic contributions wane [4, 108].

2.4.3 Carrier-phonon Interaction Consideration

More realistic calculations would include carrier-lattice interactions. Although not explored to any depth in the existing literature (by the time the corresponding article was published), carriers in these ionic perovskites will polarize the lattice. Carriers and induced polarization can be treated as quasi-particulate polarons [109], with properties depending on phonon coupling,

particularly with longitudinal optical (LO) phonons (involving positive and negative ions vibrating out of phase, creating strongly interactive electric fields [110]).

The literature on both polarons and polaronic excitons [37, 109-111] is generally limited to cases where the material hosts a single LO mode, while multiple external LO modes are expected for these perovskites. Hellwarth and Biaggio [37] provide insight into how such multiple LO modes might best be handled as an equivalent single mode, with these equivalent values able to “be used with confidence in existing polaron theories that only consider one LO mode”. They find that the equivalent LO mode coupling strength (W_e), in the related case of determining electron mobility, is reasonably treated as an accumulation of coupling strengths associated with all the LO modes (W_i) but is weighted by the strongest (square of equivalent coupling strength is equal to the sum of squares of individual coupling strengths):

$$W_e = \sum_{i=1}^m W_i^2 \quad (2.13)$$

However, the equivalent LO energy is biased towards the lower energy LO modes (one suggested algorithm gives the inverse square of equivalent LO energy (ω_{LOe}) equal to the sum of the inverse squares of the actual LO energies (ω_{LOi}) weighted by the square of the associated coupling strength, equation 2.14; another gives the inverse of the equivalent LO energy equal to the sum of the inverses of the actual LO energies weighted by the square of the associated coupling strength multiplied by a term depending on phonon occupancy, equation 2.15).

$$\frac{W_e^2}{\omega_{LOe}^2} = \sum_{i=1}^m \frac{W_i^2}{\omega_{LOi}^2} \quad (2.14)$$

$$\frac{W_e^2}{\omega_{LOe}} \coth(\beta_e/2) = \sum_{i=1}^m \frac{W_i^2}{\omega_{LOi}} \coth(\beta_i/2) \quad (2.15)$$

where $\beta_e \equiv \hbar\omega_{LOe}/k_B T$ and $\beta_i \equiv \hbar\omega_{LOi}/k_B T$.

To calculate the binding energy of the 1S excitons created in a polar semiconductor in interaction with a cloud of virtual phonons (i.e. polaronic exciton problem), the variational functional approach of Kane [111] was adapted which is applicable to weak- and intermediate-coupling modes. Kane's formalism is a modified version of the Pollman-Büttner [112] perturbation theory method in which renormalization of the optical frequency dielectric constant and bare effective masses for static dielectric constant and polaronic masses is accounted for, respectively, in the weak-coupling regime whereas, Pollman-Büttner only considered the former renormalization.

The critical fundamental physical parameters of the material influencing the generated excitonic binding energy in such polar medium are the effective mass ratio of the charge carriers, permittivity with and without ionic contributions (ϵ_{ion} and ϵ_{∞} respectively) and relevant longitudinal optical phonon energy. Due to the uncertainty associated with the calculated/measured above-mentioned parameters in the literature (provided in Table 2.2), regions of plausible exciton binding energy values are calculated instead. To calculate the exciton binding energy and its corresponding single effective LO phonon energy, subsequent to finding the appropriate electron to hole bare effective mass ratio in Table I of Kane's seminal paper, the unknown parameter in Eq. 47 [111] was calculated through which the binding energies can be directly calculated using Eq. 46. Thereafter, the corresponding LO phonon energies from Eq. 51 of ref. [111] was calculated.

Based on the polaronic exciton theory of Kane [111], giving reasonable experimental agreement for other materials, Figure 2.6a shows calculated binding energies for $\text{CH}_3\text{NH}_3\text{PbI}_3$ and $\text{CH}_3\text{NH}_3\text{PbBr}_3$ as a function of effective LO energy, band-edge bare (rigid) effective masses and permittivity (both with and without ionic contributions). LO energies in these perovskites are not yet well-established, even for better-studied [113] inorganic CsPbCl_3 . Despite larger methylammonium (MA) ionic radius, the MA ion is lighter than Cs (molar mass 36.1 versus 132.9). For external lattice phonon modes, where the MA ion vibrates as a unit, higher

frequencies would be expected than for corresponding Cs compounds. Additionally, MA ions introduce internal modes at frequencies greater than 280 cm^{-1} [114], related to vibrational modes of isolated ions [115].

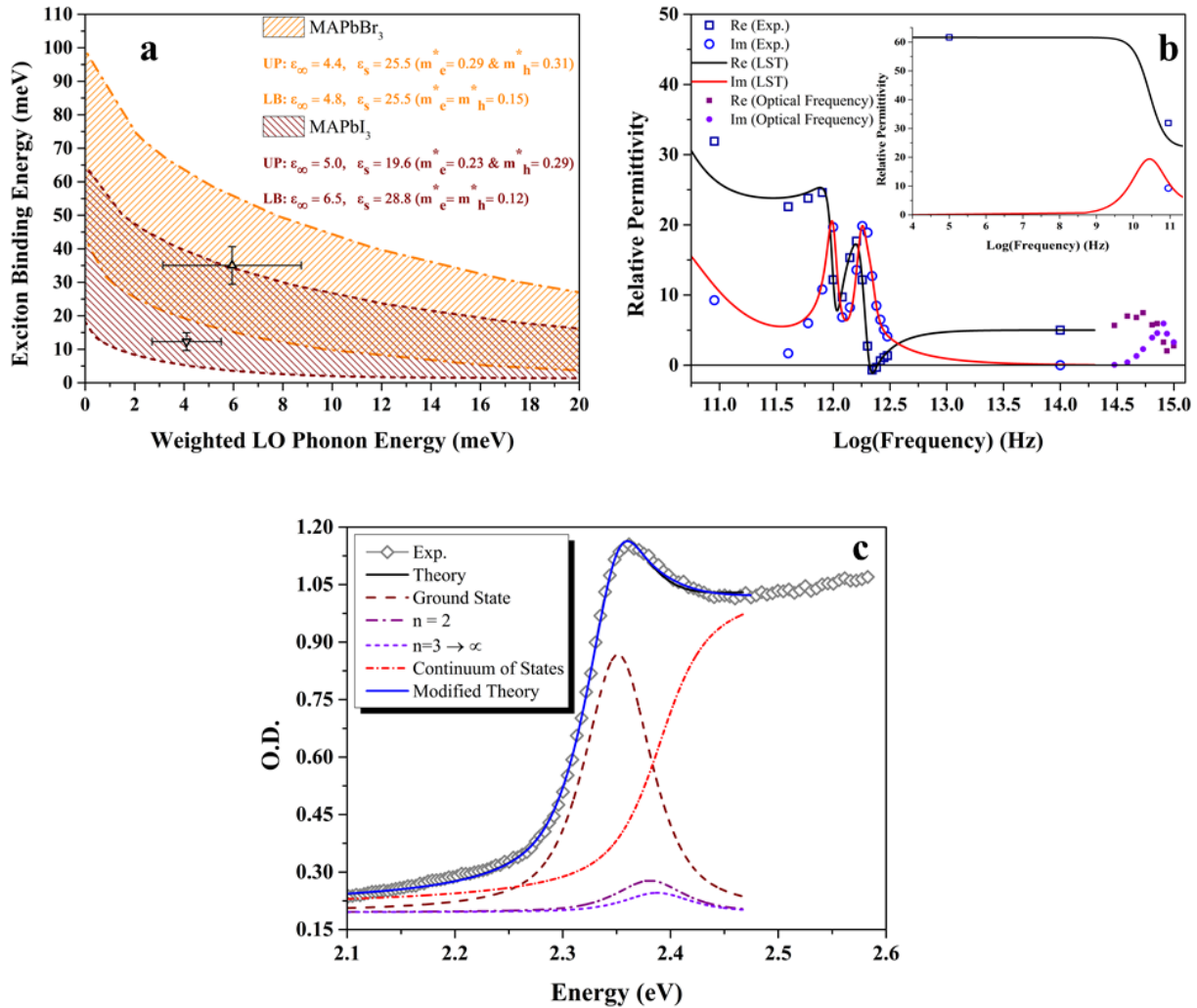


Figure 2.6 Exciton-polaron interactions, fit to the relative permittivity and decomposition of the absorption band-edge fit. (a) The exciton binding energy ranges depicted for $\text{CH}_3\text{NH}_3\text{PbI}_3$ (brown backward hatched area between short-dashed curves) and $\text{CH}_3\text{NH}_3\text{PbBr}_3$ (orange forward hatched area between dash-dotted curves) are due to the uncertainty associated with literature values of the calculated/measured carrier bare effective masses and dielectric constants. Further details on the references from which the basic physical parameters are extracted are provided in Table 2.2. (b) Experimental real (open dark blue squares covering the range from 10 kHz to 100 THz; filled purple squares illustrate optical frequency range including near-infrared (NIR) range (800-2500 nm) with

permittivity of $\epsilon_\infty \approx 5.1$) and imaginary (open blue circles covering the range from 10 kHz to 100 THz; filled violet circles show optical frequency range) components of the relative permittivity at 298 K fitted by equation 2.17 of the text. Solid black and red lines are the real and imaginary parts of the fit by LST theory, respectively. (c) Optical density spectrum band-edge decomposition of $\text{CH}_3\text{NH}_3\text{PbBr}_3$ at room temperature. The actual Elliot theory is homogeneously broadened with pseudo-Voigt profile (black solid line) with its decomposed discrete and continuum components illustrated. The FWHM is $2\Gamma = 73.6$ meV. Blue solid line is the theory convolved with pseudo-Voigt profile and further modified using scaled broadening of the states via equation (2.12). The optimum FWHM values for the excitonic ground state and continuum of states – as the free parameters – are $2\Gamma_X^{(1)} = 74.2$ meV and $2\Gamma_C = 65.2$ meV, respectively. The exciton binding energy obtained using the modified theory is $Ry_0 = 42.9 \pm 3.4$ meV.

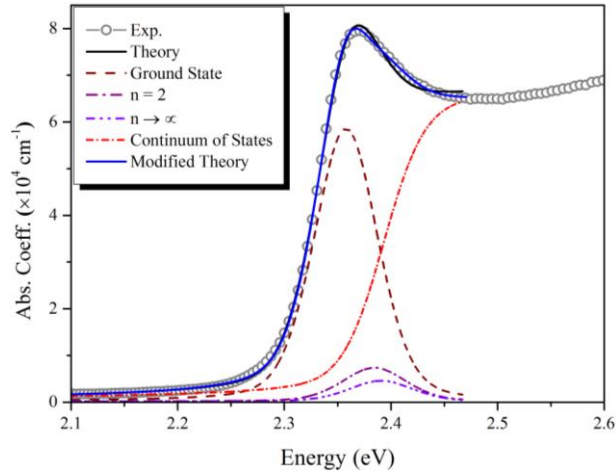


Figure 2.7 $\text{CH}_3\text{NH}_3\text{PbBr}_3$ room temperature absorption coefficient spectrum band-edge decomposition and fit assessment. The actual theory is homogeneously broadened with p-Voigt profile (black solid line) with its decomposed discrete states and continuum of states components illustrated. The effective exciton binding energy, FWHM and band gap are $Ry_0 = 37.2$ meV, $2\Gamma = 72.0$ meV and $E_g = 2396.2 \pm 1.4$ meV. Blue solid line is the theory convolved with p-Voigt profile and further modified using scaled broadening of the states as explained in equation (2.12). The optimum FWHM values for the ground excitonic and continuum of states – as the free parameters – are $2\Gamma_X^{(1)} = 66.9$ meV and $2\Gamma_C = 50.1$ meV, respectively. Effective exciton binding energy and electronic band gap are $Ry_0 = 39.6$ meV and $E_g = 2397.5 \pm 1.4$ meV, respectively.

Table 2.2 References to the physical parameters used in the theoretical Ry_0 calculation presented in Figure 2.6a.

		ϵ_∞	ϵ_{ion}	m_e^* and m_h^*
$\text{CH}_3\text{NH}_3\text{PbI}_3$	Upper Bound	Theory [116]	Experiment [117]	Theory [118]
	Lower Bound	Experiment [35, 81]	Experiment [83]	Theory [104]
$\text{CH}_3\text{NH}_3\text{PbBr}_3$	Upper Bound	Theory [108]	Experiment [83]	Theory [108]
	Lower Bound	Experiment [81]	Experiment [83]	Scaled according to lower bound of carrier mass ratio of triiodide

The number of external and internal normal modes can be derived from combined symmetries of lattice and molecular groups [115], at least in orthorhombic phases, with this number decreasing as temperature and structural symmetry increase. The ideal high temperature cubic structure (Space group 221), assumed by room temperature $\text{CH}_3\text{NH}_3\text{PbBr}_3$, has no Raman-active external modes but three triply-degenerate infrared-active external modes [119], each splitting into a doubly-degenerate TO and an LO mode in polar material. In reduced symmetry phases, both atoms/unit cell and phonon modes increase, similar to a zone-folding effect. The likely room temperature $\text{CH}_3\text{NH}_3\text{PbI}_3$ phase (Space group 140, rather than its subgroup 108) has 8 triply degenerate infrared-active and 7 Raman external modes [119].

Since translational symmetry is destroyed when MA ions distribute randomly between allowed orientations, evaluating phononic properties from high-temperature Raman and infrared measurements poses difficulties (as was also recently identified by Walsh's group [114]). Selection rules are invalidated as demonstrated for $\text{CH}_3\text{NH}_3\text{PbCl}_3$ where distinctive Raman

peaks in the orthorhombic phase disappear in the tetragonal [120]. Phonons from the entire Brillouin zone can contribute to Raman signals, nullifying strong resonances. Evidence for $\text{CH}_3\text{NH}_3\text{PbI}_3$ dissociating under high-intensity Raman illumination creates further uncertainties, with Raman features attributed to by-products [121], specifically PbI_2 .

Permittivity provides an alternative path to deducing LO energies. In ionic materials, the generalized Lyddane-Sachs-Teller (LST) relationship [122] links low and high frequency permittivity (ϵ_∞) through radial frequencies of infrared-active LO and TO phonons ($\omega_{\text{LO}i}$ and $\omega_{\text{TO}i}$, respectively, with broadenings of $\Gamma_{\text{LO}i}$ and $\Gamma_{\text{TO}i}$):

$$\epsilon(\omega) = \epsilon_\infty \prod_i \frac{(\omega_{\text{LO}i}^2 - i\omega\Gamma_{\text{LO}i} - \omega^2)}{(\omega_{\text{TO}i}^2 - i\omega\Gamma_{\text{TO}i} - \omega^2)} \quad (2.16)$$

Chaves and Porto [122] maintain that the formal basis of equation (2.16) evaporates when internal motion defying description by independent damped oscillators is present, such as internal molecular rotations. They derive a more general relationship encompassing dipolar, ionic and electronic components of present interest:

$$\epsilon(\omega) = \epsilon_\infty \frac{i\Gamma_{\text{Ld}} + \omega}{i\Gamma_{\text{Td}} + \omega} \prod_i \frac{(\omega_{\text{LO}i})^2 + (\Gamma_{\text{LO}i}/2)^2 - i\omega\Gamma_{\text{LO}i} - \omega^2}{(\omega_{\text{TO}i})^2 + (\Gamma_{\text{TO}i}/2)^2 - i\omega\Gamma_{\text{TO}i} - \omega^2} \quad (2.17)$$

where Γ_{Ld} and Γ_{Td} are the relaxation frequencies associated with order-disorder kind of mechanisms (similarly described by Debye relaxation) occurring in the microwave range or lower frequencies of ferroelectrics [122]. This factorized model capable of describing asymmetric modes requires $\Gamma_{\text{Ld}} > \Gamma_{\text{Td}}$ (see Table 2.3). $\text{CH}_3\text{NH}_3\text{PbI}_3$ permittivity has been measured from 20 Hz to 1 PHz [4, 35, 117], with data well described by this formula (Figure 2.6b), at least when contributions below 10 kHz from ion migration are excluded [35, 123]. Two phonons were detected in THz measurements [117], although best fit to the wider data range arises if 4 TO-LO pairs are considered, with fitting parameters in Table 2.3. From this fit, LO

phonon energies and coupling strengths can be determined ($= \omega_{LOi} - \omega_{TOi}$), giving an effective polaronic LO energy of $33.1 \pm 11.3 \text{ cm}^{-1}$ ($4.1 \pm 1.4 \text{ meV}$) from both earlier algorithms (uncertainty is estimated from 3 and 5 phonon fits to these data). For $\text{CH}_3\text{NH}_3\text{PbBr}_3$, effective LO energies are higher since Br is lighter (experimentally supported value 1.45 times higher [121]). The effective LO energy calculated here is consistent with the values very recently reported (after the article corresponding to this chapter was published [20]) by Diab *et. al* for $\text{CH}_3\text{NH}_3\text{PbI}_3$ single crystals [40] and by Kumar *et al.* for $\text{CH}_3\text{NH}_3\text{PbBr}_3$ polycrystalline thin films [124] measured from fittings to the temperature-dependent photoluminescence spectra line-width broadening.

Table 2.3 Optimum fitting parameters in equation (2.17) used to fit the experimental permittivity data presented in Figure 2.6b (the figures are in THz).

Modes	ω_{LOi}	ω_{TOi}	Γ_{Li}	Γ_{Ti}	Γ_{Ld}	Γ_{Td}
1	0.9054	0.0035	2.5645	2.4438	0.0722	0.0275
2	1.0476	0.9969	0.2412	0.2768		
3	1.2066	1.0476	2.0538	0.8349		
4	1.2950	1.2066	1.1620	0.7028		

2.4.4 Comparison of Theory with Experiment

To complete comparison with theory, experimental binding energies were deduced simply by fitting equation (2.8), including pseudo-Voigt broadening [102], to optical densities of Figures 2.3c and 2.3d. Figure 2.6c illustrates the good fits obtained over the selected fitting range, showing small but systematic deviations near excited exciton state energies (see Figure 2.7 for fit to the absorption coefficient spectrum of $\text{CH}_3\text{NH}_3\text{PbBr}_3$). These could be due to non-

hydrogenic excited states arising from anisotropic effective masses, different broadening for different states, or additional unmodeled absorption, such as from LO phonon replicas of excitonic features. Although introducing additional parameters improves fits, the minimal parameter model of equation (2.9) was retained since there was insufficient physical basis for refinement and also the impact upon the extracted binding energy was relatively small. The only fitting parameters are bandgap E_g , ground state binding energy Ry_0 , broadening FWHM (2Γ) and the pseudo-Voigt Lorentzian fraction. Values so extracted for Ry_0 , FWHM and E_g are shown in Figures 2.8a to 2.8d, with pseudo-Voigt fraction in Figure 2.11.

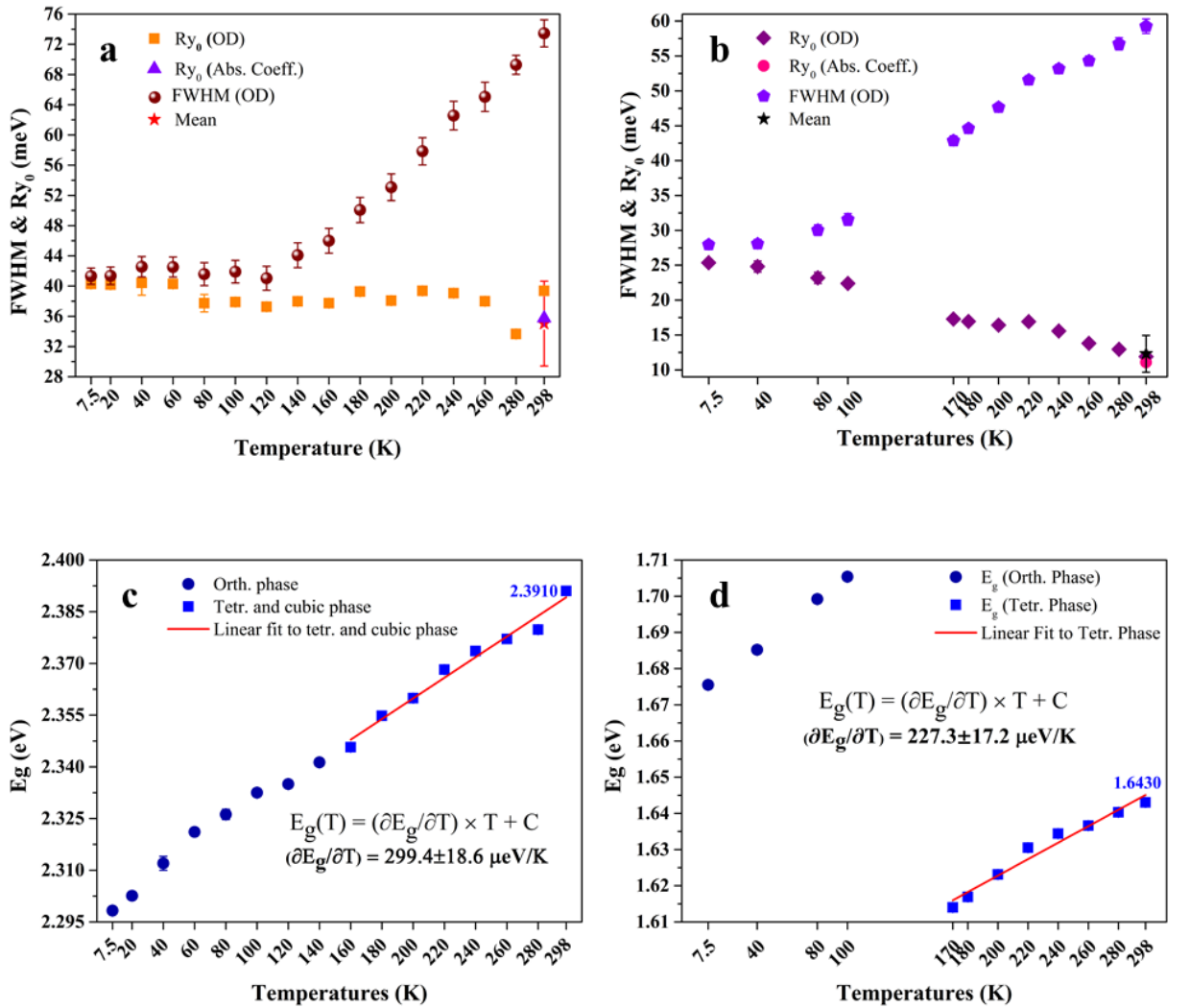


Figure 2.8 Temperature-dependent variation of exciton binding energy, broadening and bandgap of $\text{CH}_3\text{NH}_3\text{PbBr}_3$ and $\text{CH}_3\text{NH}_3\text{PbI}_3$. (a and c) Parameters are obtained by fitting the band-edge of

experimental OD spectrum in Figure 2.1c. (a) Brown circles and orange squares show FWHM and effective Rydberg values, respectively. The violet triangle indicates the exciton binding energy value from the absorption coefficient spectrum by the non-modified theory (corresponding to Figure 7). (c) Variation of the bandgap with temperature from 7 K to 298 K, with a linear function used to fit the temperature range above 140 K (encompassing tetragonal and cubic phases). Error bars reflect 95% confidence intervals of fitting parameters of the nonlinear least-square fit, rather than total measurement uncertainty. (b and d) Parameters are obtained by fitting the band-edge of experimental OD spectrum in Figure 2.2d. (b) Violet pentagons and purple rhomboids show FWHM and effective Rydberg values, respectively. The pink circle symbol indicates the exciton binding energy value from the fit to the absorption coefficient spectrum (see Figure 2.9). The star symbol is the mean value obtained from a collection of RT data presented in Figure 2.12. (d) Variation of the band gap with temperature in the orthorhombic and tetragonal phases is shown with the latter phase fitted by a linear function. The numbers depicted in (c) and (d) are, respectively, the bandgaps of $\text{CH}_3\text{NH}_3\text{PbBr}_3$ and $\text{CH}_3\text{NH}_3\text{PbI}_3$, obtained by fitting the absorption spectrum at RT.

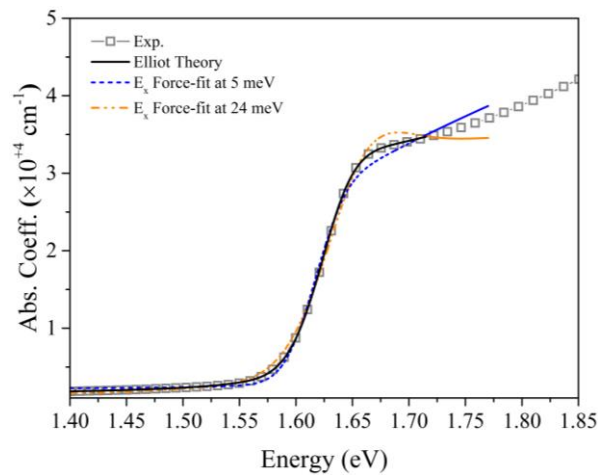


Figure 2.9 $\text{CH}_3\text{NH}_3\text{PbI}_3$ Absorption coefficient spectrum band-edge fit assessment at room temperature. (a) Absorption coefficient of $\text{CH}_3\text{NH}_3\text{PbI}_3$ (grey open square) was measured using spectroscopy ellipsometry at room temperature. Black solid line shows the actual fit to the band-edge with effective Rydberg of 11.1 ± 0.1 meV. Blue short dash and the orange dash-dot dot lines illustrate force-fitted theoretical spectrum by R_{y0} of 5.0 meV and 24.0 meV, respectively. These values are half and double that of the optimum effective exciton binding energy. The FWHM and band gap are set as free parameters in the force-fits.

Figure 2.10 shows the effect of sample storage in a nitrogen purged glovebox upon the extracted exciton binding energy values. Also demonstrated is the insensitivity to use of absolute absorption coefficient values or optical density data.

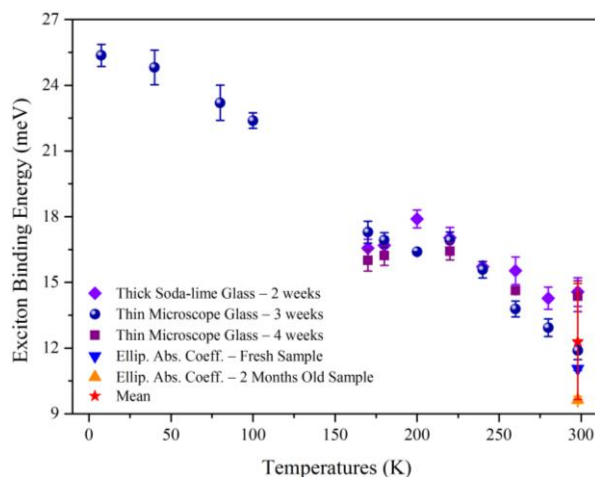


Figure 2.10 Temperature-dependent exciton binding energy of $\text{CH}_3\text{NH}_3\text{PbI}_3$ thin films measured on different substrates and at various times after fabrication. The exciton binding energies are obtained from optical density at various temperatures and from absorption coefficient only at room temperature. The perovskite film was deposited on two different types of glasses namely, soda-lime and normal microscope glass. In addition, exciton binding energies were collected at various times after sample deposition. The RT mean value is presented by red star symbol and the 95% confidence interval is calculated via student's t-test.

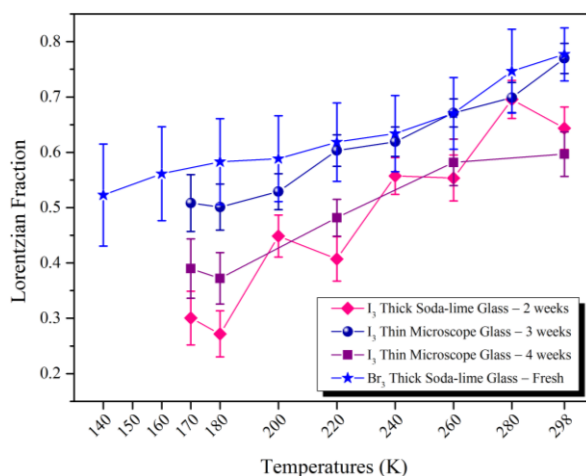


Figure 2.11 Lorentzian contribution to the pseudo-Voigt broadening of the absorption spectrum.

The increasing contribution of the Lorentzian broadening profile – or the corresponding decreasing contribution of the Gaussian broadening – with temperature to the pseudo-Voigt profile by which the theoretical spectrum is smeared is illustrated for $\text{CH}_3\text{NH}_3\text{PbI}_3$ and $\text{CH}_3\text{NH}_3\text{PbBr}_3$ perovskites. The data are presented for the room temperature tetragonal phase of $\text{CH}_3\text{NH}_3\text{PbI}_3$ and tetragonal and cubic phases' temperature range ($\geq 140^\circ\text{C}$) of $\text{CH}_3\text{NH}_3\text{PbBr}_3$.

For $\text{CH}_3\text{NH}_3\text{PbBr}_3$, extracted binding energies are largely temperature independent with room temperature value of 35.0 ± 5.6 meV. This is in accordance with the recent finding that the excitons are present even at room temperature for single crystals of tribromide perovskite [125]. For $\text{CH}_3\text{NH}_3\text{PbI}_3$, binding energy of 25.4 ± 2.8 meV is deduced for the low temperature orthorhombic phase, reducing to 12.3 ± 2.6 meV at room temperature, consistent with the recent work by Nicholas and co-workers [21]. FWHM is large even at low temperatures, as previously noted for these perovskites [126]. MA ions are ordered at such temperatures, necessitating explanations not involving changing orientation or translational symmetry violation, with strong LO phonon interaction one possibility [126, 127]. The distribution of grains with large defect density among the dominant high-quality crystals with the former resulting in apparent red-shift and broadening of the corresponding localized photoluminescence spectrum with noticeably lower carrier lifetime is supportive of the large spectrum bulk broadening [128]. These large broadening parameters prevent the appearance of the peaks associated with the exciton 2S state in steady state absorption measurement, with a relevant example of ZnS versus ZnSe, where the first excitonic excited state of the latter is clearly detected in its low-temperature absorption spectrum although having lower binding energy compared to the former, mainly due to the larger spectrum broadening of ZnS [59]. FWHM increases with increasing temperature, well described by a thermally-activated component with activation energy 57.9 meV for bromide and 24.1 meV for iodide (see Figure 2.12), an energy variously equated to exciton binding energy [36] and LO phonon energy. However, these values are apparently too high in the present case

for either. As shown in Figure 2.6a, experimental exciton binding energies are consistent with polaronic calculations, taking into account the effective LO phonon energy previously deduced.

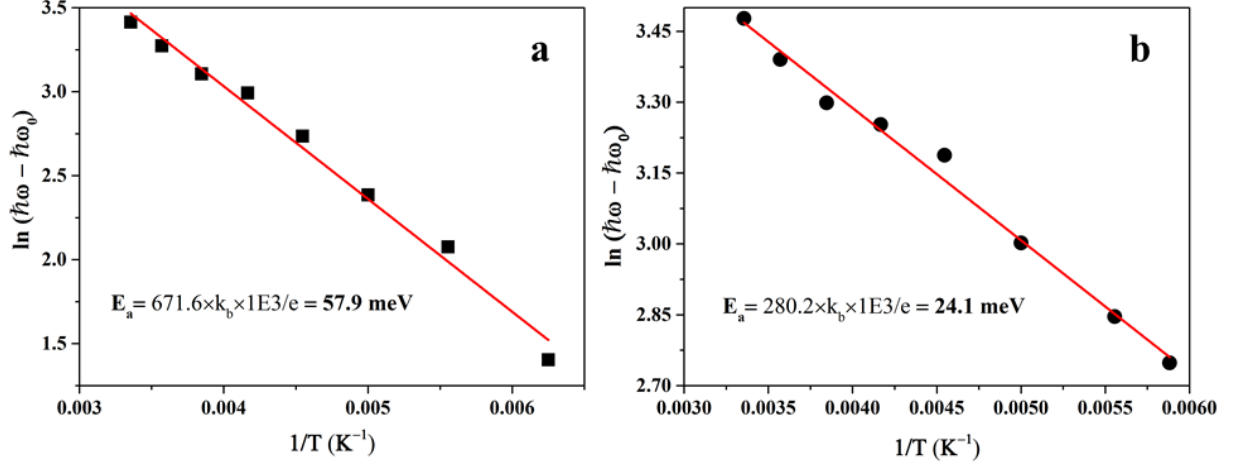


Figure 2.12 Thermally activated component of the absorption spectrum broadening. Linear fit to the natural logarithm of the difference between the absorption spectrum broadening ($\hbar\omega$) at a temperature and the intrinsic broadening at 7.5 K ($\hbar\omega_0$) with respect to the temperature inverse for triiodide (a) and tribromide (b) polycrystalline thin films.

Unlike tetrahedrally-coordinated semiconductors, bandgaps of both perovskites increase with temperature with this counterbalanced, for the iodide, by sudden reduction at the orthorhombic to tetragonal phase transition. In tetragonal and cubic phases, resulting bandgaps are (E_g in meV, T in Kelvin):

$$E_g(Br) = 2299 + 0.2994 \times T ; \quad E_g(I) = 1577 + 0.2273 \times T \quad (2.18)$$

Absorption thresholds, as often inappropriately determined by Tauc plots [4], lie at lower energies, since both binding energy and broadening contributions must be subtracted.

In summary, the results of this chapter show that polaronic effects are likely to play a major role in determining excitonic properties in organic-inorganic lead halide perovskites. Evaluating an effective LO phonon energy to describe these effects results in higher exciton binding energies than if only the highest energy LO phonons are considered. By including the polaronic effects

theoretical binding energy values which fall intermediate between the extremes of previous calculations, consistent with experimental values deduced from the present high quality $\text{CH}_3\text{NH}_3\text{PbBr}_3$ and $\text{CH}_3\text{NH}_3\text{PbI}_3$ samples, are obtained.

3 Electro- and photo-luminescence Imaging of Perovskite Solar Cells

3.1 Background

Light absorption, upon illumination of a solar cell, is the first step towards its operation. The absorption spectrum and its coefficient are important factors in the determination of the extent of light which can be trapped in the active semiconductor layer creating extractable charge carriers. An important fundamental physical parameter which directly affects the strength of light absorption and would influence the fraction of the free carriers in the photo-generated species is the semiconductor exciton binding energy. The latter was elaborated for $\text{CH}_3\text{NH}_3\text{PbI}_3$ and its tribromide counterpart in the previous Chapter.

Also relevant to the band-to-band absorption coefficient, is the spontaneous emission (i.e. luminescence) radiated out of a semiconductor. There is a linear proportionality correlation between the two [129, 130] (the theory is presented and discussed in section 3.3 of the current Chapter). Analysis of photoluminescence (PL) intensity, emission caused by radiative recombination of the photo-generated charge carriers (created upon illumination), is an important technique that provides insight into the active layer quality and also the implied open-circuit of a solar cell. Spatial investigation of the luminescence intensity would then be useful to characterize full devices both for performance improvement and for long-term operational assessment.

Photoluminescence and Electroluminescence (EL) imaging characterization techniques have been widely used to spatially investigate the efficiency limiting factors of partially and fully processed solar cells [38, 131, 132]. By exploring the charge carrier radiative recombination properties, detailed information about the distribution of non-radiative recombination centres, resistive and optical losses in solar cells can be obtained [39, 131-133]. However, the

application of these techniques in understanding the electrical properties of PSCs is still being developed [39, 133-135].

Photoluminescence measurements are based on the detection of photons generated by radiative recombination of the photo-generated electron-hole pairs, the majority of them being in the form of free carriers in the $\text{CH}_3\text{NH}_3\text{PbI}_3$ layer [20]. The parallel competitor mechanism for radiative recombination is non-radiative carrier recombination such as: Shockley-Read-Hall recombination (SRH) [136-138], surface recombination at the interface between the perovskite and the charge carrier selective contacts [139], and higher order excitation density dependent Auger recombination [140].

Electroluminescence is based on the detection of photons generated from radiatively recombined charge carriers which are electrically injected into the active layer (i.e., $\text{CH}_3\text{NH}_3\text{PbI}_3$) of the solar cell upon applying voltage bias to the contacts. Imaging of the spatial distribution of EL intensity provides combined information regarding carrier recombination and series resistance (R_s). EL imaging has been used as a robust stand-alone characterization tool [141] for characterization of a wide range of thin film solar cells such as copper indium gallium selenide (CIGS) [132] and organic solar cells [142].

3.2 Experimental Methods

3.2.1 Materials

Chemicals were purchased from Alfa Aesar (lead iodide, 99.999%), Sigma-Aldrich (methylamine solution, hydriodic acid solution, 4-*tert*-butylpyridine, lithium bis(trifluoromethylsulfonyl)imide (LiTFSI)) and Luminescence Technology Corporation (2,2',7,7'-tetrakis-(*N,N*-di-4-methoxyphenylamino)-9,9'-spirobifluorene (Spiro-OMeTAD)) and used as received. FTO glass (3.2 mm thick, $8\ \Omega\ \text{sq}^{-1}$ sheet resistance) was purchased from Dyesol. Ultraviolet-curable resin (XNR5516ZB1) was purchased from Nagase ChemteX Corporation. $\text{CH}_3\text{NH}_3\text{I}$ was synthesized by mixing solutions of CH_3NH_2 (20 mL, 0.23 mol, 40

wt% in water) and HI (10 mL, 76 mmol, 57 wt% in water) in water (100 mL). After stirring for 1 h, all volatiles were removed on a rotary evaporator at 60 °C. The product was dried in high vacuum (10^{-5} bar) at 60 °C for 24 h.

3.2.2 Solar Cell Preparation

Device fabrication was performed according to a published procedure by Huang *et al.* [46] in which the $\text{CH}_3\text{NH}_3\text{PbI}_3$ layer of the solar cells was deposited via a gas-assisted fast crystallisation technique. Briefly, a dense titanium dioxide (c-TiO_2) blocking layer was deposited on a clean fluorine-doped tin oxide (FTO) glass by spray pyrolysis of a $\text{Ti}(\text{acac})_2(^i\text{PrO})_2$ (bis(isopropoxide)bis(acetylacetonato) titanium(IV)) solution (1:9 $\text{Ti}(\text{acac})_2(^i\text{PrO})_2$:isopropanol) at 475 °C. After cooling down to room temperature, a perovskite film was formed by spin coating a solution of $\text{CH}_3\text{NH}_3\text{PbI}_3$ in dimethylformamide (45 wt%, prepared from PbI_2 and $\text{CH}_3\text{NH}_3\text{I}$ in a molar ratio of 1:1) at 6000 rpm for 30 s with the assistance of a nitrogen flow (60 psi) after 2.5 s. The substrate was then annealed at 100 °C on a hotplate for 10 min. After cooling down to room temperature, a Spiro-OMeTAD solution in chlorobenzene (containing 40.8 mg Spiro-OMeTAD, 3.25 mg lithium bis(trifluoromethylsulphonyl)imide in 7.8 μL acetonitrile and 16.8 μL 4-*tert*-butylpyridine in 500 μL chlorobenzene) was spin coated on the perovskite film, followed by thermal deposition of 80 nm of gold. The device was then encapsulated by a cover glass with ultraviolet-curable adhesive inside a nitrogen filled glove box according to a procedure of Han *et al.* [143]. We note that all the devices used in this Chapter and the following Chapter were fabricated using the abovementioned method and were encapsulated so as to minimize the impact of oxidation and moisture on the measurements.

3.2.3 J-V Characterization

The current density-voltage (J - V) measurements were performed under AM1.5G illumination ($100 \text{ mW}\cdot\text{cm}^{-2}$) using an Oriel solar simulator (model 94023A) and Keithley 2400 source meter. The J - V measurements were made on a defined area using a 0.16 cm^2 mask with a circular

aperture (4.5 mm in diameter). In all measurements the voltage was swept between 1.2 and -0.1 V with a scan rate of 30 mV s^{-1} .

3.2.4 Steady-state Spectral Photoluminescence Measurement

Steady-state (time-integrated) photoluminescence (SSPL) was used to characterize the PL peak position and spectra broadening. SSPL measurements were performed with a 405 nm, 60 mW, 1.5 mm-diameter excitation beam and a Si CCD camera. A 442 nm long-pass filter was used to remove the excitation beam from detection.

3.2.5 Electroluminescence and Photoluminescence Imaging

For photoluminescence and electroluminescence imaging measurements, a commercial 1-mega-pixel silicon charge-coupled device (CCD) camera (Princeton Instruments, Trenton, NJ, USA) was used to detect the luminescence signal. A 750-850 nm bandpass filter was used prior to the camera collection lens to exclusively detect the emission from the perovskite active layer. A 630 nm red LED was used as the excitation light source for photoluminescence measurements with low irradiance at the device surface, up to 0.1 Sun-equivalent illumination intensity. The voltage bias was controlled by a Source Measurement Unit, Agilent Technologies, controlled via computer software. The whole imaging setup was located inside a light-blocking box.

3.3 Evaluating the Generalized Planck's Emission Law in Planar Structured Perovskite Solar Cells

Luminescence emission by direct and indirect transitions can be described by the generalised Planck's emission law [129, 144]. This generalisation is valid for optical transitions occurring between two bands of energy states that are separated by an energy gap and occupied according to separate thermal distributions, each characterised by separate quasi-Fermi energies [129, 145]. It has been derived theoretically and validated experimentally for direct [146] and for indirect [147] semiconductors. According to this emission law, the rate of spontaneous emission

$dr_{em}(\hbar\omega)$ of photons with energy between $\hbar\omega$ and $\hbar\omega + d\hbar\omega$ into a solid angle Ω is given by the absorption coefficient $\alpha(\hbar\omega)$ and the difference of the quasi-Fermi energies $\Delta\eta$ [145, 148]:

$$dr_{em}(\hbar\omega) = \alpha(\hbar\omega) \frac{c_\gamma D_\gamma \Omega}{\exp\left(\frac{\hbar\omega - \Delta\eta}{k_b T}\right) - 1} d(\hbar\omega) \quad (3.1)$$

where c_γ is the velocity of the photons in an emitting medium with a refractive index n ($c_\gamma = c_0/n$, where c_0 is the speed of light in vacuum), D_γ is the density of states per solid angle for photons in the medium, k_b is Boltzmann's constant and T is the temperature in kelvin. In the case where $(\hbar\omega - \Delta\eta) \gg k_b T$, such as in this study, Boltzmann approximation is valid and equation (3.1) can be written in a simpler form:

$$dr_{em}(\hbar\omega) = \alpha(\hbar\omega) \exp\left(\frac{-\hbar\omega}{k_b T}\right) c_\gamma D_\gamma \Omega \exp\left(\frac{\Delta\eta}{k_b T}\right) d(\hbar\omega). \quad (3.2)$$

The detected luminescence R_{det} can be determined by integrating equation 3.2 (or equally equation 3.1) and taking into account multiple reflections from both surfaces and the quantum efficiency of the detection system.

The value of $\Delta\eta$ in the absorber of a solar cell upon illumination represents a fundamental upper limit for the open circuit voltage of the device. For silicon solar cells the exponential relationship between PL intensity and $\Delta\eta$ has been used to extract quantitative implied voltages from partially processed cells. An exponential relationship of the form

$$R_{det} \propto \exp\left(\frac{qV}{k_b T}\right) = \exp\left(\frac{V}{V_{th}}\right) \quad (3.3)$$

is expected between R_{det} and the device terminal voltage V (where $V_{th} = kT/q$ is the thermal voltage), for the cases where there is no voltage drop over a series resistance. This relationship was experimentally demonstrated for silicon [147], amorphous silicon, CIGS and dye sensitized

[145] solar cells. We investigate the validation of this formalism for PSCs using both PL and EL imaging measurements in the following subsections.

3.3.1 Required Corrections to the Images

In the following the corrections needed in order to obtain reliable quantitative intensities for the measured PL and EL data are explained. Figure 3.1a presents luminescence spectra of a representative perovskite solar cell used in this study (see Figure 3.1b for the device structure). Both PL and EL spectra are shown; the PL measurement was performed with an incident photon flux of $2.2 \times 10^{16} \text{ cm}^{-2} \cdot \text{s}^{-1}$, corresponding to an electrical current density of $3.5 \text{ mA} \cdot \text{cm}^{-2}$ (about 0.1 suns), while the EL measurement was carried out using a forward bias voltage of 1.4 V. In order to compare between the two spectra, the EL peak intensity was scaled to match the PL peak intensity. Both emissions have a similar full-width at half maximum and a similar location of the peak intensity (783 nm); the peak position is in the range reported by others [149, 150]. Significant deviations between the spectra can be observed in the short ($< 750 \text{ nm}$) and long ($> 810 \text{ nm}$) wavelength ranges. To clarify this observation, the PL spectra of a test sample containing only an FTO and a compact titanium dioxide (c-TiO₂) layer was measured under the same light intensity. The relatively constant PL emission of this test structure in the wavelength range 735–810 nm and the long tail in the wavelength range above 810 nm explain the deviation between the PL and EL, since the FTO–TiO₂ structure emits luminescence only under illumination and not under forward bias voltage. As the quantitative analysis methods described in the paper rely on the luminescence from the active absorber of the solar cell, the optical filters set of the measurement system was designed to restrict the detected signal to the spectral range 750 nm to 850 nm in order to minimise the contribution of the FTO and c-TiO₂ to the total measured PL signal. In addition, for the signal detected in the 735–810 nm range, the contribution from the FTO–TiO₂ structure was subtracted at all the illumination intensities in this study.

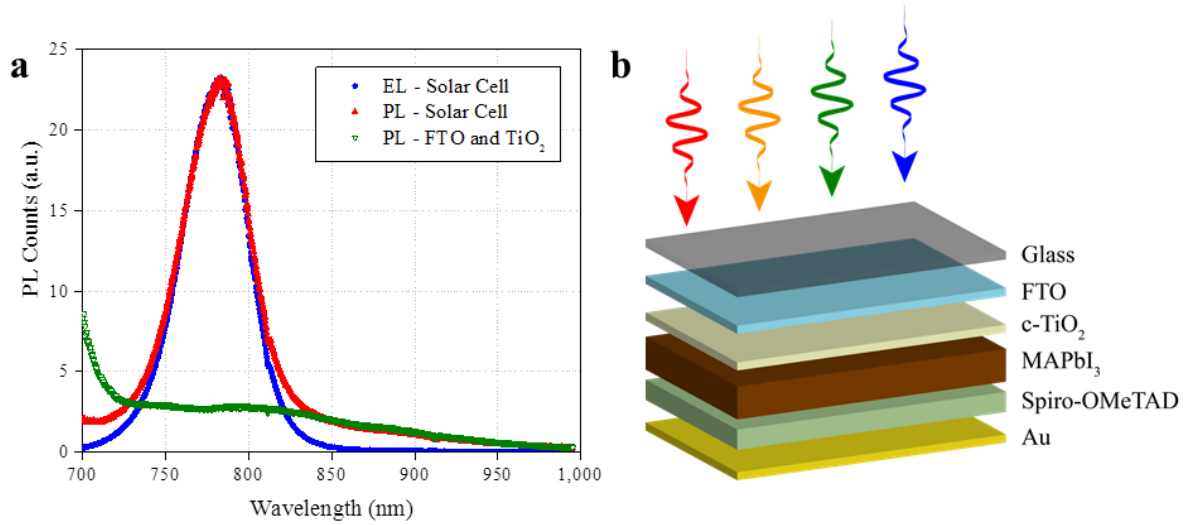


Figure 3.1 Spectral PL and device architecture. a) Luminescence spectra (EL and PL) of a completed perovskite solar cell and of the FTO–TiO₂ test structure. b) Schematic of the planar structured PSCs used in this chapter with glass/FTO/c-TiO₂/CH₃NH₃PbI₃/Spiro-OMeTAD/Au. The arrows show the direction of the incident light on the device.

3.3.2 Photoluminescence Measurement

To verify this relationship for perovskite-based solar cells, PL imaging measurements were performed and the average PL count (representing the detected PL intensity) from a fully processed cell was recorded together with the measured terminal voltage, while varying the illumination intensity between 0.1 and 0.02 suns. Details regarding the fabrication process of the solar cells and regarding the measurement system is given in the Experimental Methods section (section 3.2). Before the measurement, the solar cell was light soaked for approximately 20 min under 0.1 suns. Figure 3.2 plots the PL counts in arbitrary units (a.u.) on a semi-logarithmic scale together with a best fit to an exponential function (as expected from equation 3.3). The obtained good fit (open triangles and dashed line) verifies the exponential relationship between the PL and the terminal voltage. However, a larger exponential factor was calculated from the slope ($1.13 \times V_{th}$ instead of the predicted V_{th}). Spurious PL emission from non-active layers in the device (such as FTO and TiO₂) partly explains these deviations. In order to separate the PL of the active layers from the non-active layers, the PL emission of a FTO–TiO₂

test sample (i.e. an otherwise identical sample but with no active absorber) was measured at the same light intensities. The PL from the active layers was then determined by subtraction of the PL from the non-active layers (FTO–TiO₂) from the PL emitted by the perovskite solar cell. The good fit to an exponential function (filled symbols and solid lines in Figure 3.2) and the exponential factors in the range $1.05 \times V_{th} - 1.07 \times V_{th}$ verify the relationship between luminescence and voltage as predicted by equation (3.3). Note that although a small hysteresis was observed when performing the measurement from low to high intensity, a similar exponential factor was detected. This is the first time that this fundamental relationship is demonstrated for perovskite-based solar cells and the associated work was published in ref. [39]; this finding enables the use of the wide range of EL- and PL-based analysis techniques to perovskite cells.

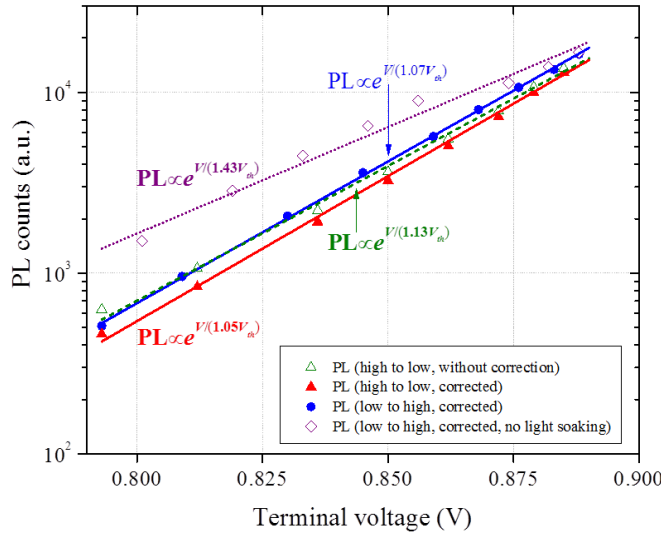


Figure 3.2 Photoluminescence versus internal voltage. PL counts as a function of terminal voltage for measurements: (open triangle) from high to low intensity (including the PL emission from the FTO and TiO₂); (filled triangle) from high intensity to low intensity after light-soaking the device; (filled circles) from low to high intensity after light-soaking the device; and (open diamond) from low to high intensity without a light soaking. For corrected values, the PL emission from the FTO and TiO₂ was removed.

The small deviation from the expected unity exponential factor can be related to insufficient light soaking. To highlight the remarkable effect that light soaking has on the determined factor

the measurement was repeated; however, this time no light soaking was performed. The FTO–TiO₂ corrected curve for the corresponding measurement is also included in Figure 3.2 (open diamonds). The relatively poor fit (dotted line) and the large exponential factor indicate that before light soaking the relationship between the luminescence and voltage departs from equation (3.3) in planar structured PSC. This can be explained by changes of the electrical field within the device [151, 152]. It can also be related to modification of material properties, such as bulk doping, due to illumination [136] and by light-induced electrical processes [153], such as previously proposed trap filling [136, 154] and ion migration [155-157]. Note that the measurements were done at light intensities below 0.1 suns so as to minimise temperature variations of the device.

3.3.3 Electroluminescence Measurement

Electroluminescence measurements with an applied forward bias in the dark were also performed on the same solar cell. The relationship between the average EL intensity and the applied forward bias voltage is shown on a semi-logarithmic scale in the insert of Figure 3.3 for a device without being light-soaked prior to EL measurements. The values substantially deviate from the straight line expected from equation (3.3). In a simplified equivalent circuit, a solar cell is described as a series connection of a diode representing the cell and a resistor, representing the finite series resistance R_s associated with current transport from the terminals to the absorber. The current I associated with a forward bias causes a voltage drop $R_s \times I$ across the series resistance and a corresponding deviation between the terminal voltage and the electrochemical potential difference at the absorber. Such series resistance effects can be compensated by plotting the measured luminescence intensity over the R_s -corrected forward voltage V_{corr} [i.e. $V_{\text{corr}} = V_{\text{forward}} - (R_s \times I)$]. Here R_s is used as a variable parameter; for this cell, the expected exponential relationship was found for $R_s = 19.2 \, \Omega$, which is within the range of R_s values determined from the current-voltage measurements. A similar exponential factor (1.06) as reported above for the PL data was determined. With this simple correction the exponential

dependence is confirmed and in addition the ability to extract quantitative series resistance information from luminescence data is demonstrated, an ability, which can be exploited further for spatially resolved R_s imaging of perovskite solar cells.

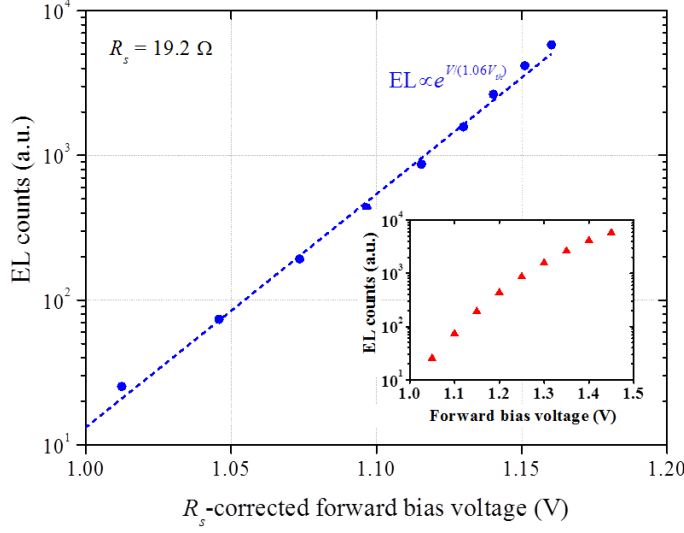


Figure 3.3 Electroluminescence versus internal voltage. EL counts as a function of the series resistance-corrected forward bias voltage [$V_{\text{corr}} = V_{\text{forward}} - (R_s \times I)$, where I is the measured current and $R_s = 19.2 \, \Omega$ for this solar cell]. The device was not light-soaked prior to the voltage biasing for EL measurements.

3.4 Luminescence Imaging as Fast Screening Technique of Layer Uniformity

In the previous section we confirmed the validity of the generalised Planck's emission law (equation 3.1) for PSCs using EL and PL imaging [39]. The generalised Planck's law describes the exponential correlation between the quasi-Fermi energy splitting and the luminescence intensity [39, 158]. According to the reciprocity theorem [159]:

$$\phi_{em}(E, \vec{r}) = EQE_{PV}(E, \vec{r}) \phi_{bb}(E) \left[\exp\left(\frac{qV_j(\vec{r})}{k_B T}\right) - 1 \right] \quad (3.4)$$

where the EL intensity, $\phi_{em}(E, \vec{r})$, at any position across the solar cell, \vec{r} , and for photon energy, E , is proportional to the photovoltaic external quantum efficiency, $EQE_{PV}(E, \vec{r})$, spectral photon density of a black body, $\phi_{bb}(E)$, and the internal junction voltage $V_j(\vec{r})$. q is the unit charge. According to Planck's law, a constant junction voltage results in a constant EL intensity (for specific E). However, the time-dependent behaviour of PL and EL in PSCs in the order of tens of seconds and longer [160-164], requires primary device stabilization (i.e., preconditioning) via poling (i.e., forward biasing) or light-soaking (LS) for this correlation to hold [39]. These imaging techniques have been also recently used to understand the influence of $\text{CH}_3\text{NH}_3\text{PbI}_3$ crystal size on device performance in mesoporous structure PSC [133]. A very recent study by Weber and colleagues [165] attempted to address the underlying reasons of hysteresis in planar and mesoporous structured PSCs using the full area photoluminescence imaging technique.

In this section, we have exemplified the application of EL/PL imaging techniques for the detailed analysis of PSC performance by connecting the device electrical parameters to the features visualized in the corresponding spatially-resolved luminescence images [166]. Planar structure PSCs with glass/FTO/c-TiO₂/CH₃NH₃PbI₃/Spiro-OMeTAD/Au architecture (see Figure 3.1b) were chosen for two reasons: (1) the interpretation of EL/PL images was expected to be less complex than for devices with a mesoporous structure having light scattering layer; and (2) the degradation of planar structures has been less intensely investigated in the literature [167]. Using this system, in the next section, we have further demonstrated the usefulness of EL/PL imaging for investigating the long-term performance of PSCs as the evolution of the solar cell electrical parameters is clearly reflected in the EL image.

We first investigated EL imaging as an independent and fast (equal or less than one second exposure times per image) technique to understand the underlying reasons for variation of the electrical properties between identically fabricated perovskite devices. Considering equation

(3.4), in polycrystalline semiconductors [132] such as organic-inorganic lead halide perovskites, where there is a grain-to-grain optoelectronic variation [51, 52], EQE_{PV} incorporates the variation of carrier recombination and optical losses on a micrometer length scale. The resistive losses integrated into the junction voltage are also spatially variable ($V_j = V_a - R_s \times I$ where V_a is the applied voltage at the terminals, R_s is total series resistance and I is the dark injected current). Luminescence emission detected within a pixel in these imaging techniques is performed on macroscopic scales and commonly averaged over small fraction of few millimetres square, which ideally allows the assumption of the spatial independency of EQE_{PV} . As such, the exponential dependence of EL emission on voltage junction dominates the detected EL signal, implying the importance of voltage drop over resistive losses [132]. Here, a comparison between two arbitrarily chosen devices in the same batch, demonstrates the application of the spatially-resolved EL imaging in linking the extracted electrical parameters from J - V measurements to features observed in their luminescence maps.

Figure 3.4a shows the relative difference in the electrical parameters of Cell 2 with respect to Cell 1 measured under forward and reverse voltage sweep directions. While the short-circuit current density (J_{SC}) of the two devices is very similar, indicating comparable active layer thickness and carrier collection efficiency, the fill factor (FF) shows the biggest relative difference among the electrical parameters with Cell 2 having an approximately 7% higher FF than Cell 1. Moreover, the FF of both devices is rather low compared to non-encapsulated devices with the same architecture and fabrication procedure. A decrease in FF upon encapsulation is generally observed and subject of ongoing investigations. In view of the slopes of the J - V curves of the two devices around open-circuit voltage (V_{OC}) and J_{SC} (provided in Figure 3.5) the major contribution to this difference originates from R_s as shown in Figure 3.4a. To gain insights into the causes for the difference in solar cell performance, EL and PL images of both devices are investigated in detail.

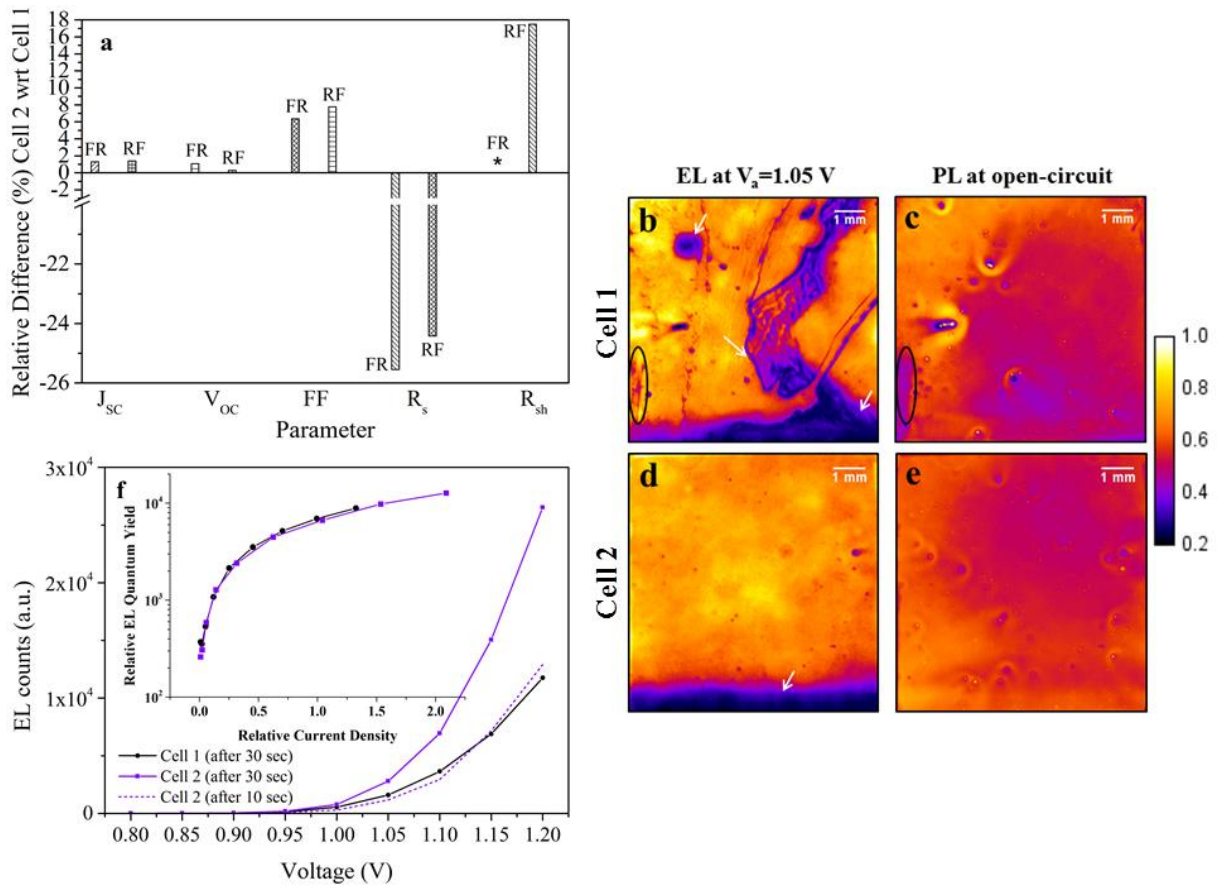


Figure 3.4 Solar cells photovoltaic parameter, relative EL EQE and EL and PL image comparison.

a) Relative difference in percent of the photovoltaic parameters of Cell 2 with respect to (WRT) Cell 1 measured under $V_{oc} \rightarrow J_{sc}$ (FR) and $J_{sc} \rightarrow V_{oc}$ (RF) scan directions at a scan rate of 30 mV/s. The series resistance is obtained from the slope of J - V curve near V_{oc} . For absolute values of the device electrical parameters see Table 3.1. b and d) EL images under forward voltage bias of 1.05 V for devices 1 and 2, respectively. c and e) PL images obtained under 0.04 Suns-equivalent light intensity ($\approx 8010^{13} \text{ cm}^{-3}$ carrier density) at open-circuit condition for Cells 1 and 2, respectively. The intensity of all images is normalized to the maximum intensity. f) Full-device averaged EL intensity evolution with voltage for Cells 1 and 2 (black line-circle and purple line-square curves, respectively), calculated from the images captured after 30 sec of biasing initiation; Purple dashed curve shows the evolution of EL intensity for Cell 2 with images captured after 10 sec. The inset depicts the relative quantum yield of the two devices with respect to their relative dark current density. *Using the linear fit approach to the J - V curve near the J_{sc} to extract the R_{sh} value for the FR scan direction, the calculated slope for both Cell 1 and Cell 2 showed very large error, thus the data were not included in the plot.

Cell	Sweep Direction	Sweep Rate (mV·s ⁻¹)	Eff. (%)	V_{oc} (mV)	J_{sc} (mA·cm ⁻²)	FF (%)	Condition
1	$V_{oc} \rightarrow J_{sc}$	30	10.09	981.1	21.31	48.27	Fresh
1	$J_{sc} \rightarrow V_{oc}$	30	7.86	974.4	21.13	38.17	Fresh
2	$V_{oc} \rightarrow J_{sc}$	30	10.99	991.7	21.59	51.33	Fresh
2	$J_{sc} \rightarrow V_{oc}$	30	8.61	977.1	21.42	41.14	Fresh
2	$V_{oc} \rightarrow J_{sc}$	30	9.79	1004.1	21.00	46.42	2 months
2	$J_{sc} \rightarrow V_{oc}$	30	8.16	1001.5	20.83	39.10	2 months
3	$V_{oc} \rightarrow J_{sc}$	30	10.81	1004.5	20.55	52.38	Fresh
4	$V_{oc} \rightarrow J_{sc}$	30	10.29	978.0	20.75	50.73	Fresh

Table 3.1 Device electrical parameters extracted from the J - V curves of solar cells 1, 2, 3 and 4.

Figures 3.4b and 3.4c present EL image of Cell 1 under 1.05 V forward voltage bias and PL at open-circuit condition (PL_{OC}), respectively. Figures 3.4d and 3.4e show the corresponding images of Cell 2. The spatial variation in PL_{OC} intensity commonly reflects the effective (i.e., bulk and surface) charge carrier recombination properties of the active layer material (i.e., CH₃NH₃PbI₃); a lower defect density results in a higher local voltage and brighter luminescence. As mentioned above, the EL signal is affected by the perovskite quality, shunting (e.g., when c-TiO₂ is in direct contact with the HTM), and also R_s . We note that severe shunting can also reduce the PL emission.

The more obvious, larger features are described first followed by the smaller features later in this section. The feature appearing as a dark strip at the bottom of the EL images of Cells 1 and 2 in Figures 3.4b and 3.4d, are near the isolation trench formed on the FTO-glass using laser scribe. The FTO layer is likely to be absent in this region and the underlying glass has experienced heat-induced damage before c-TiO₂ spray deposition [46], leading to a highly resistive region. These strips appear as an indistinguishably bright region under low-injection

PL measurement (see Figure 3.4c and 3.4e) demonstrating a negligible contribution from the perovskite layer to the feature. Photoluminescence images measured at short-circuit condition showed that these regions appear brighter than the rest of the device, supporting the notion that higher contact resistance in these regions has increased the local voltage (see Figure 3.5).

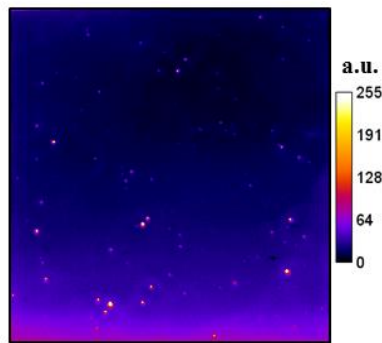


Figure 3.5 PL at short-circuit condition. Photoluminescence image of solar cell 2 measured at short-circuit condition. The intensity is in arbitrary units.

While the EL image of Cell 2 appears quite uniform (Figure 3.4d), prominent features (dark colour) can be seen in EL image of Cell 1 (see Figure 3.4b). As shown by Rau *et al.* [132] on large scale Cu(In,Ga)Se_2 solar cells, features in EL images are predominately due to resistive losses, both series and shunt resistances, whereas abrupt drops in EL intensity are usually related to pronounced local shunting [132, 168] which is dependent on the injection-level. The circular (top left area indicated with white arrow) and the fissure-like smeared dark regions appearing in the EL image (Figure 3.4b) of Cell 1 suggest that a highly resistive interlayer contact may exist which affects the EL but not the PL. We note that these features are likely to be a result of solution-based deposition of Spiro-OMeTAD rather than c-TiO_2 . More information can be deduced from the plot of EL quantum yield versus injected dark current density. The initial part of such a plot, in a semi-logarithmic form, which shows steep slope in perovskite solar cells [133], as illustrated in the inset of Figure 3.4f, is mainly dominated by the SRH recombination and shunting processes. We note that because the active area (i.e., deposited gold area) of the two devices are obtained from their EL images in equivalent resolution (i.e.,

pixel area), the current densities used in the inset of Figure 3.4f, and thus EL quantum yields, are presented in relative form by dividing the device-averaged EL counts by the corresponding relative current densities. No divergence between the curves associated with the two devices was found, in particular at low current injection levels. Therefore, the attribution of the features in the EL images of Cell 1 (Figure 3.4b) to shunting can be thoughtfully ruled out. In addition, if severe shunting existed, the abovementioned dark features would be observed in the PL_{OC} image (Figure 3.4c). A possible explanation for the large dark features in the EL image of Cell 1 is that they are regions with anomalously thin Spiro-OMeTAD layer, resulting in anomalously high sheet resistance, contributing to the total FF loss due to R_s of the device. The marginal difference in the relative EL quantum yield of the two devices, within the photovoltaic voltage working regime, corresponds well with the very similar V_{OC} of both devices (see Figure 3.4a).

The dark scratch-like feature appearing at bottom-left side in both PL_{OC} and EL images of Cell 1 (indicated with black oval in Figures 3.4b and 3.4c, respectively) most likely represents a region with damaged perovskite layer which in turn reduces the photo and electro-injected charge carriers concentration (i.e. reduces internal voltage).

The outcome of the EL mapping of the two solar cells is consistent with the results from J - V characterisation where the difference between the two devices mostly originates from the higher R_s of Cell 1 compared to Cell 2. This demonstrates the strength of the EL imaging technique in obtaining a comprehensive understanding of the performance limitations of PSCs within short time. To support the interpretations of Figure 3.4, similar analysis using the information extractable from EL imaging is provided in Figure 3.6 for two other solar cells fabricated following identical procedure but from a different batch of precursors.

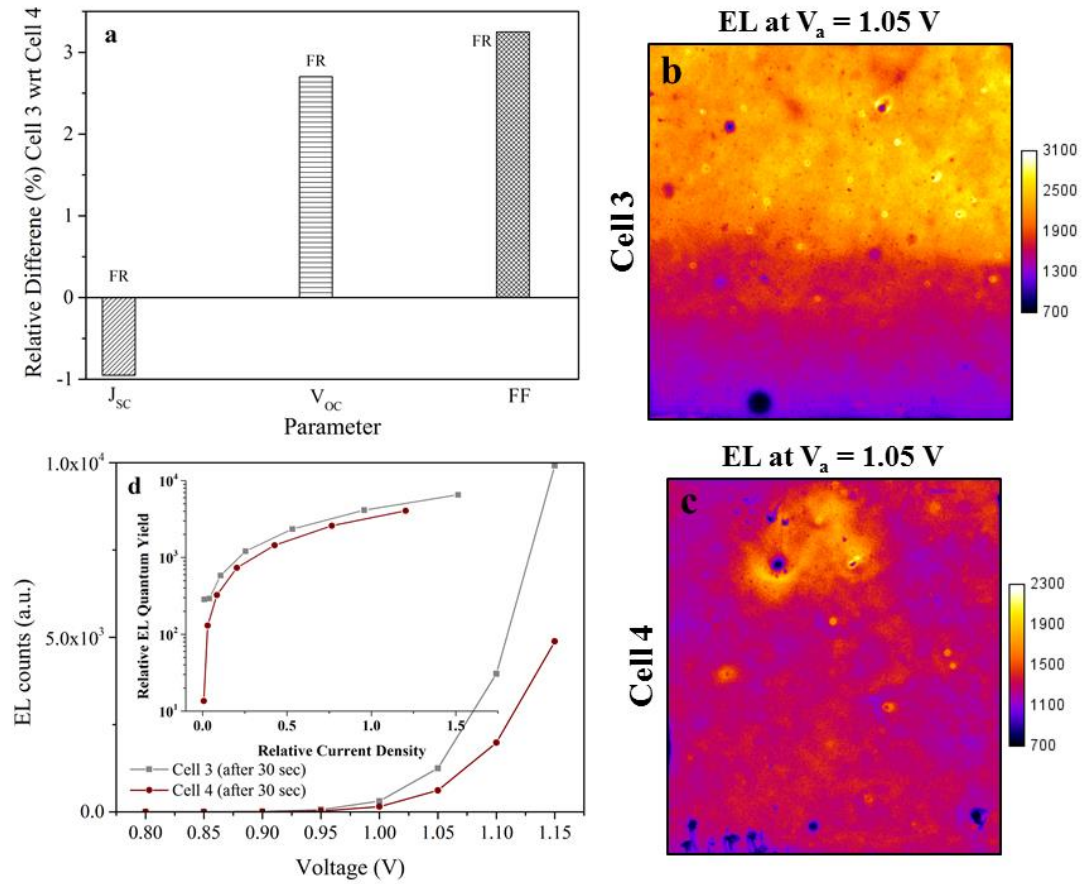


Figure 3.6 Solar cells photovoltaic parameter, relative EL EQE and EL and PL image comparison.

Similar data analysis as in Figure 1 of the main text for two different $\text{CH}_3\text{NH}_3\text{PbI}_3$ planar solar cells (i.e., Cell 3 and 4) fabricated following identical technique as Cell 1 and 2, using different batch of precursors. a) Relative difference in percent of the photovoltaic parameters of Cell 3 with respect to Cell 4 for $V_{OC} \rightarrow J_{SC}$ (FR) scan directions measured with scan rate of 30 mV/s. The series resistance is obtained from the slope of J - V curve near V_{OC} . For absolute values of the device electrical parameters see Table 3.1. b and c) EL images under forward voltage bias of 1.05 V for devices 3 and 4, respectively. f) Full-device averaged EL intensity evolution with voltage for Cells 3 and Cell 4 (grey square symbol and brown circle symbol, respectively), calculated from the images captured after 30 sec of biasing initiation; The inset depicts the relative quantum yield of the two devices with respect to their relative dark current density.

As an important side note, when comparing the EL intensity of different devices it is essential to collect the images after a fixed time of voltage bias initiation. For example, the images collected after 10 sec for Cell 2 (dashed purple curve in Figure 3.4f) should not be compared to the image

after 30 sec for Cell 1 (black curve in Figure 3.4f) as the EL intensity strongly increases with time.

3.5 Luminescence Imaging as Fast Screening Technique of Device Degradation in the Dark

Cell 2 was further used for investigating possible long-term changes in the EL/PL intensity upon storage in nitrogen atmosphere in the dark for two months. Figure 3.7a shows the J - V curves for Cell 2, fresh and aged. A summary of the changes in the electrical parameters of the device for the $V_{OC} \rightarrow J_{SC}$ (i.e. forward to reverse, FR) sweep direction is included in the inset table of Figure 3.7a. J - V measurements were done following identical procedure for the fresh and aged sample in order to exclude any undesirable effect caused by preconditioning of the solar cell [169, 170]. The least variation was observed in V_{OC} after two months suggesting a minimal change to the bulk properties of the perovskite layer. This is consistent with the unchanged peak position at ~ 773 nm and full-width at half maximum of the spectral PL of the fresh and aged device (see Figure 3.7f). The largest contribution to the power conversion efficiency reduction originates from the decrease in FF by $\sim 10\%$. To establish whether the change in device performance had an effect on the luminescence, EL images were collected at 1.05 V forward voltage bias (Figure 3.7b and 3.7c) and PL images at open-circuit (Figure 3.7e). By comparing the EL intensities of Figure 3.7b and 3.7c several findings are obvious: The small dark spots identified in Figure 3.7b which are ascribed to pinholes – confirmed by the optical microscope image shown in Figure 3.8 – have grown over time as evident from the EL image of the aged device in Figure 3.7c. As a result, some new spots became visible within the resolution of the EL image upon aging. Importantly, not only are the pinholes growing in size but it also seems that the surrounding $CH_3NH_3PbI_3$ degrades over time. This is exemplified in the zoomed-in PL_{OC} images (Figure 3.7e) of the spot identified with a rectangle in Figure 3.7b and 3.7c. The PL images also confirm the growth of the same pinhole discussed above. Although the

underlying mechanism of the pinhole growth and its surrounding degradation is not clear yet, its contribution to device performance is expected to be more likely a reduction in shunt resistance or an increase in ideality factor rather than influencing series resistance. However, since the V_{OC} does not degrade over time, the increased shunting effect is minimal and only observed as a reduced FF . Nevertheless, these findings highlight the importance of fabricating pinhole-free perovskite layers [171]. Another intriguing observation is that in addition to the inhomogeneous aging of the planar PSC, some regions of the device, for instance the top-left side, show improved EL intensity over time. A clearer picture is obtained by subtraction of the EL image of the fresh device from that of aged, shown in Figure 3.7d. A possible explanation for the EL enhancement in some parts of the device could be the shift in the current flow from the surrounding regions with higher local series resistance towards these more accessible regions. This explanation implies that it is unnecessary to invoke a change in the bulk material quality in the brighter EL regions, and this is consistent with the unchanged V_{OC} (see the Table inset in Figure 3.7a). It is evident from the subtracted image that the major part of the EL image has downgraded in intensity over time. By comparing this finding with the data obtained from J - V measurements (i.e. FF), it can be concluded that the EL images are dominated by resistance losses; suggesting that the performance loss upon aging mainly originates from changes of the perovskite/HTL and/or perovskite/c-TiO₂ interfaces affecting the R_s . Several studies have been dedicated to the understanding of the degradation mechanisms of neat CH₃NH₃PbI₃ films and its corresponding solar cells and the device stability improvement under different conditions [143, 160, 172-176]. Although the devices were stored in the dark in nitrogen-environment of a glovebox with a very low levels of O₂ (\approx 1 ppm) and H₂O (< 1 ppm), partial degradation of the perovskite layer from trace amounts cannot be fully excluded. The decrease in device performance may also be initiated by the very first J - V measurements and/or the forward biasing of the solar cell for EL imaging measurements. In both cases, the device experiences an electric field which was recently reported by Carrillo *et al.* to affect the charge carrier selective contact layers [177]. Although no long-term study was conducted in their work, it was proposed that

under electric-field the mobile ions in $\text{CH}_3\text{NH}_3\text{PbI}_3$ (i.e. mainly iodine ion [155, 177]) move towards the charge carrier selective contacts [156] and react reversibly with TiO_2 and irreversibly with Spiro-OMeTAD [177]. The latter permanent reaction was suggested to progressively deteriorate the conductivity of the HTL and affect the solar cell long-term performance, which is consistent with our observation of the FF degradation.

Notably, the subtracted EL image in Figure 3.7d reveals another feature: A dark circular area, 4.5 mm in diameter, which corresponds to the region where the device was illuminated during J - V characterisation using a round 0.16 cm^2 shadow mask. This fingerprint left after the J - V scan is to a large extent reversible, fading away after several hours [39], whereas the image in Figure 3.7b was collected six hours after the J - V measurement on the device. The mechanism behind the reversible illumination induced change in luminescence intensity, visible even several hours after light exposure, is unclear at this stage but it is further studied in the next Chapter.

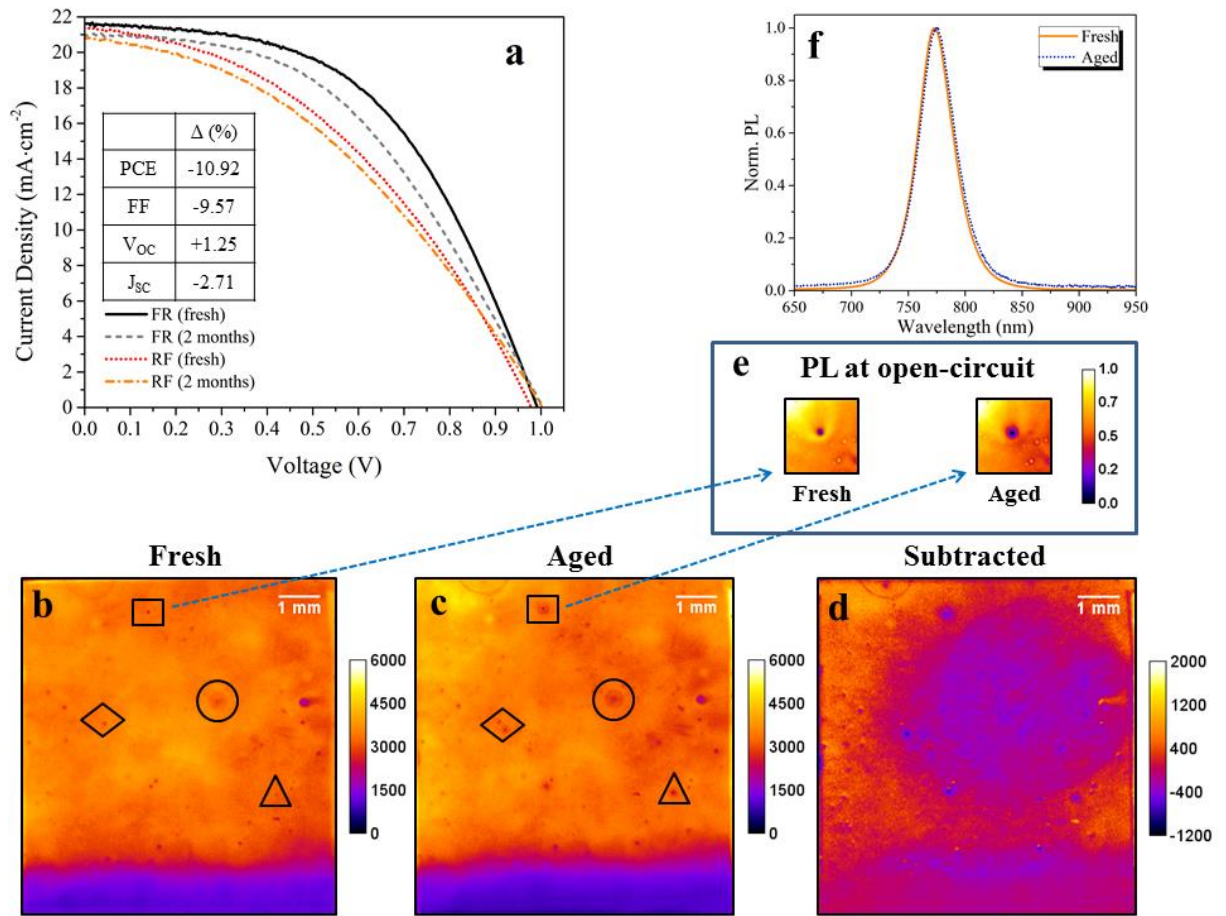


Figure 3.7 Fresh versus aged solar cell solar cell photovoltaic parameter, EL and PL image and spectral PL comparison. a) J - V characteristic curves of the fresh and two-months aged Cell 2 (stored in dark in glovebox); the inset table shows the change in the electrical parameters in percentage for the FR sweep direction. b and c) are the corresponding EL images of fresh and two-months aged device, respectively, both voltage biased at 1.05 V. Images are collected after 30 sec of bias initiation; the calibration bar shows the actual intensities. The inset (e) displays the normalized PL_{oc} images of the spot enclosed in a rectangle in part 3.2b and 3.2c. d) Subtracted image of the fresh device from the aged device. f) Normalized spectral PL of the fresh and aged solar cell.

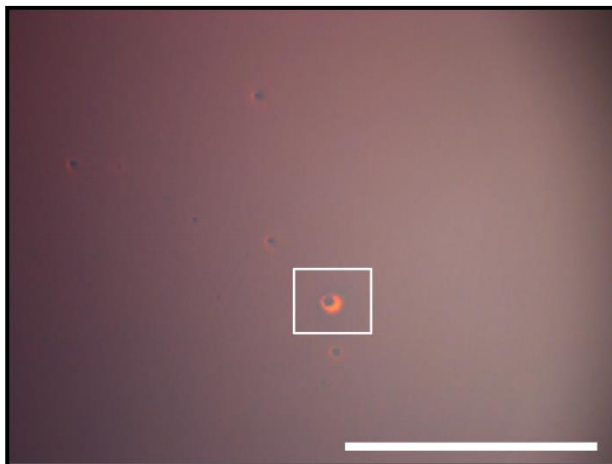


Figure 3.8 Optical microscope image of Cell 2. Optical microscope image of part of the Cell 2, showing the pinholes in the $\text{CH}_3\text{NH}_3\text{PbI}_3$ perovskite film; the scale bar is $100\ \mu\text{m}$. The square identifies the pinhole enclosed in a rectangle in Figure 3.7b and 3.7c. The image was taken from the two months aged device.

In summary, the application of fast and spatially resolved PL and EL full-device imaging techniques to perovskite solar cells which is in its developing stage is demonstrated in this chapter. It was shown that for $\text{CH}_3\text{NH}_3\text{PbI}_3$ -based planar perovskite solar cells the Planck's emission law with radiative ideality factor close to one can be achieved only when the device is pre-conditioned by light-soaking – due possibly to suppressing trap-mediated non-radiative recombination – and when luminescence from other layers of the device is taken into account. Detailed analyses of the luminescence images of planar solar cells were also performed to link the electrical parameters obtained from common current density-voltage measurements to the features observed in the spatially resolved luminescence images, in particular, EL images. Using EL imaging, it was further shown that pinholes are likely to act as a source of increased degradation over time even when devices were stored in a dry glovebox environment, pointing to the importance of developing pinhole free solar cells. Moreover, EL imaging is revealed to be a suitable technique to investigate the effect of reversible illumination induced changes in the device.

4 Illumination-induced Immediate Response and Long-term Evolution of $\text{CH}_3\text{NH}_3\text{PbI}_3$ Planar Perovskite Solar Cells

4.1 Background

The ease of fabrication, compositional versatility and astonishingly high power conversion efficiency (PCE) of perovskite solar cells (PSCs) has attracted the attention of many researchers worldwide [10, 178]. However, the main obstacle for PSCs field implementation is their long-term operational stability [3]. A large numbers of studies have investigated the underlying mechanisms of degradation in perovskite thin films and PSCs under various environmental conditions [6, 179]. However, there is no consensus on a complete description of these mechanisms. A few key findings from earlier works are outlined below.

Very recently it was proposed that the simultaneous presence of oxygen and photo-generated or electrically injected charge carriers is essential for a description of degradation in both perovskite thin films [180] and solar cells [175]. It was shown that humidity, in the absence of either oxygen or light, has a lesser impact on the degradation [175]. Non-encapsulated PSC architecture employing mesoporous aluminium oxide ($\text{mp-Al}_2\text{O}_3$), acting as the scaffold for perovskite deposition, on top of a thin compact TiO_2 (c-TiO_2), as the electron transport layer (ETL), was shown to increase the degradation rate compared to devices using c-TiO_2 and mesoporous TiO_2 (mp-TiO_2) as the ETL. This was attributed to an increase in the accumulation of free charge carriers in the perovskite layer and the formation of the degradation catalyst superoxide (O_2^-) [175, 180]. However, these findings are contrary to the mechanism proposed by Leijtens *et al.* [181] who concluded that $\text{mp-Al}_2\text{O}_3$ -based PSCs would have a more stable performance than mp-TiO_2 -based devices as a result of a lower ultra-violet (UV) light

absorption in the Al_2O_3 . This was expected to reduce deep trap formation in mp- Al_2O_3 which occurs through the reaction of desorbed oxygen (which is accelerated by absorption of UV photons) and photo-generated holes in mp- TiO_2 . Moreover, Leijtens *et al.* [181] suggested that TiO_2 trap passivation by oxygen is the major reason for the better long-term performance of non-encapsulated PSCs than encapsulated ones under solar illumination, including UV light. It has also been speculated that the migration of ions to the perovskite surface and their possible interaction with the hole transport layer (HTL) additives could form unprecedented trap states which cause the instability of the planar PSC in the long-term [177, 182].

Recently, it has been shown that Spiro-OMeTAD (either un-doped or doped with Li-TFSI) and methylammonium lead triiodide ($\text{CH}_3\text{NH}_3\text{PbI}_3$) are vulnerable to moisture-induced degradation, however, only at very high humidity [183]. In addition, it has been proposed that the ability of ions to transport through the perovskite polycrystalline thin film can be a source of intrinsic instability of the perovskite absorbers [177, 184, 185].

Photoluminescence (PL) and electroluminescence (EL) imaging techniques have proved extremely valuable in the silicon-based photovoltaic (PV) research and development [38, 186-188] for process optimization, efficiency improvements and degradation exploration. In addition, the short acquisition time of this method allows for its use for high throughput in-line inspection of wafers, solar cells and PV modules [132, 189].

Although employed and described in Chapter 3, since this technique, except for a few examples [39, 133, 135, 166, 190], is not widely used in the perovskite community we briefly outline it here. A PL image depends upon the spatial distribution of the charge carrier concentrations in a solar cell [191]. Assuming a relatively uniform absorbance across the perovskite absorber layer, the PL_{OC} image intensity (image taken under open-circuit condition) correlates with the variation of the photo-excited charge carrier effective lifetime since this determines the carrier concentrations. The effective lifetime is a measure of the impact of both the charge carrier bulk lifetime (the bulk perovskite) and the surface recombination rates of charge carriers (e.g. at the

perovskite/HTL or ETL/perovskite interfaces). In EL imaging, an external bias is used to inject charge carriers into the active layer via the selective contacts. These carriers pass through the contact barriers before recombining in the perovskite layer or at the interfaces. Therefore, the combined contribution of the transporting contact layer and interfacial contact resistance losses, in addition to the bulk recombination, is integrated into the EL signal.

Interfacial contact resistance has been recently shown to play a major role in limiting the fill factor (FF) of both conventional (illumination from ETL) and inverted (illumination from HTL) architectures [135, 166]. EL and PL_{OC} spatial intensity images at low charge carrier injection levels can also reveal the local shunt resistance. Change in the interfacial contact resistance (e.g. its reduction) results in an inverse response of EL (increase) and PL at short-circuit condition (PL_{SC}; decrease) intensities. Changes in shunt resistance, non-radiative bulk and surface recombination rates affect the EL and PL_{OC} signals in the same way.

4.2 Introduction

In the previous chapter we demonstrated the usefulness of EL imaging in resolving illumination-induced reversible phenomena in planar PSCs [166]. In the present chapter, luminescence imaging is used to track the fate of a selectively illuminated region, either under open-circuit condition or by sequential J - V measurements, on a planar structured PSC (see Figure 4.1a; the photo of a typical device used is shown in Figure 4.1b). This structure was chosen in light of the ongoing improvement of devices employing c-TiO₂ and Spiro-OMeTAD as the ETL and HTL, respectively [15, 192-198]. Further, the degradation of this PSC device architecture has been previously investigated [143, 199]. While PSCs employing organic selective contacts (i.e. PCBM, C₆₀ and PEDOT:PSS) can be used, they are known to undergo chemical reactions with the perovskite absorber layer when slow voltage sweep rates (such as during J - V measurements) are used and to be prone to degradation under relatively long light exposure durations [167, 169, 200, 201]. Firstly the changes in the spatial EL and PL intensity

maps immediately after their first exposure to illumination during J - V characterization are discussed. The evolution of the bulk absorber and interfaces are monitored over several days, while stored in a dark, oxygen- and moisture-free (both < 1 ppm) environment, are then discussed.

We demonstrate for the first time, the impact of light-induced changes using spatially-selective illumination, on the long term evolution of the perovskite layer and interfaces within encapsulated PSCs [202]. Spatially inhomogeneous deterioration at the c-TiO₂ interface is visualised by spatially resolved electro- and photoluminescence imaging and high-resolution focused ion beam-transmission electron microscopy (FIB-TEM) is applied to investigate structural changes.

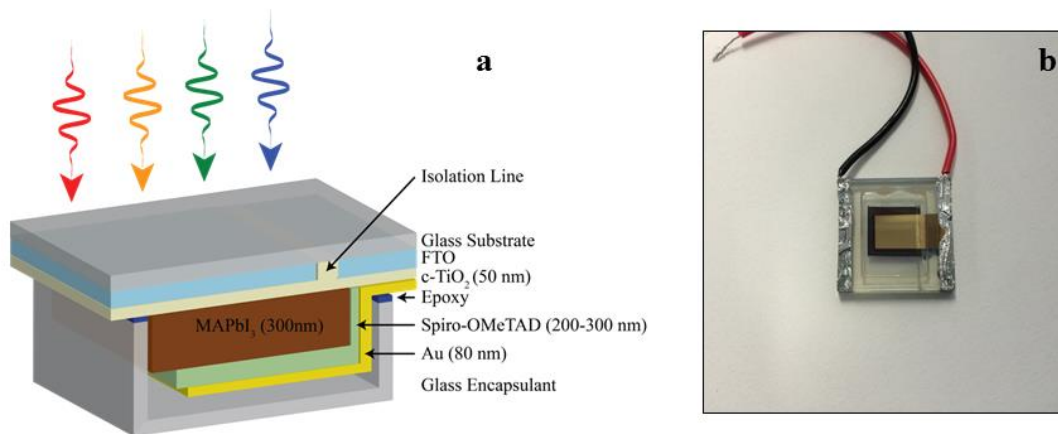


Figure 4.1 Device architecture. a) 3D schematic cross-section of the planar structure PSCs used in this study, also illustrating the edge-sealed encapsulation of the devices. The arrows show the direction of illumination. The layer thicknesses are provided in the brackets. The drawn layer thicknesses are not to the scale. In the following, all the images are oriented so that the isolation line close to the positive contact (gold; Au) indicated in this schematic is located at the bottom of the images. b) Image of an example device used in this study. Note the isolation line at the right hand side of the device near the positive contact. The schematic of this structure is drawn in (a) of the main text.

4.3 Experimental Methods

4.3.1 Materials

Chemicals were purchased from Alfa Aesar (lead iodide, 99.999%), Sigma-Aldrich (methylamine solution, hydriodic acid solution, 4-*tert*-butylpyridine, lithium bis(trifluoromethylsulfonyl)imide (LiTFSI)) and Luminescence Technology Corporation (2,2',7,7'-tetrakis-(*N,N*-di-4-methoxyphenylamino)-9,9'-spirobifluorene (Spiro-OMeTAD)) and used as received. FTO glass (3.2 mm thick, 8 Ω sq⁻¹ sheet resistance) was purchased from Dyesol. Ultraviolet-curable resin (XNR5516ZB1) was purchased from Nagase ChemteX Corporation. CH₃NH₃I was synthesized by mixing solutions of CH₃NH₂ (20 mL, 0.23 mol, 40 wt% in water) and HI (10 mL, 76 mmol, 57 wt% in water) in water (100 mL). After stirring for 1 h, all volatiles were removed on a rotary evaporator at 60 °C. The product was dried in high vacuum (10⁻⁵ bar) at 60 °C for 24 h.

4.3.2 Solar Cell Preparation

Device fabrication was performed according to Section 3.2.2.

4.3.3 J-V characterization

The current density-voltage (*J-V*) measurements were performed under AM1.5G illumination (100 mW·cm⁻²) using an Oriel solar simulator (model 94023A) and Keithley 2400 source meter. The *J-V* measurements were made on a defined area using a 0.16 cm² mask with a circular aperture (4.5 mm in diameter). In all measurements the voltage was swept between 1.2 and -0.1 V with a scan rate of 30 mV s⁻¹.

4.3.4 Electro- and photoluminescence Imaging

Photoluminescence imaging measurements were performed at 1 mW cm⁻² excitation intensity using a red LED array with central wavelength of 635 nm (i.e. $\sim 2.1 \times 10^{13}$ cm⁻³ photo-excited charge carriers density). Unless otherwise stated, all the images were collected after 40 sec of

photo- (PL) or electro-excitation (EL), with very short exposure times of 1 sec (for EL) or less (for PL).

4.3.5 Transmission Microscopy Measurement

The TEM samples were prepared using the XP200 FIB to make a cross-sectional Lamella. The Lamella was then extracted using an ex-situ micromanipulator and deposited on continuous-carbon copper TEM grid so that we could perform TEM measurements (using Philips CM200).

4.4 Regular Measurement Conditions and Procedures

The following points are general instructions applicable to all the measurements performed in this study and provided here in order to avoid repetition throughout this chapter:

- All the devices used in this study were encapsulated according to Han *et al.* [143] so as to minimize the impact of oxidation and moisture on the prolonged device storage and measurements.
- All the solar cells used in this study if not being used for characterization, have been stored in dark, oxygen-free (< 1 ppm) and moisture-free (< 1 ppm) environment of standard glovebox.
- Aperture area of the mask used for selective illumination of the device, either during open-circuit light-soaking or J - V measurement is $\sim 0.16 \text{ cm}^2$ (i.e. diameter of 4.5 mm).
- The PL and EL images stated as the “immediately after” J - V measurements or LS were performed after about 10 minutes from the time J - V measurement or LS was completed.
- For the PL imaging purpose the excitation wavelength was 635 nm with illumination intensity of 1 mW cm^{-2} .
- Photo-excitation respective electro-excitation during PL and EL imaging measurements were only performed for one minute at each and every stage of device monitoring.

- All the EL and PL images were collected after 40 seconds from the voltage biasing and illumination initiation, respectively.

In this study, we have minimized the impact of preconditioning (i.e. accumulative effect of photo-induced or voltage bias-induced E-field creation across the device) on the image response of the solar cells by using individual cells for EL and for PL imaging investigations.

4.5 Results and Discussion

In the following we adopt a simple notation to clarify the results. The ratio between the luminescence intensity at a time, t , and the intensity of a pristine device is denoted as

$R_m(t) = I(t)/I(0)$, where m indicates the luminescence technique ($m = \text{PL}_{\text{OC}}$, EL or PL_{SC}) and I is the luminescence intensity.

4.5.1 Initial Effect of Light Current-Voltage Measurements

4.5.1.1 Cell 1: Comparison of EL and PL_{SC} after J - V measurements

Upon performing several J - V scans on Cell 1 (see Figure 4.2 for the related curves and electrical parameters), it was realized that the area associated with the circular aperture of the mask (4.5 mm in diameter, $\sim 16 \text{ mm}^2$ area) used to illuminate a defined area (henceforth named the aperture affected area; AA) of the device by AM1.5G ($100 \text{ mW}\cdot\text{cm}^{-2}$) illumination is brighter than its surroundings in the EL image, as illustrated in Figure 4.3a. This phenomenon occurs irrespective of the measurement procedure (i.e. scan direction or stabilized current measurement at maximum power point voltage). As the first step in understanding this behaviour, a PL image of Cell 1 under short-circuit conditions was collected and is presented in Figure 4.3b. The AA appears darker than the surrounding regions. Figure 4.3c presents the intensity profile of the line scan shown in Figures 4.3a and 4.3b.

Note that, due to the good conductivity of the FTO layer, the non-illuminated areas experience similar cyclic voltage variations as the illuminated areas, so changes are due to either the effect of illumination or the slightly different voltages seen by the two regions.

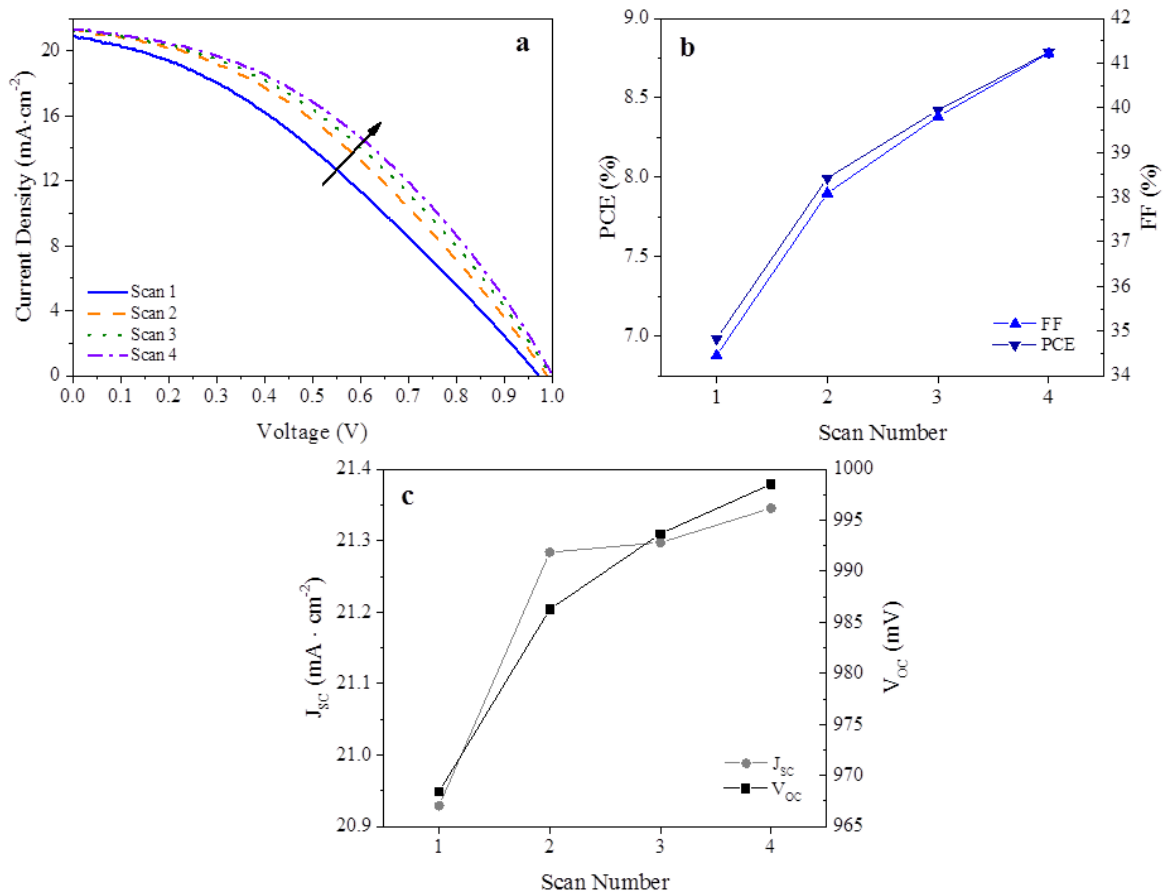


Figure 4.2 Photovoltaic parameters of Cell 1. a) J - V curves of four consecutive $J_{sc} \rightarrow V_{oc}$ (-0.1 V to 1.2 V) scans of Cell 1. Corresponding electrical parameters extracted from the J - V scans, FF and PCE in (b) and J_{sc} and V_{oc} in (c).

The origin of the brighter EL of AA could be twofold [166]: (i) decrease in the interfacial contact and/or bulk resistance; (ii) increase in the external quantum efficiency at long wavelengths (note equation 4.1). The latter, generally, reflects the active layer material ($\text{CH}_3\text{NH}_3\text{PbI}_3$) quality condition; encompassing information about the carrier diffusion length and the charge carrier recombination rates in the bulk and rear contact. The reduced PL_{sc}

intensity of AA in Figure 4.3b implies a lower series resistance or an increase in bulk and/or rear non-radiative recombination rates.

More insight can be obtained by considering the following formalism for the EL intensity $\phi_{em}(E)$, for photon energy E , with this intensity proportional to the photovoltaic external quantum efficiency, $EQE_{PV}(E)$, spectral photon density of a black body, $\phi_{bb}(E)$, and the internal junction voltage V_j (q , k_B and T are unit charge, Boltzmann constant and absolute temperature in Kelvin, respectively) [166]:

$$\phi_{em}(E) = EQE_{PV}(E)\phi_{bb}(E) \left[\exp\left(\frac{qV_j}{k_B T}\right) - 1 \right] \quad (4.1)$$

This equation is expected to hold in situations where $EQE_{PV}(E)$ is not strongly dependent on bias light intensity. The contrasting luminescence behaviour of EL and PL_{SC} spatial intensity images is suggested to be mainly due to a reduced vertical interfacial contact series resistance in the AA [39] (which affects V_j exponentially impacting EL intensity). The increase is also consistent with reduced bulk non-radiative recombination due to defect annihilation [153, 156], increasing $EQE_{PV}(E)$ at the long wavelengths where the highest intensity EL emission occurs. However, this would tend to increase PL_{SC}, in conflict with experimental data, unless overridden by decreased series R or increased rear surface recombination.

The reduced series resistance is explained by the decreased ionic contribution to the interfacial junction band-bending during illumination (as depicted later in Figure 4.23c) mainly at the c-TiO₂/CH₃NH₃PbI₃ contact [203, 204]. The reduced field at the interface increases the concentration of those carriers in the interfacial region that need to cross the interface, reducing the series resistance (see below the Mechanistic Interpretation section for complete description). This agrees well with the major enhancement in the fill factor (FF) rather than with the short-circuit current density (J_{SC}) or the open-circuit voltage (V_{OC}) of the devices upon consecutive J -

V measurements (see Figures 4.2, 4.5 and 4.9 for three planar PSCs prepared from different batches of precursor solutions).

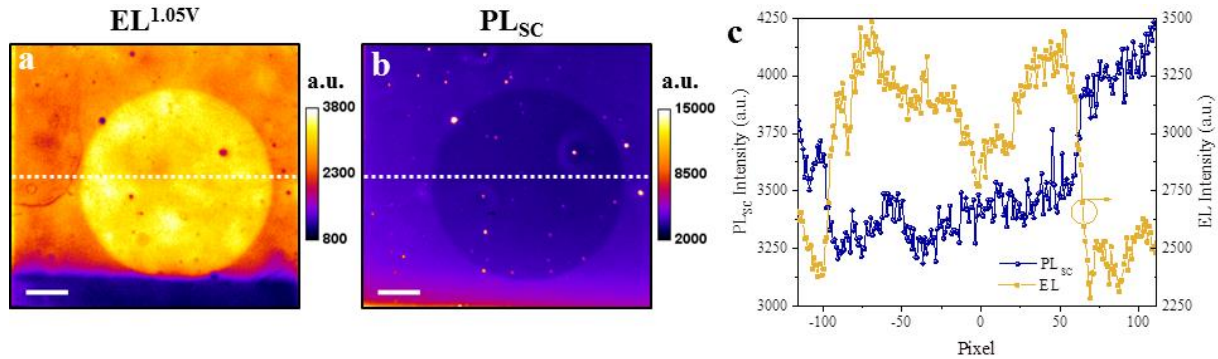


Figure 4.3 Effect of light exposure on the immediate EL and PL_{SC} response of PSC. a) EL image of Cell 1 measured after four times RF ($J_{SC} \rightarrow V_{OC}$) J - V scans from -0.1 to 1.2 V taken at 1.05 V and b) PL_{SC} image of the same cell. PL measurement was performed with a red excitation light source having a 635 nm central wavelength. The scale bars are 1 mm. c) PL_{SC} (blue circle data points) and EL^{1.05V} (gold square data points) intensity along the line scan shown in Figures 4.3a and 4.3b. The feature appearing as a dark strip at the bottom of the EL image in (a) is near the isolation trench formed on the FTO-glass using laser scribing. The FTO layer is likely to be absent in this region and the underlying glass has experienced heat-induced damage before c-TiO₂ spray deposition [46] leading to a highly resistive region [166]. PL_{SC} image in (b) shows that this region appears brighter than the rest of the device, supporting the notion that higher contact resistance in these regions has increased local voltage.

4.5.1.2 Cell 2: Comparison of EL and PL_{OC} after J - V measurements

To further explore changes in the bulk of the CH₃NH₃PbI₃ active layer, upon illumination, the J - V characteristics of pristine Cell 2 was measured over several scans in the FR ($V_{OC} \rightarrow J_{SC}$) direction with the data presented in Figure 4.4a (see Figure 4.5 for the extracted photovoltaic parameters). As explained above, regardless of the J - V measurement procedure, the EL intensity associated with the light-exposed region is enhanced compared to the surroundings. This is clearly demonstrated by plotting the ratio of the spatial EL^{1.15V} image of the J - V measured (Figure 4.4c) to that of the pristine (Figure 4.4b) device in Figure 4.4d. The PL_{OC} image of the

same device was recorded prior to and immediately after (Figures 4.4e and 4.4f) performing consecutive J - V scans.

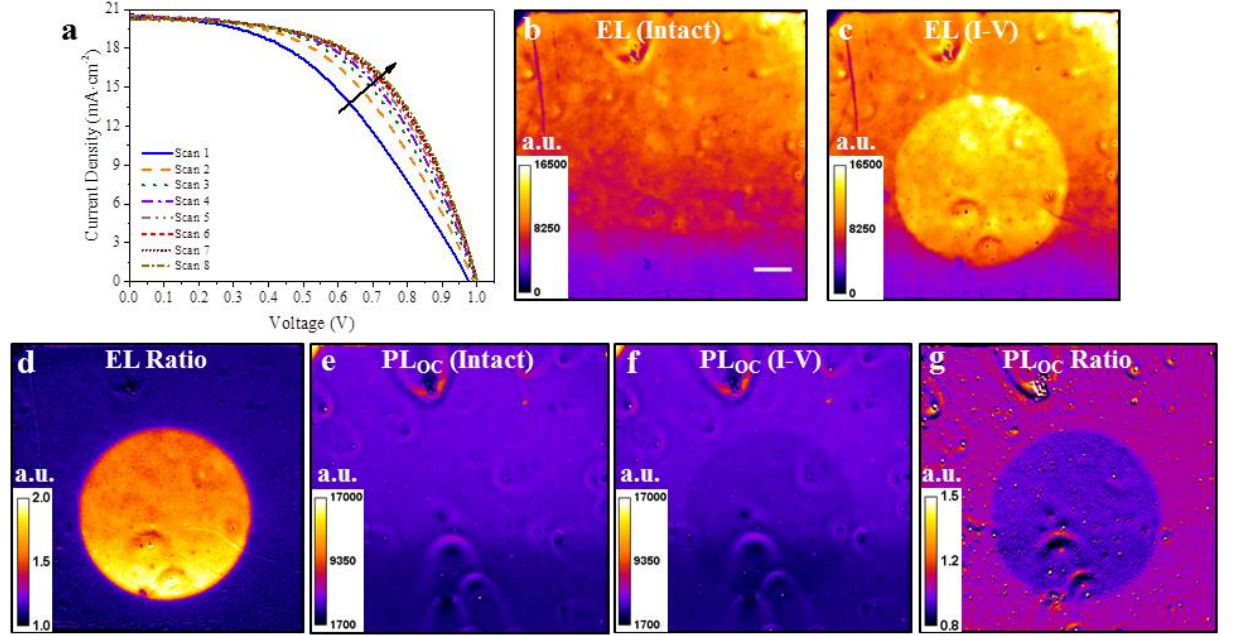


Figure 4.4 Effect of light exposure on the EL and PL_{OC} immediate response of PSC. a) Sequential J - V curves of Cell 2 measured for eight times in FR ($V_{\text{OC}} \rightarrow J_{\text{SC}}$) direction from 1.2 to -0.1 V with scan rate of 30 mV s^{-1} . EL intensity images of the same device under forward voltage bias of 1.15 V collected before (b) and immediately after (c) the consecutive J - V scans. Only the circular region (i.e. AA) was illuminated during J - V measurements while the rest of the device was masked. The corresponding ratio of the EL images of the measured device to the fresh device is shown in (d). PL_{OC} intensity images of the same device collected before (e) and immediately after (f) the consecutive J - V scans; together with the ratio image in (g). PL measurements were performed with a red excitation light source having a 635 nm central wavelength. The scale bar in (b) is 1 mm and applies to all the images in this figure.

Interestingly, when measured under open-circuit conditions, the corresponding spatially-resolved PL related to the AA appears darker than the rest of the device (see Figure 4.4f). This is more clearly observed in Figure 4.4g which shows the ratio image of Figures 4.4e and 4.4f. This behaviour indicates that the effective lifetime of the photo-excited charge carriers is reduced in the illuminated region. We suggest that the AA yields a quenched PL_{OC} intensity due to the increased interfacial non-radiative recombination of the minority carriers at the front

contact (c-TiO₂/perovskite interface according to Figure 4.1a) as will be shown in the next section. This would increase dark saturation current and would most likely reduce the EQE_{PV} in the short wavelength range of the spectrum for which charge carriers generation rate is concentrated near the c-TiO₂/MAPbI₃ interface. It is noteworthy that this increase in dark saturation current is small enough not to offset the increase in EL in this region, again attributed to reduced series resistance or the total photocurrent. The unfavourably increased surface recombination rate could arise from the newly formed non-radiative recombination centres during the illumination. One possibility is that defects are created within the several topmost layers of MAPbI₃ (close to the ETL) possibly facilitating the collapse of the perovskite structure into non-perovskite ones [205] (this probably cannot be detected by XRD measurement). The distorted perovskite structure is possibly the consequence of larger number of MA⁺ cations migrating from the cuboctahedral spaces in the illuminated region than the masked area, during J - V measurement (this will be further discussed in the Mechanistic Interpretation section). The persistence of the features observed in EL, PL_{OC}, PL_{SC} for several minutes (i.e. for at least 10 minutes after the end of the J - V measurement) allows us to rule out a recent mechanism postulating the formation of metastable trap states within the perovskite bandgap in the bulk perovskite upon light-soaking (LS) which recover at fast timescales [201], as a possible cause of the decrease in luminescence intensity.

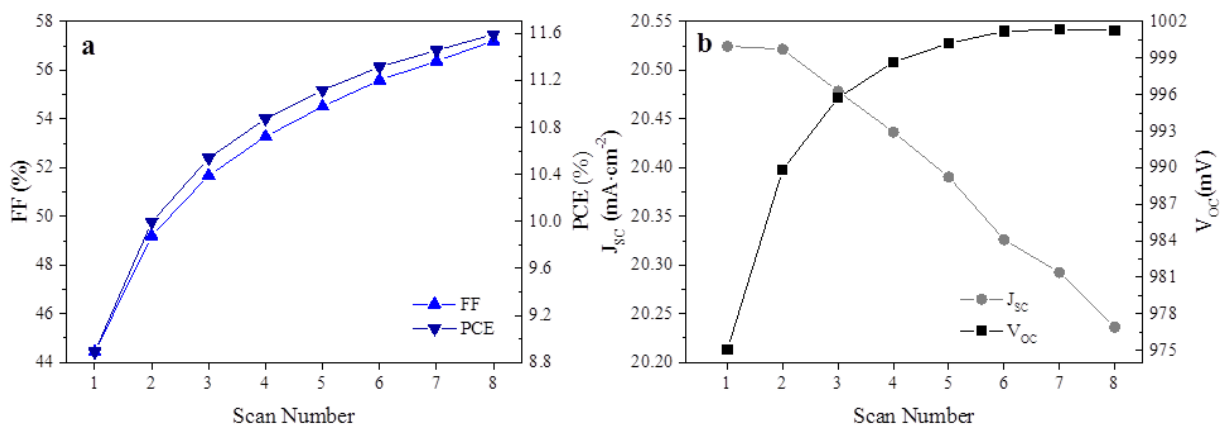


Figure 4.5 Photovoltaic parameters of Cell 2. Photovoltaic parameters extracted from the eight consecutive FR ($V_{oc} \rightarrow J_{sc}$) J - V scans for Cell 2; FF and PCE in (a) and J_{sc} and V_{oc} in (b).

4.5.1.3 Carrier Selective Contact/ $\text{CH}_3\text{NH}_3\text{PbI}_3$ Bilayers after Light-Soaking

We tested the above hypothesis by fabricating and studying the PL images of planar c- $\text{TiO}_2/\text{CH}_3\text{NH}_3\text{PbI}_3$ and $\text{CH}_3\text{NH}_3\text{PbI}_3/\text{Spiro-OMeTAD}$ structures on standard FTO glass. A pristine FTO/ $\text{CH}_3\text{NH}_3\text{PbI}_3/\text{Spiro-OMeTAD}$ structure was illuminated for 30 minutes and the spatial PL_{OC} image was collected immediately after LS (see Figure 4.6). The luminescence intensity of the AA region showed an evident increase, likely due to reduced trap density in the $\text{CH}_3\text{NH}_3\text{PbI}_3$ layer [156], enhancing the charge carrier effective lifetime. However, when measured after one day, the brightened AA region completely disappeared, which allowed us to visualize the complete reversibility of the LS effect [206] in the perovskite layer even when only in contact with Spiro-OMeTAD. As a result, structural damage at the Spiro-OMeTAD can be cautiously ruled out as the mechanism for PL quenching in Cell 2.

It is important to note that although at the excitation wavelength of 635 nm most part of the light is absorbed at the front surface and also the bulk of the perovskite layer (but not the back surface which can suppress the radiative recombination), the low PL intensity in the associated images of the FTO/ $\text{CH}_3\text{NH}_3\text{PbI}_3/\text{Spiro-OMeTAD}$ structure as compared to glass/ $\text{CH}_3\text{NH}_3\text{PbI}_3$ (see Figure 4.17) is likely due to a substantial non-radiative electron-hole recombination at the FTO/ $\text{CH}_3\text{NH}_3\text{PbI}_3$ interface in the former because of the metal-like conductive characteristics of FTO.

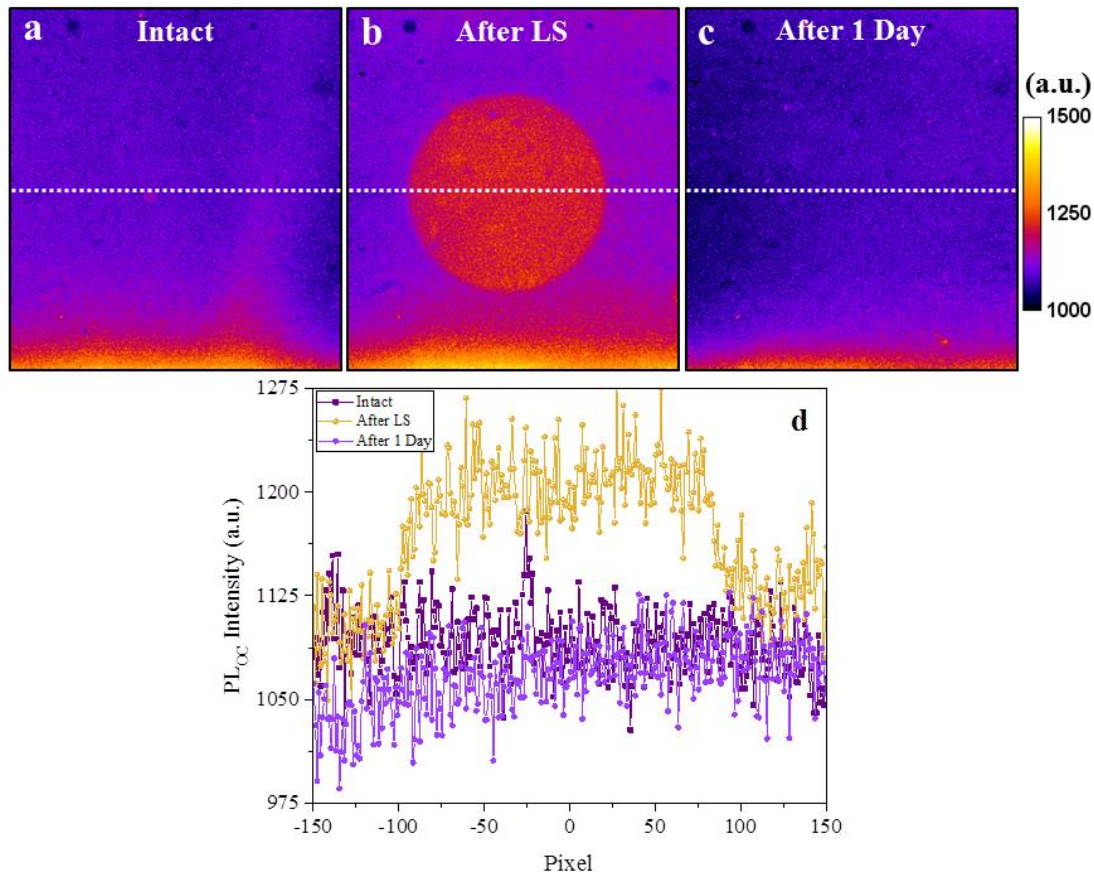


Figure 4.6 PLOCC images of FTO/CH₃NH₃PbI₃/Spiro-OMeTAD structure, excited and detected from the perovskite side, measured on the as-fabricated (a), 30 minutes light-soaked with AM1.5G illumination (100 mW·cm⁻²) (b) and after one day (c). d) Intensity profiles of the dotted line scans drawn in parts a-c.

After exposure of the FTO/c-TiO₂/CH₃NH₃PbI₃ sample to simulated solar light for 30 minutes (from the TiO₂ side), a similar PL quenching of the AA was observed (see Figure 4.7). Therefore, the observed changes in the spatial PL in Cell 2 after light-exposure (Figure 4.4f) are attributed to the c-TiO₂/CH₃NH₃PbI₃ interface. This is further elucidated by the results of FIB-TEM (the reliability of this technique for perovskites has been demonstrated in ref. [207]) and elemental analysis using energy-dispersive spectroscopy (EDS) mapping. It is noteworthy that the PL quenching in the c-TiO₂/CH₃NH₃PbI₃ structure was not found completely reversible as in CH₃NH₃PbI₃/Spiro-OMeTAD bilayer supporting the possibility of creation of relatively long-lasting defective distorted perovskite structure layers close to the c-TiO₂ interface during the prolonged illumination.

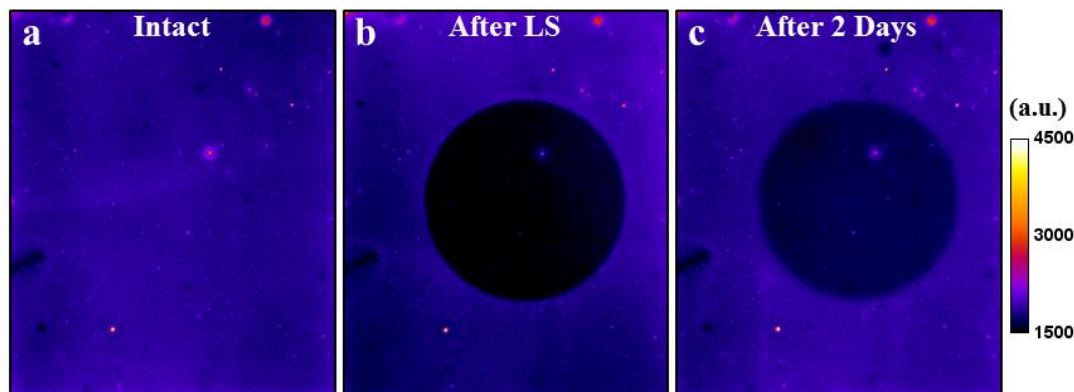


Figure 4.7 PL_{OC} images of FTO/c-TiO₂/CH₃NH₃PbI₃ structure, excited and detected from the TiO₂ side, measured on the as-fabricated (a), 30 minutes light-soaked (b) and after two days (c).

4.5.2 Long-term Impact of Light Current-Voltage Measurements

4.5.2.1 EL measurements of Cell 3

We now investigate the impact of illumination during several slow voltage sweep rate scans (30 mV s⁻¹) on the evolution of planar PSCs. Figure 4.8a shows the progress of the *J-V* curves for a new device, Cell 3. As observed for the previous two devices (Cell 1 and Cell 2) the performance increased gradually; the corresponding photovoltaic parameters are provided in Figure 4.9. The evolution of the EL^{1.2V} images from the pristine device up to 15 days after the *J-V* measurements are illustrated in Figures 4.8b to 4.8g. It can be seen that the AA experiences a dynamic intensity evolution within the time period monitored. It is noteworthy that the higher EL intensity of the illuminated region persists even after 24 hours of measurement, pointing to very long timescale of the underlying dynamics (see Figure 4.10). This could be a result of the slow scan rates used here which fall within the non-capacitive current regime with concomitant prolonged solar cell polarization [200]. The relaxation timescale observed here complies more with the lifetimes associated with vacancy- and/or interstitial-mediated ionic transport and its associated phenomena [155, 156, 204, 208-211]. This is more likely dominated by the slower moving ionic species whose migration requires larger activation energies, namely negatively charged MA⁺ vacancies (V_{MA}; and its associated positively charged interstitials; MA_i) [185,

209, 212-214] than positively charged vacancies generated by the movement of I^- (V_I ; and its associated negatively charged interstitials; I_i) [156, 209, 210]. Effects merely from interfacial electronic charge accumulation and trapping have been proposed to occur at c-TiO₂/perovskite layer [164, 197] which excluded any short- or long-range ion transport in the device.

Over the long-term, once recovered, the illuminated region suffers from an intensified EL emission deterioration. The EL intensity ratio of the AA immediately after light exposure is $R_\text{EL}=2.03$, but this degrades to $R_\text{EL}=0.65$ after 15 days. Conversely, the surrounding area which was not exposed to light and is only influenced by the cyclic voltage changes, showed an increase to $R_\text{EL}=1.38$ immediately after J - V measurement and a slower degradation to $R_\text{EL}=0.75$ after 15 days.

The time evolution of a different set of sampled regions is provided in Figure 4.11 to demonstrate the reproducibility of our results. In order to explain these results, we suggest that the dramatic improvement in EL intensity ($R=2.03$) in the illuminated region eventually leads to faster interfacial contact degradation which reduces the EL intensity ($R=0.65$). The latter would depreciate the interfacial series resistance. The latter would depreciate the interfacial series resistance and thus, reduces FF , which can explain previous observations on the suppressed FF of devices stored in dark after prolonged illumination [215].

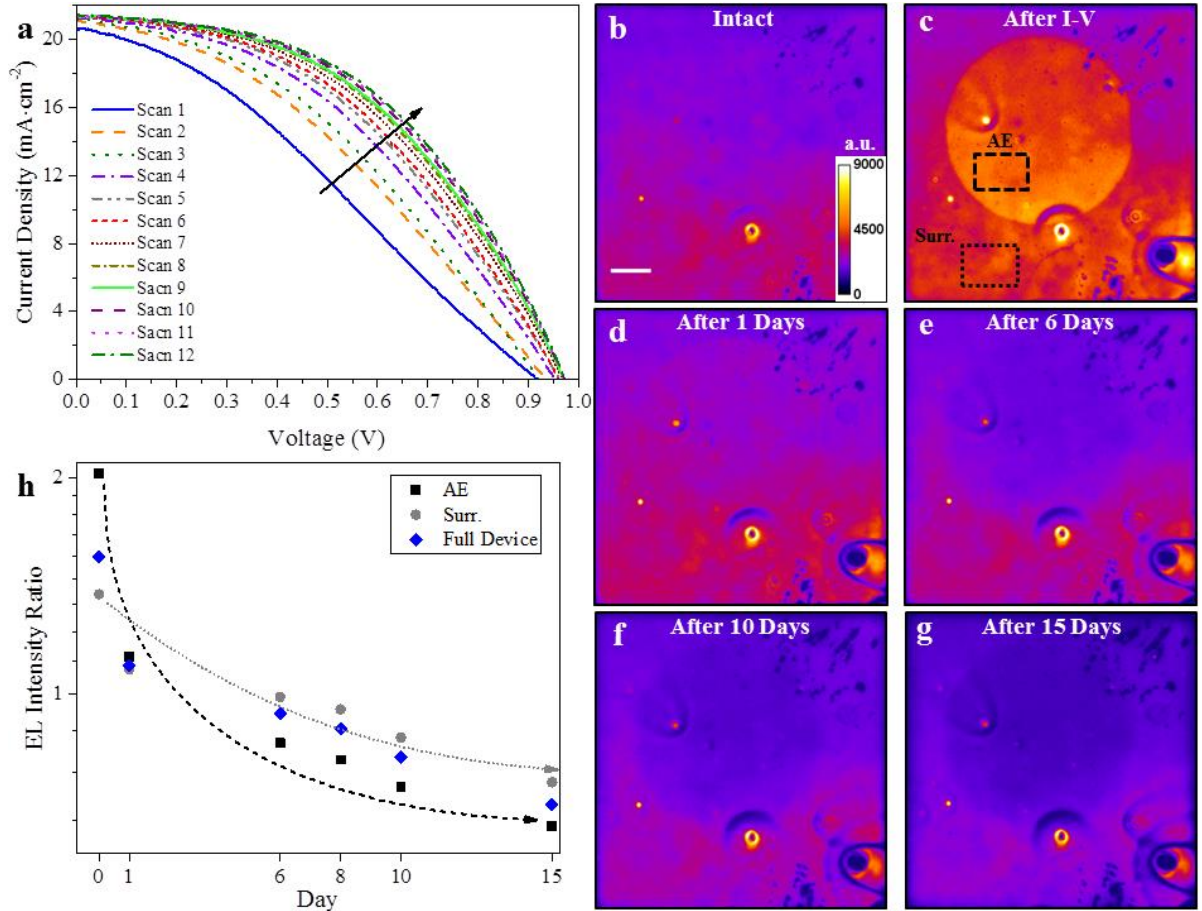


Figure 4.8 Effect of light exposure on long-term performance of the EL of PSC. a) Sequences of FR J - V scans on Cell 3 which develops dramatically after several intermittent measurements at scan rate of 30 mV s^{-1} . The evolution of $\text{EL}^{1.2\text{V}}$ images at different stages before (b) and after (c-g) J - V measurements up to 15 days stored in dark, oxygen- and moisture-free environment in between the imaging; all images have similar intensity calibration bar as in (b). The scale bar in (b) is 1 mm and applies to all the images in this figure. h) Evolution of the area-averaged EL intensity ratio of the AA (dashed-line enclosed area indicated in 4.8c) and Surr. (dotted-line enclosed area indicated in 4.8c) regions and the entire device. Day “0” indicates the intensity ratio right after illumination. The arrows are guides to the eye for the changes measured in area-averaged EL intensity ratio over time.

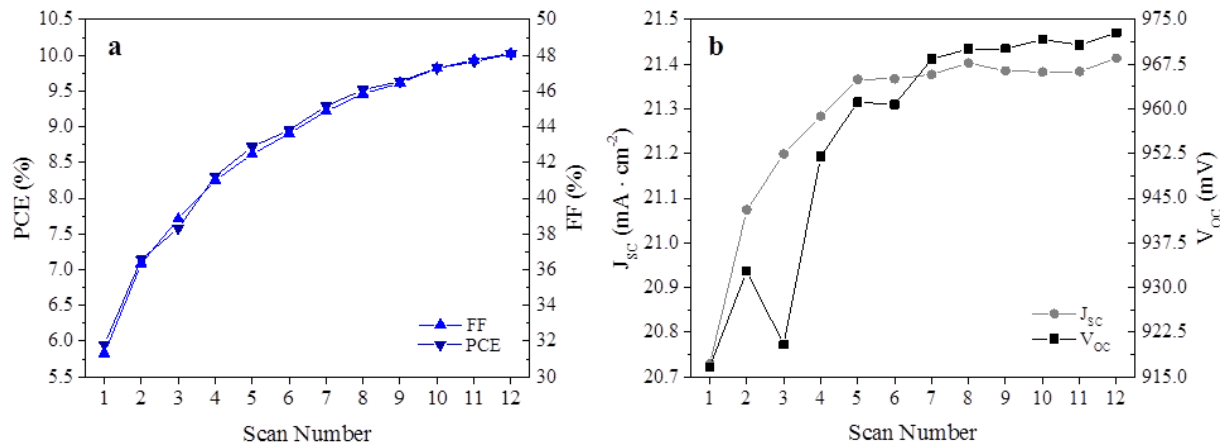


Figure 4.9 Photovoltaic parameters of Cell 3. Photovoltaic parameters extracted from twelve consecutive FR ($V_{OC} \rightarrow J_{SC}$) J - V scans on Cell 3; FF and PCE in (a) and J_{SC} and V_{OC} in (b).

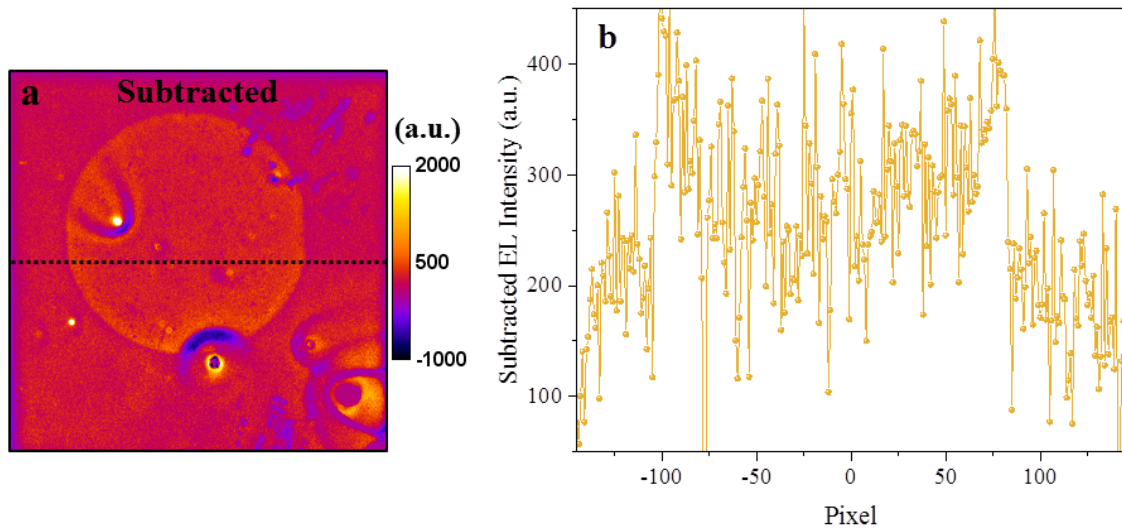


Figure 4.10 a) EL image obtained by subtracting the as-fabricated Cell 3 image from the image collected after one day storage in the dark and oxygen- and moisture-free environment. b) EL intensity profile of the dotted line scan shown in Figure 4.10a;

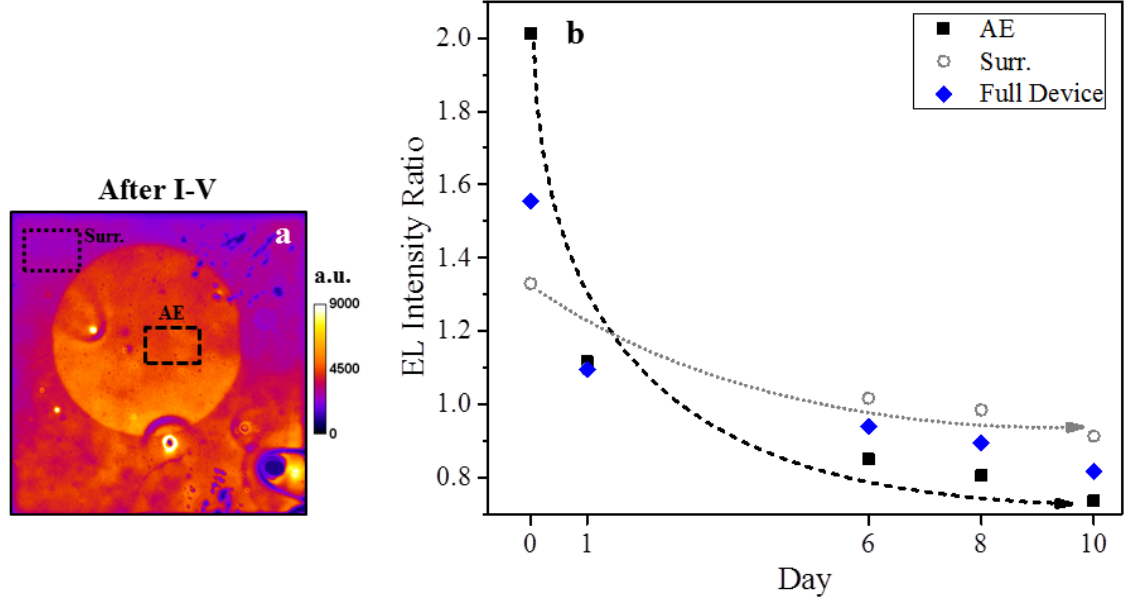


Figure 4.11 a) The $\text{EL}^{1.2\text{V}}$ image of Cell 3 taken right after the consecutive $J-V$ measurements. b) Evolution of the area-averaged EL intensity ratio (R_{EL}) of different regions; the AA (dashed-line enclosed area in 4.11a) and Surr. (dotted-line enclosed area in 4.11a) regions and the entire device.

Effective charge carrier recombination in the $\text{CH}_3\text{NH}_3\text{PbI}_3$ layer and its associated interfaces in the same device (Cell 3) was examined by imaging its PL intensity. The $\text{EL}^{1.2\text{V}}$ and PL_{OC} images of the device aged for 17 days in an oxygen- and moisture-free (<1 ppm), dark environment, are provided in Figures 4.12a and 4.12b, respectively. An inverse correlation between EL and PL intensity spatial profiles is found, exemplified by the intensity profile of the line scan shown in Figure 4.12c, which resembles the reverse behaviour observed in the images collected immediately after $J-V$ measurement (see description of Figure 4.3). We tentatively attribute this to the electrical/physical interfacial decoupling occurring at the c-TiO_2 and $\text{CH}_3\text{NH}_3\text{PbI}_3$ interface over time; further evidence for this proposal will be discussed in the following sections. In Figures 4.12a and 4.12b, this proposed decoupling has respectively led to increased interfacial series resistance, suppressing EL intensity, and improved charge carrier effective lifetime, increasing PL intensity.

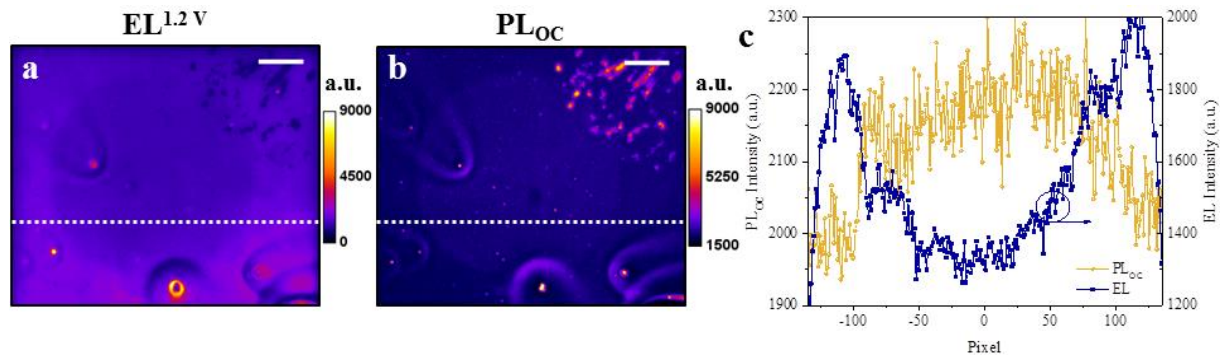


Figure 4.12 Comparison of EL and PL_{OC} response of the aged PSC upon illumination. a) EL^{1.2V} image of Cell 3 and its corresponding PL_{OC} image after 17 days in dark, oxygen- and moisture-free (< 1 ppm) environment (b); The scale bars are 1 mm. c) Luminescence intensity profiles of the dotted line scans presented in images (a) and (b) which clearly shows the inverse intensities of EL and PL_{OC} images.

4.5.2.2 PL measurements of Cell 2

PL_{OC} images of Cell 2 recorded immediately after *J-V* measurements and after six days are illustrated in Figures 4.13a and 4.13b, respectively. Intriguingly, upon leaving the device in the dark, the PL intensity ratio observed immediately after the *J-V* scans in the AA ($R_{\text{PLOC}}=0.93$), which is lower than the ratio of the rest of the device ($R_{\text{PLOC}}=1.01$) implying reduced carrier effective lifetime, was reversed and, as time evolves, increases in relative intensity ($R_{\text{PLOC}}=0.95$ compared to $R_{\text{PLOC}}=0.89$ of the surrounding area). This behaviour was sustained for more than six weeks (see Figure 4.14 for the complete set of data). This spatial PL intensity contrast between AA and the surrounding non-illuminated regions of the aged device is consistent with the results of the previous section where the device was only used for monitoring the EL evolution (Figure 4.12b).

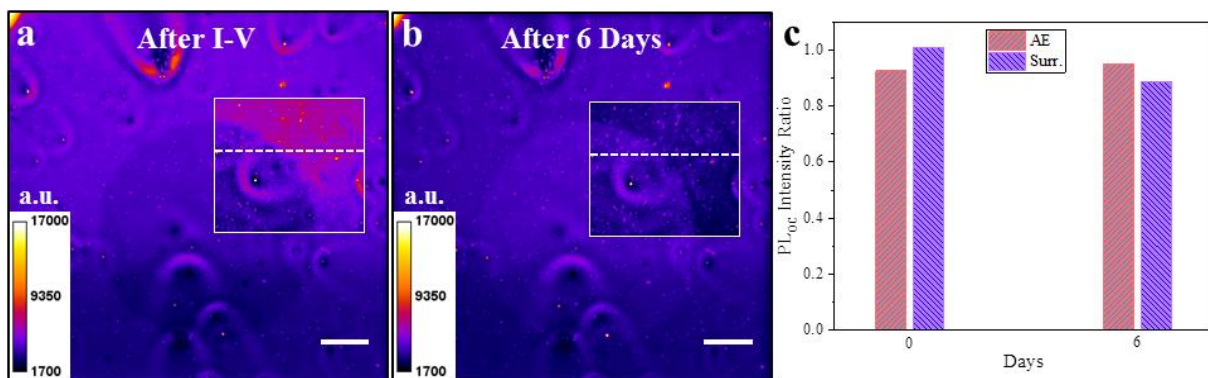
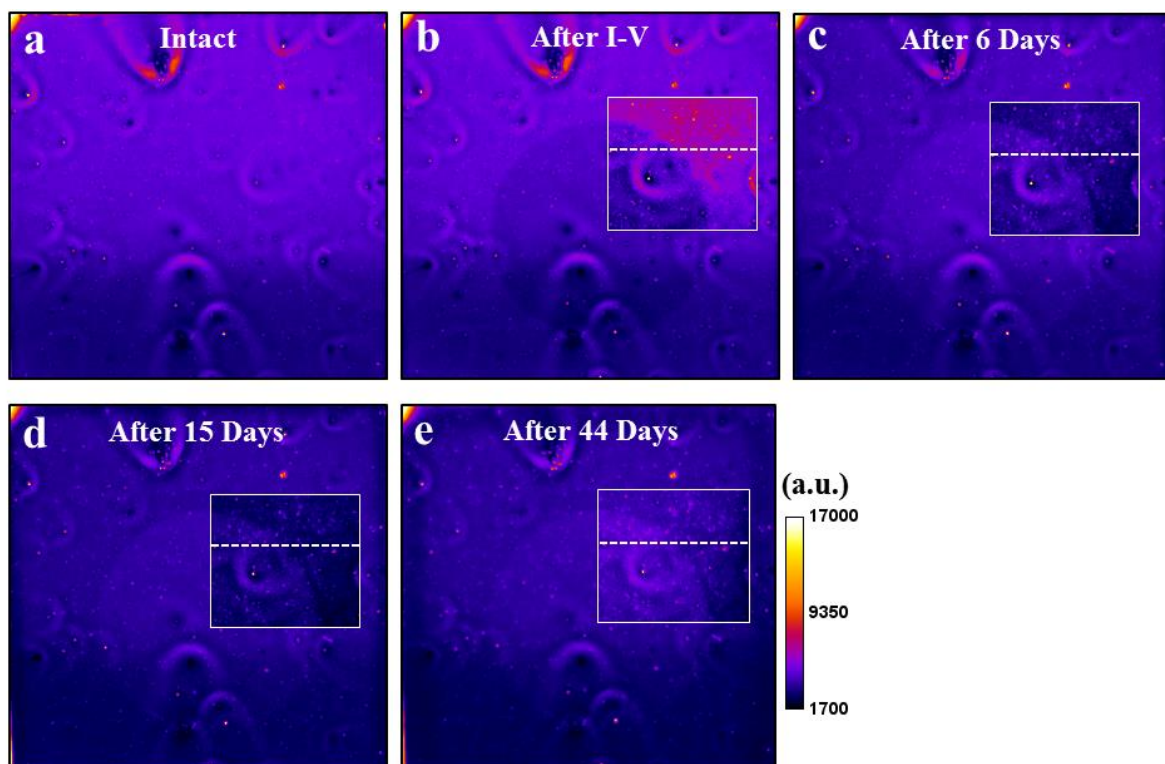


Figure 4.13 Effect of light exposure on long-term performance of the PLOC of PSC. Spatially-resolved PLOC images of Cell 2 measured immediately after J - V scans (a) and one collected after six days storage in dark nitrogen-environment condition (b). Both images have identical intensity scale. The sections of the images, which include the dashed line scans, are presented in different intensity than the main device images providing appropriate contrast between AA and Surr. regions. The scale bars are 1 mm. c) Area-averaged PLOC intensity ratio (R_{PLOC}) of the AA (right-hand hatched column) and Surr. (left-hand hatched column) regions on the line scans drawn on the selected areas of the images in (a) and (b).



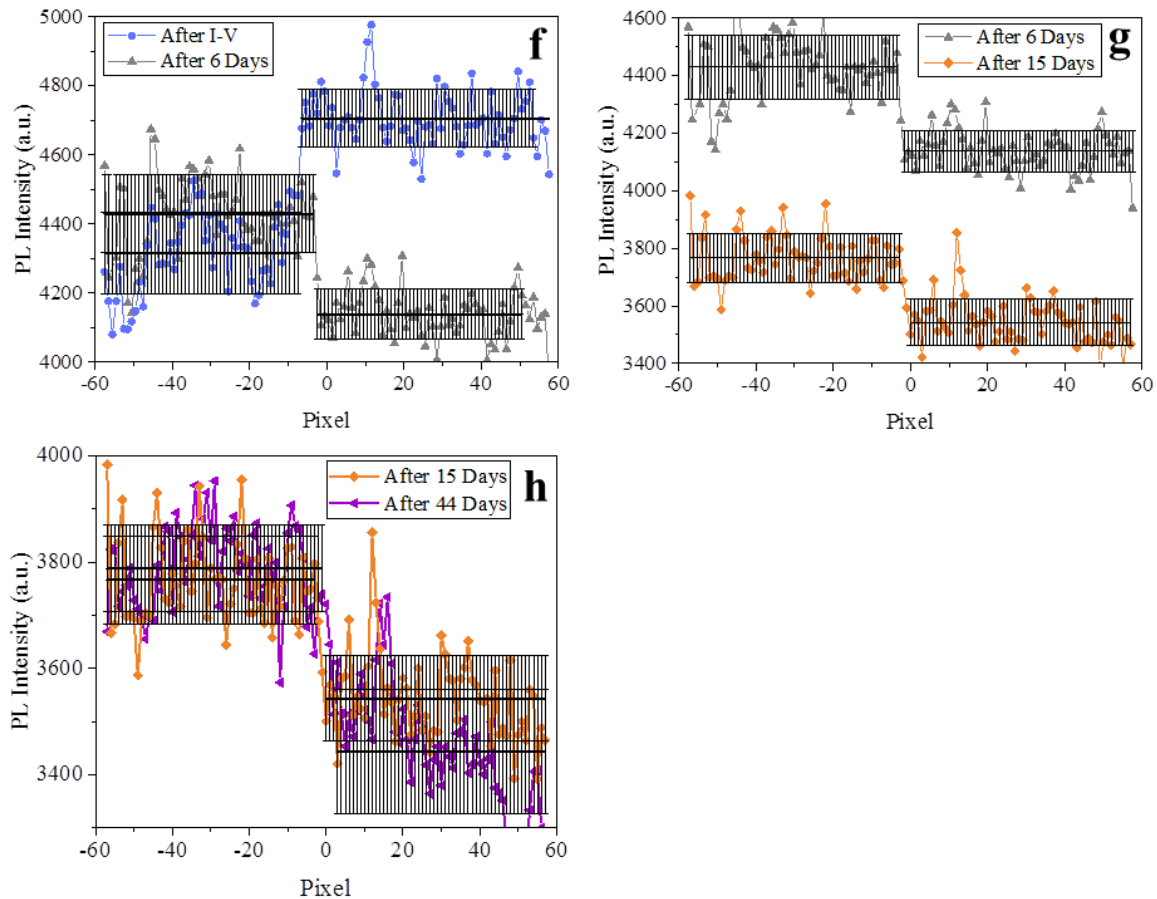


Figure 4.14 Time evolution of PL_{OC} images of Cell 2. a-e) illustrate the PL_{OC} images measured for Cell 2 over 44 days. f-h) show the corresponding intensity profiles of the line scans drawn in a-e images for the selected areas encompassing both high-exposed regions and its surrounding. The black solid lines and the error bars in (f-h) present the mean and standard deviation of the data points in the AAs and the surrounding regions of the line scans.

4.5.3 Impact of Light-Soaking at Open-circuit Condition

Finally, a pristine device after 30 minutes of LS was tested in order to disentangle the effect of electrical bias in $J-V$ measurement from the light-induced effects. The $EL^{1.2V}$ images of Cell 4 in a pristine state and immediately after LS are shown in Figures 4.15a and 4.15b, respectively. Interestingly, the EL intensity of the AA decreases significantly after one day of storage in a dark nitrogen-environment. Two rationalizations for the latter observation are: (i) the perovskite layer is fully damaged upon prolonged 1-sun AM1.5G simulated solar illumination; or (ii) there is a substantial degradation of the perovskite interface with the selective contact, dramatically

increasing the series resistance (see Figure 4.15c). Explanation (i), however, would be in contrary to the enhanced EL intensity realized immediately after LS (Figure 4.15b). To clearly differentiate between these two possibilities, the PL_{OC} image of the one-day old device was measured (see Figure 4.15d). The histogram presenting the distribution of the occurrence frequencies of the spatial EL and PL intensities in Figures 4.15c and 4.15d are given in Figure 4.16. Two distinct luminescence intensity regions are obvious from the associated PL_{OC} image (Figure 4.15d). The clear inverse response of spatially-resolved EL and PL_{OC} images after one day of storage allows us to rule out (i). That is, the light-exposed region has a severely deteriorated interface (higher PL intensity in Figure 4.15d) when compared to the surrounding area where physical/electrical contact was maintained (suppressed PL intensity in Figure 4.15d). This is consistent with PL quenching which occurs in the neat CH₃NH₃PbI₃ film when forming a flat junction with c-TiO₂ (see Figure 4.17), due to the presence of greater interfacial defects (e.g. ionic vacancies [209]) and thus, enhanced non-radiative recombination at the c-TiO₂/CH₃NH₃PbI₃ interface. We excluded any major irreversible changes of the perovskite layer (decomposition), possibly induced by the combination of light and moisture [197] during *J-V* measurements or LS in ambient condition or during device storage in dark nitrogen-environment in the glovebox, as origin for the observed EL and PL changes. X-ray diffraction (XRD) data of a 30 minutes light-soaked device measured after 50 days from light-exposure did not show any diffraction pattern of PbI₂, which would be the typical degradation product of CH₃NH₃PbI₃, and is consistent with a fresh non light-soaked device (see Figure 4.18 for the XRD results).

Our assertion that physical detachment occurs at the c-TiO₂/CH₃NH₃PbI₃ interface rather than the CH₃NH₃PbI₃/Spiro-OMeTAD interface was supported by an observation made during FIB-TEM sample preparation for TEM imaging of Cell 4. During the lift-out of a FIB-TEM cross-section of the 30 minutes light-soaked planar structure PSC (Cell 4) the layers separated close to the c-TiO₂/CH₃NH₃PbI₃ interface whereas the CH₃NH₃PbI₃/Spiro-OMeTAD connection remained intact (see Figure 4.19 for the cross-sectional TEM image).

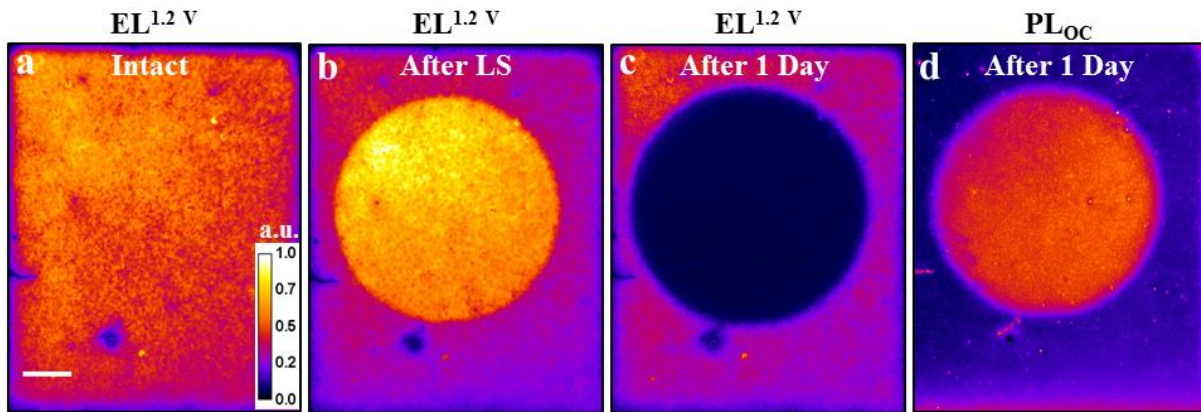


Figure 4.15 Effect of light-soaking under open-circuit conditions on EL and PL_{OC} behaviour of PSC. Luminescence images illustrating the impact of 30 minutes light-soaking, at 1-sun simulated solar irradiance, on the EL performance of Cell 4 at 1.2 V forward bias for fresh (a), immediately after $J-V$ (b) and after one day (c); the PL_{OC} image of the same device after one day storage in dark is presented in (d). The scale bar in (a) is 1 mm and applies to all the images in this figure. Luminescence intensity of all the images in (a-d) is in normalized form.

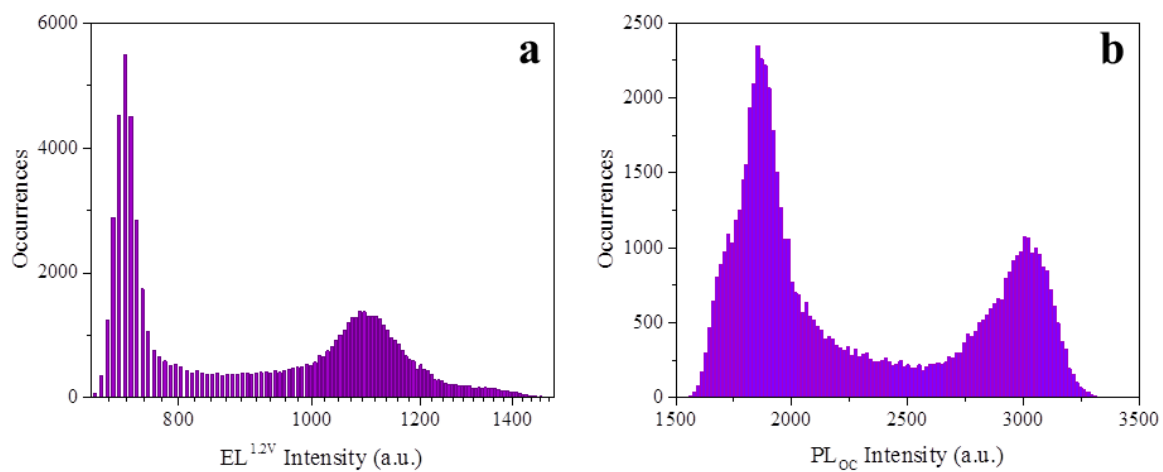


Figure 4.16 Intensity distributions of EL and PL images of Cell 4. Histograms showing the occurrence frequency of the intensity distribution of the spatially-resolved $EL^{1.2V}$ and PL_{OC} images presented in Figures 4.15c and 4.15d of the main text. Occurrences, as the y-axis, represent the number of pixels associated with a specific intensity bin.

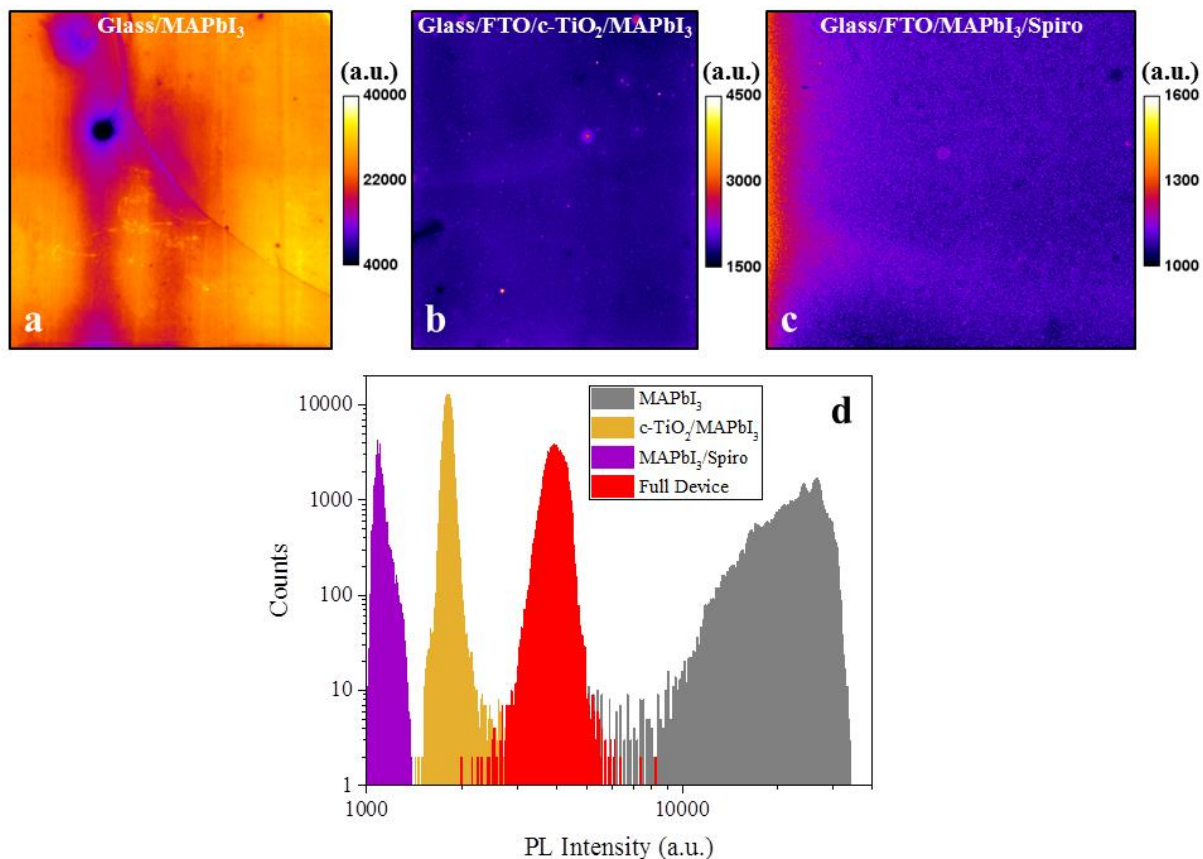


Figure 4.17 PL images and intensity distribution histograms of perovskite incorporated into various structures. PL_{OC} images of $\text{CH}_3\text{NH}_3\text{PbI}_3$ layer deposited on different substrates forming a flat junction; glass/ $\text{CH}_3\text{NH}_3\text{PbI}_3$ (a), glass/FTO/c-TiO₂/ $\text{CH}_3\text{NH}_3\text{PbI}_3$ (b), and glass/FTO/ $\text{CH}_3\text{NH}_3\text{PbI}_3$ /Spiro-OMeTAD (c). Histogram showing the occurrence frequency of the intensity distribution of the spatially-resolved PL_{OC} images of the structures presented in (a-c) in addition to a completed device. All the samples have been excited from the glass side with an LED with central wavelength of 635 nm at 1 mW cm^{-2} excitation intensity.

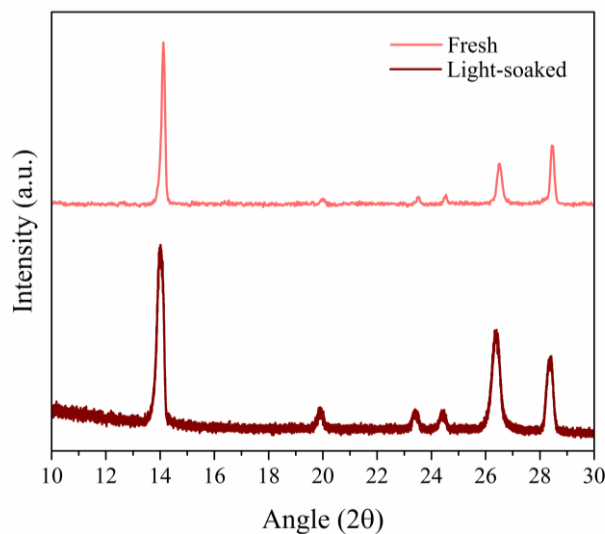


Figure 4.18 XRD pattern of an aged light-soaked and fresh non light-soaked device. XRD pattern measured on an encapsulated 50 days aged device which was light-soaked at open-circuit condition for 30 minutes in ambient condition. No signature from the residual PbI_2 left during fabrication procedure or moisture-induced degradation formed PbI_2 was detected at 12.5 degree which is comparable to a fresh device without any light-soaking.

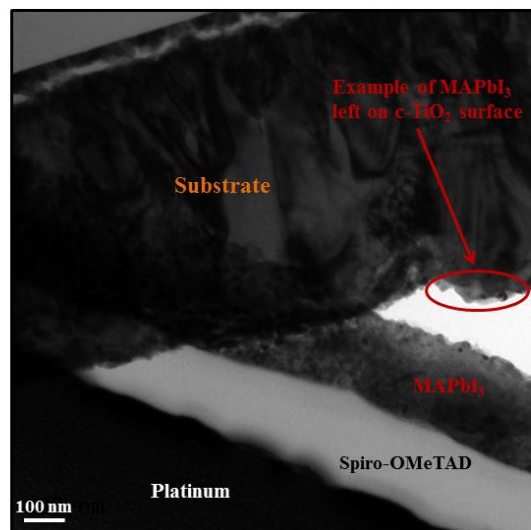
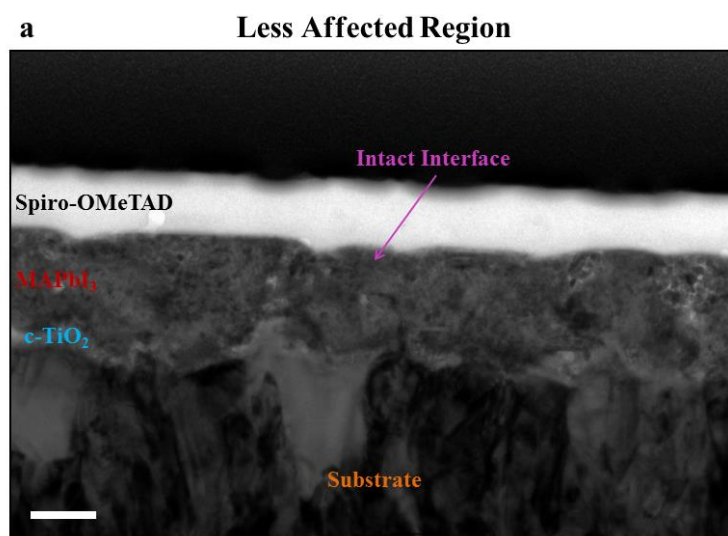


Figure 4.19 High-resolution cross-sectional TEM images of the changes in the light-exposed regions of Cell 4. Cross-sectional TEM image of Cell 4 after being light soaked for 30 minutes under simulated AM1.5G illumination of $100 \text{ mW} \cdot \text{cm}^{-2}$ irradiance. The separation at $\text{c-TiO}_2/\text{CH}_3\text{NH}_3\text{PbI}_3$ interface occurred during FIB lift-out preparation step due to the already weakened interface while the $\text{CH}_3\text{NH}_3\text{PbI}_3/\text{Spiro-OMeTAD}$ interface remained intact.

4.5.4 Cross-sectional TEM and EDS

In order to investigate any induced chemical and structural changes in the device in the light-exposed region, in particular at the interfaces, cross-sectional TEM measurements were performed at the central AA region of Cell 3 (cf. Figure 4.8) and are shown in Figure 4.20. The TEM images of two distinctly affected regions, mildly and severely influenced regions, are presented in Figures 4.20a and 4.20b, respectively. The corresponding elemental analysis EDS maps of similarly influenced regions are provided in Figure 4.21. Importantly, the CH₃NH₃PbI₃/Spiro-OMeTAD interface remained virtually intact in both images and no change in the perovskite layer thickness can be detected from the TEM images. A clear interfacial detachment, close to the ETL interface, is evident in Figure 4.20b. This interfacial delamination matches well with the above mentioned tentative interpretation of the EL and PL reciprocal intensity relationship in the aged devices. Noticeably, some of the perovskite layer has been left on TiO₂ in the detached region. While lead, iodine, carbon and nitrogen are uniformly distributed within the perovskite layer in the less influenced section (Figure 4.21 panel a), an elemental gap is observed in the TEM image of the severely affected region (Figure 4.21 panel b). The main elements with partial residues left on the TiO₂ surface at the detached interface are Pb and I (see Figure 4.20b). This correlates with the EDS line scans collected from the less- and severely-affected regions provided in Figure 4.22.



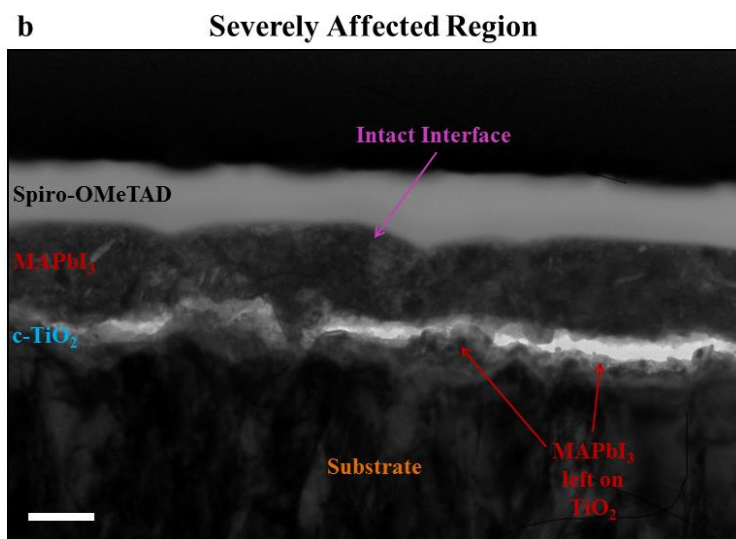
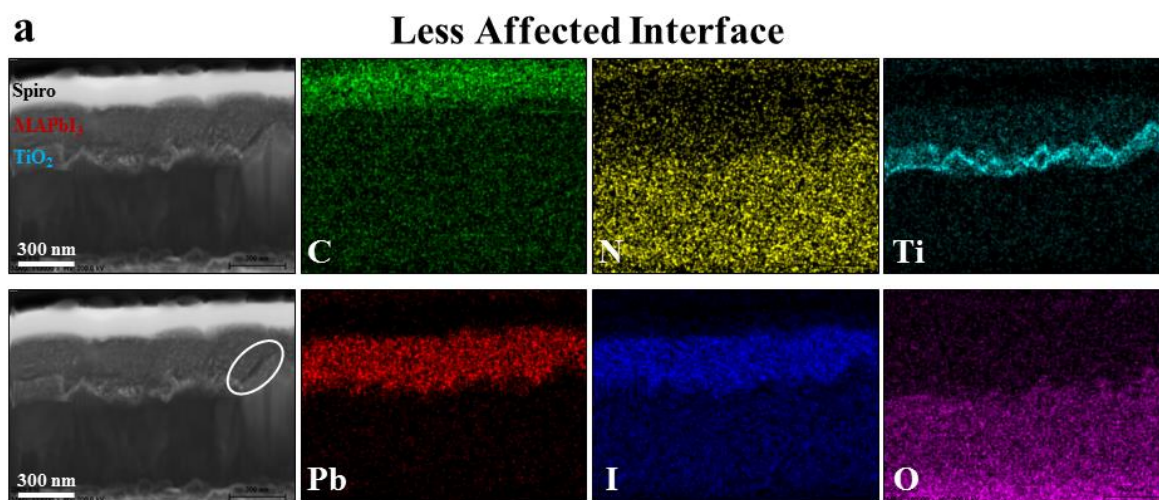


Figure 4.20 High-resolution cross-sectional TEM images of the changes in the light-exposed regions of Cell 3. a) Shows an interface which is affected less during light-exposure and b) a region severely affected and delaminated upon illumination. The overall exposure to the full spectrum light of the solar simulator is about 10 min. The scale bars are 200 nm.



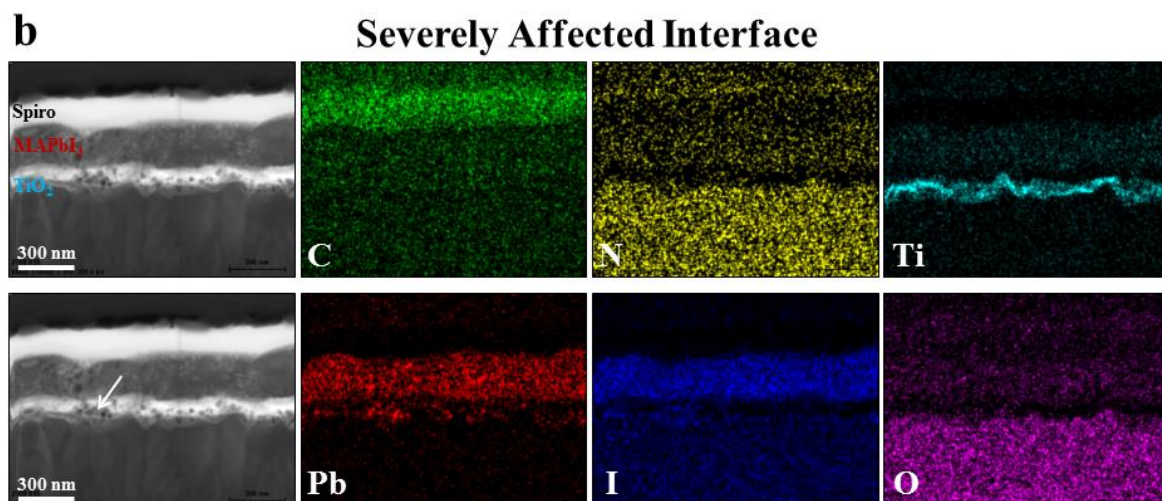
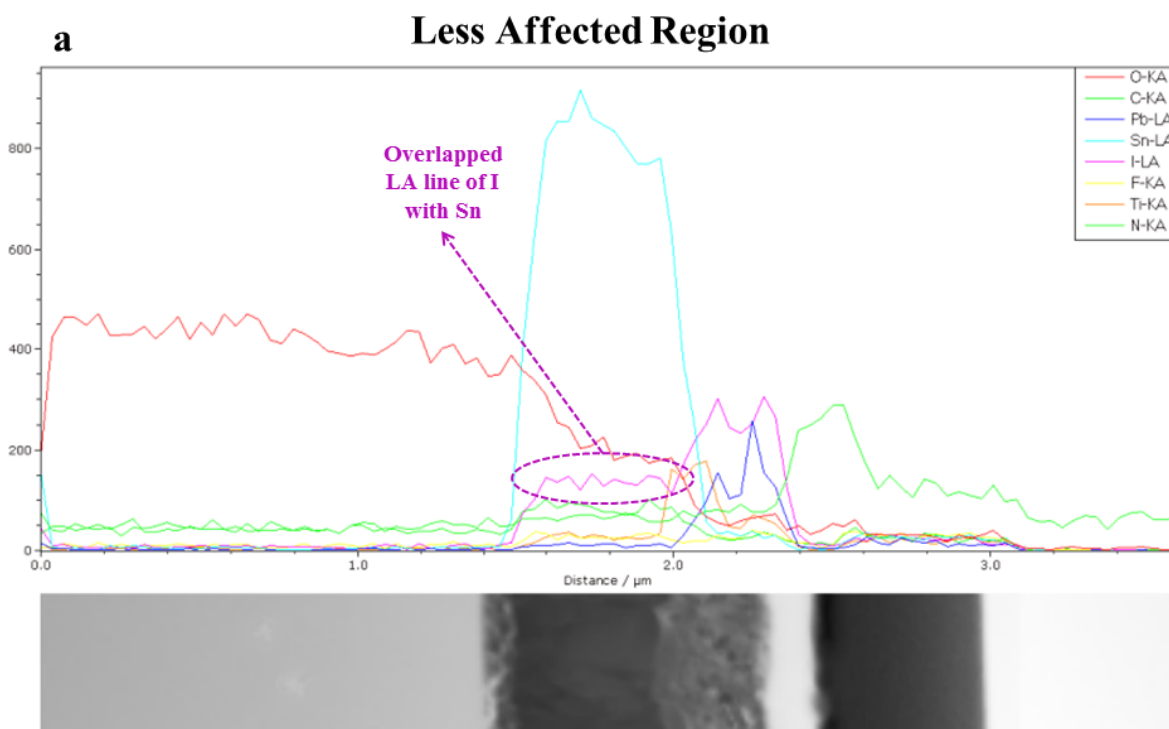


Figure 4.21 Cross-sectional EDS maps. Cross-sectional TEM images (far left columns) and EDS elemental maps of two entirely different interfaces; less affected (panel a) and severely influenced (i.e. delaminated) by the external field (panel b) collected from Cell 3. The unexpected detection of iodine within the substrate region is considered as artefact possibly due to the close *L*-series with Sn (tin). For closer look at the elemental signals check EDS line scans in Figure 4.22. The white oval in panel (a) indicates a small region of the interface supposedly suffering from detachment. The arrow in panel (b) points at a clear fraction of $\text{CH}_3\text{NH}_3\text{PbI}_3$ remained on the c- TiO_2 surface.



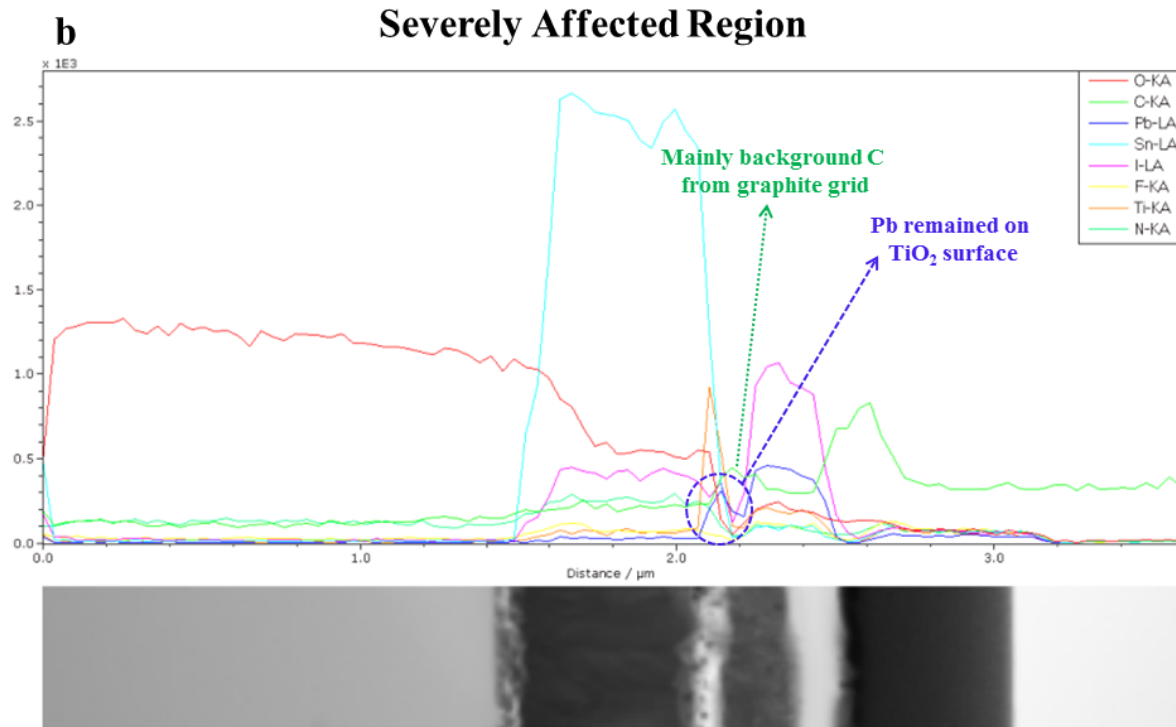


Figure 4.22 EDS line scans. EDS line scans of a region less affected (a) and severely affected (b) by light exposure during the J - V characterization of Cell 3.

4.6 Mechanistic Interpretation

The dynamic evolution of the relative changes in the luminescence intensity of the illuminated region with respect to its intact state (i.e. prior to light-exposure) or relatedly with respect to its surrounding area (which is only affected by the cyclic voltage changes during J - V measurement) for the PL_{OC} , EL and PL_{SC} intensity images right after the illumination and upon storage in dark (oxygen- and moisture-free atmosphere) for several days is graphically summarized in Figure 4.23a. In the following, the speculated mechanism underlying the evidenced dynamics is elaborated.

4.6.1 Perovskite Degradation Assessment

The stability of c-TiO₂ based planar PSCs, under prolonged continuous monochromatic UV-light (365 nm) irradiation, was recently investigated by Li *et al.* [216]. Decomposition of the perovskite layer into PbI₂ was observed at the interface between the CH₃NH₃PbI_{3-x}Cl_x and the n-

type ETL. As stated by the authors, however, harsh conditions had been applied in that study. The light intensity used was about 110 suns equivalent with respect to the intensity of the <400 nm spectra of the simulated solar irradiance and the potential impact of moisture and oxygen [175, 197] on the light-induced degradation was not disentangled in the non-encapsulated solar cells. Moreover, a statistically significant device performance degradation could not be detected within the first 5 minutes of the high intensity UV-light exposure, a time period similar to the intermittent sequential *J-V* measurements conducted in this study (under AM1.5G simulated solar irradiance). For these reasons interfacial PbI₂ formation, mediated by the photocatalytic effect of TiO₂ under UV-light, might not be relevant to the results presented here.

The enhancement in the EL intensity of the illuminated region was shown to be remarkable and to recover completely only several hours after the light exposure. Besides, the nature of the decomposition reaction of CH₃NH₃PbI₃ into $\Gamma^- + \text{PbI}_2 + \text{MA}^+$ was recently shown to be endothermic, being inefficient at room temperature [217]. By measuring the *J-V* of Cell 2 after 45 days it was realized that V_{OC} , which reflects the CH₃NH₃PbI₃ bulk condition, remained unchanged over this time whereas the *FF* reduced dramatically with an expected consequential decrease in J_{SC} (see Figure 4.24; note that the aperture was located almost at the same position for *J-V* measurement on both the fresh and aged device; compare Figure 4.4c and Figure 4.24d). Moreover, it seems contradictory to consider the partial decomposition of MAPbI₃ to PbI₂ during illumination as the origin of delamination at the c-TiO₂/CH₃NH₃PbI₃ interface while PL in the AA shows higher intensities than the regions where the interface is less influenced upon resting the device (e.g. see Figure 4.15d). These, however, together with other experimental evidences provided by the XRD, TEM and EDS results make the detrimental effect of bulk perovskite degradation/decomposition less likely as a key underlying mechanism of intrinsic device performance degradation upon very first light-exposure or relatedly *J-V* characterization.

4.6.2 Ionic Species Involved

The relatively long timescales (at least 10 minutes) associated with the above presented PL and EL observations allows us to link these transient behaviours with ion migration commonly used to interpret the hysteretic effect in PSCs [155, 204, 208, 211]. It has been reported that the activation energies associated with the iodine vacancies (V_I) and interstitials (I_i), which fall within 0.1-0.2 eV range are too small to be able to merely explain the photocurrent transient behaviour and J - V hysteresis in PSCs and therefore, the migration of methylammonium vacancies (V_{MA}) was also highlighted [209]. Richardson *et al.* recently argued that these low energies and their corresponding high diffusion coefficients enable fast iodine defect movement which can negate the device's internal E-field prior to any MA^+ associated transport [204]. Thus it was concluded that, if iodine related defects contribute to the PSC hysteresis, activation energies in excess of 0.1-0.2 eV might be more relevant for V_I migration (these activation energies include the breaking of the Pb-I bonds). However, recent experiments [156] and theoretical calculations [210] have shown that the low activation energies of I^- associated transport is plausible. In fact, the activation energies of about 0.5-0.6 eV associated with V_I in ref. [155] employed for device modelling in ref. [204] is indeed in the range of V_{MA} related values [209] and suggest that V_{MA} migration also contributes to the hysteresis commonly observed in PSCs [185]. Due to the very large activation energies associated with migration of the lead (Pb) vacancies (≥ 1 eV) [155, 209] in the following V_{Pb} is excluded from contributing to triggering the structural distortion and possible $CH_3NH_3PbI_3$ break-down. The latter phenomena are attributed to the combined movement of mainly V_{MA} [185, 209, 213, 218] and/or its associated MA^+ interstitials (MA_i) [184, 185] and V_I and its correlated I_i [156, 184, 219]. These ionic motions occur more readily at the grain boundaries, as recently demonstrated by our group [213] and Huang and co-workers [218]. As such, by performing slow scan rate J - V measurements, we expect both anionic and cationic species to have sufficient time to diffuse through in the active layer and, in particular, near the selective contacts. Employing DFT calculations, Azpiroz *et al.* proposed that V_{MA} and/or I_i may be dominantly located at the TiO_2

interface under equilibrium conditions, while the positively charged ionic defects would be more uniformly dispersed throughout the perovskite film [209]. The accumulation of the relevant ionic defects at the TiO₂ interface [203, 209] upon perovskite film deposition can induce inherent deformation and rearrangement of the soft structure of the perovskite layer even prior to light exposure.

4.6.3 Mechanism Description

Assuming that the mobile charged ionic species are absent, at equilibrium condition, the free charge carriers in the active layer of a PSC would distribute at their corresponding interfaces (electrons (holes) concentrate at the c-TiO₂ (Spiro-OMeTAD)) upon formation of the contacts. The field in a fresh device in dark is highest at the interfaces and its integration over the Debye length (decay length associated with the surface E-field close to the contacts) gives its contribution to the electrostatic potential. However, being aware of the possible ionic defect movement in the organic-inorganic lead halide perovskites as reported in several studies [156, 220-224], and in particular in the CH₃NH₃PbI₃ composition, the built-in E-field (E_{bi} ; this is generally formed due to the difference in the work functions of ETL and HTL [225]) in a CH₃NH₃PbI₃-based PSC at equilibrium condition when stored in the dark would induce the transport of these ions toward the interfaces. The negatively-charged (V_{MA} and/or I_i) and positively-charged (MA_i and/or V_I) ions move towards the surface regions and accumulate within the perovskite lattice in the narrow Debye layer near the ETL and HTL surfaces, respectively. The field created by the ions would then oppose the E_{bi} , partially reducing the effective built-in potential across the device [204, 222]. While this ion movement occurs, ideally the overall concentration of the free electrons and holes concentration at the surfaces remains unchanged in the dark and thus, leading to narrowing of the Debye layers. Consequently, the interfacial band-bending strengthens [226, 227] and the middle part of the device becomes almost field free [223, 228] (see the energy band diagram in Figure 4.23b). It is worth mentioning that it has been recently shown that the ionic accumulation at the interfaces

has a greater impact on the hysteresis than capacitive current especially at low scan rate measurements [223].

Immediately after illumination, the E-field in the centre of the device would have negative slope [228] because of insufficient time for the ions to move away from the contacts so as to relieve the strong surface field contributions (see Figure 4.23c). As the device is illuminated for longer time, the photo-voltage induced by the photo-generated free charge carriers opposes the polarization induced by ion concentration at the contacts. This will force the ions to diffuse away from the interfacial regions during the prolonged illumination which will mitigate the strength of the interfacial band-bending (see Figure 4.23d), reducing the surface E-field and therefore, influencing the Debye layers width especially at the TiO_2 interface [204]. It is also recently shown that light itself might have an impact on reducing the ionic transport activation energy in perovskites [208, 214] which probably allows more ions to move in the illuminated region than the surrounding masked area influenced only by external bias during J - V scans. Sweeping the voltage bias, from high to low, at scan rates comparable to the ionic response times in the order of hundreds of seconds would assist the dispersion of the ions away from the surface regions in favour of the illumination effect; the latter induces an electric field through the created photo-voltage which moves the ionic defects away from the perovskite/contact interfaces towards the bulk of the active layer. Right after the light is switched off, the electron concentration at the surface region is expected to be similar to the initial dark condition of the fresh device; however, importantly the lower field at the contact region and hence, the number of appropriate carriers in the vicinity of the contact, is likely to reduce the contact resistance resulting in the observed EL enhancement. Considering a larger concentration of ionic vacancies and also interstitials [209] and a greater potential variation at the $\text{c-TiO}_2/\text{CH}_3\text{NH}_3\text{PbI}_3$ interface [204], it can be speculated that under illumination the bond breakage and structural collapse due to ion transport (see Figures 4.23e and 4.23f) – particularly the large MA^+ cation associated vacancies – is accelerated near the $\text{c-TiO}_2/\text{CH}_3\text{NH}_3\text{PbI}_3$ interface compared to the $\text{CH}_3\text{NH}_3\text{PbI}_3/\text{Spiro-OMeTAD}$ interface.

We speculate that, after the removal of the photo- and/or electro-induced E-field, over the long term in the dark, the device attempts to retrieve its equilibrium condition through the slow redistribution of the ionic species, to their pseudo-equilibrium initial positions within the perovskite structure. This is consequent to a precedent structural changes during illumination, which might have already damaged the soft structure of CH₃NH₃PbI₃ [184, 205] (Figure 4.23e), resulting in a gradual electrical decoupling and in some instances leading to severe physical decoupling of the perovskite and the TiO₂ layer. This would consequently suppress EL signal. The proposed mechanism here complies well with a recent study on CH₃NH₃PbI₃ nanowires in which ion migration, particularly MA⁺, was shown to induce structural distortion through a structural swell-shrink mechanism [185] with the possible consequence of accelerated aging of the perovskite film. It is noteworthy that there is some residual CH₃NH₃PbI₃ left on the TiO₂ layer clearly shown in Figures 4.19 and 4.20. Therefore, this structural weakening which could facilitate the structural detachment at the c-TiO₂/CH₃NH₃PbI₃ interface – during FIB-TEM sample preparation – does not necessarily occur precisely at the c-TiO₂/CH₃NH₃PbI₃ interface, but very close to it. No obvious reduction in the thickness of the CH₃NH₃PbI₃ active layer could be detected in the TEM images in Figure 4.20, even in the severely delaminated interface. This is, consistent with the very thin Debye layer within which diffusion of large concentration of ions occurs [204, 209, 211] due to the internal E-field variation across the device. The origin of delamination is proposed to be near or this thin Debye region. Finally, the severity of this interfacial delamination can largely vary across the TiO₂/perovskite interface in the illuminated region. This is due to the inhomogeneous ionic defect density distribution among the grains of a polycrystalline thin film as well as grain size variation within a thin film [51, 156], both of which having an impact on the local concentration of mobile ions near the interfaces.

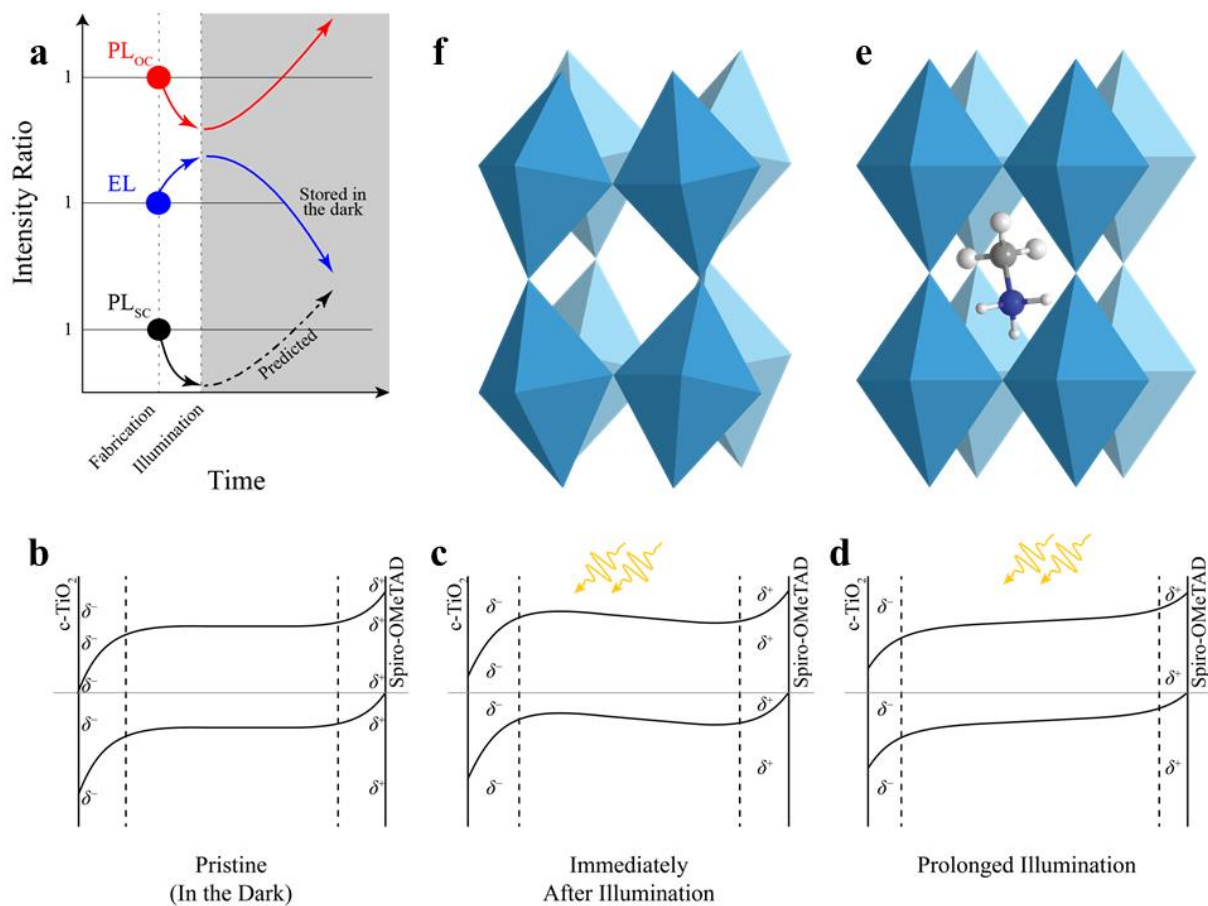


Figure 4.23 Graphical description of the EL, PL_{OC} and PL_{SC} evolution of the light-exposed region and the associated modifications to the perovskite layer energy band alignment and its three-dimensional structure. a) The diagram shows the dynamic evolution of the ratio of the luminescence intensity of the illuminated region with respect to its fresh state in planar PSCs for PL_{OC} , EL and PL_{SC} images upon its first exposure. Panels (b), (c) and (d) show the energy band diagram of the device in its pristine state in dark, immediately after exposure to light or under working conditions (bias voltage $< V_{OC}$) and when the device is under prolonged illumination at open-circuit condition, respectively. Positively and negatively charged ions are represented by δ^+ and δ^- , respectively. Panels (e) and (f) illustrate the schematic of the three-dimensional structure of $CH_3NH_3PbI_3$ prior to and after being influenced by illumination (inducing ion migration), respectively. Note that in (f) upon applying a strong field, the MA^+ ion has migrated out of the cuboctahedral space which would cause a severe structural distortion.

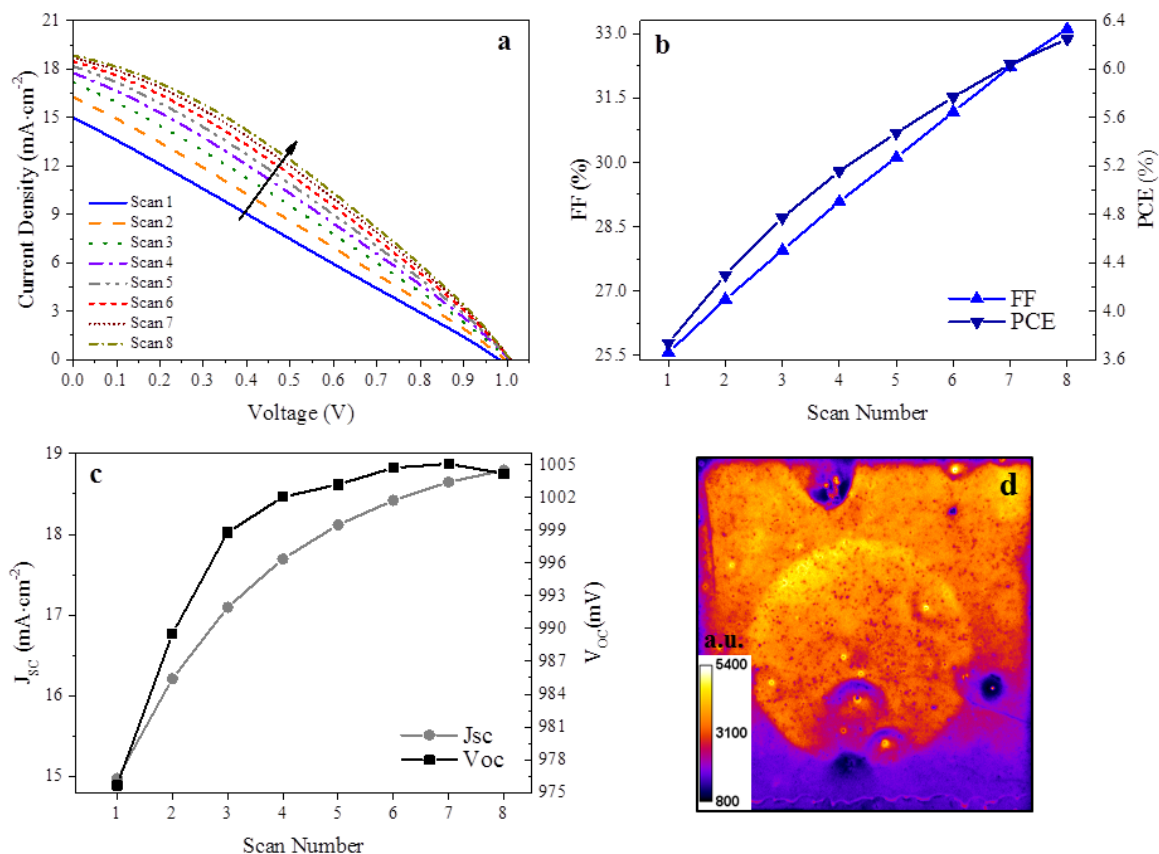


Figure 4.24 PV characteristics of an aged device. a) J - V curves for eight consecutive FR ($V_{oc} \rightarrow J_{sc}$) J - V scans on Cell 2 measured after 45 days from the first J - V characterization with no J - V measurements performed meantime. Photovoltaic parameters are presented in (b) for FF and PCE and in (c) for J_{sc} and V_{oc} . d) EL^{1.15V} image of Cell 2 collected after J - V characterization. This spatial image clearly shows that the J - V scans on the fresh and the aged device was performed with a good approximation at a similar location.

Another important implication of the findings of this study is that when performing credible long-term stability and degradation investigations of perovskite solar cells and in particular when using the conventional architecture explored here, the aperture used for the J - V measurements must be always located in the same position. It is clear that previously light-exposed regions degrade at different rates than the surrounding which has only experienced the external E-field.

In summary, spatially-resolved luminescence imaging has been applied to demonstrate an intrinsic disadvantage of the compact $\text{TiO}_2/\text{CH}_3\text{NH}_3\text{PbI}_3$ interface. Delamination between c- TiO_2 and $\text{CH}_3\text{NH}_3\text{PbI}_3$ is significantly intensified in the light-exposed region and would be relevant to any procedure encompassing prolonged illumination of the device or J - V measurement with slow voltage sweep rate. This is because the underlying mechanism is assigned to the inherent collective migration of the interstitial ions/ion vacancies in the $\text{CH}_3\text{NH}_3\text{PbI}_3$ leading to the perovskite structure buckling over time. It is expected that perovskite compositions (such as the state-of-the-art mixed cation-mixed halide perovskites) which mitigate ionic migration and thus have less hysteresis would be less affected by this effect. We propose that, regardless of the use of mesoporous or compact TiO_2 , the incorporation of stoichiometric $\text{CH}_3\text{NH}_3\text{PbI}_3$ as the active layer will give rise to ion migration and lattice distortion and ultimately device performance degradation.

5 Conclusions and Future Work

Debate continues on the role of excitons and free carriers in organic-inorganic lead halide perovskites, primarily $\text{CH}_3\text{NH}_3\text{PbI}_3$ and the related halides involving bromide and chloride. Recent studies report values of exciton binding energy for $\text{CH}_3\text{NH}_3\text{PbI}_3$ ranging from 0.7 meV to 200 meV, with vastly different implications for device operation and design. In Chapter 2, previously neglected polarons were shown likely to have a major impact in determining excitonic properties of organic-inorganic lead halide perovskites. By including the polaronic effects, theoretical exciton binding energy values were obtained which fall intermediate between the extremes of previous calculations using the simple Wannier-Mott exciton model in which either the static, low-frequency, or optical, high-frequency, dielectric constants were employed. By evaluating an effective longitudinal optical (LO) phonon energy to describe these effects, we demonstrated higher exciton binding energies than if only the highest energy LO phonons are considered. Polaronic exciton binding energies calculated here using effective LO energies, deduced from permittivity measurements, are shown to be consistent with experimental energies for good quality polycrystalline samples of $\text{CH}_3\text{NH}_3\text{PbI}_3$ and $\text{CH}_3\text{NH}_3\text{PbBr}_3$, as determined over a large temperature range from optical absorption data. Bandgaps were also determined simultaneously which show a discontinuity at the orthorhombic to tetragonal phase transition for the iodide, but not for the bromide perovskite.

For future studies with regards to the excitonic effects in these semiconductors and to complete the puzzle of the role of exciton binding energy on the carrier transport properties in PSCs several as yet unanswered questions need to be elucidated. One is the impact of the microstructure, the degree of polycrystallinity and the crystal quality, on this parameter. Although quite recently one study attempted to resolve this [17], a more robust and direct approach to understand the correlation between the crystal quality/size and the binding energy is necessary to get the ultimate verdict of the binding energy trend. The change in electron-hole

instantaneous interaction upon photo-excitation is in particular interesting when the perovskite material is infiltrated in the mesoporous scaffolds (e.g. mesoporous Al_2O_3 or mesoporous TiO_2) also used as device architecture. These issues are currently under in-depth investigation.

Another important but less attended notion is the understanding of the appropriate dielectric medium influencing the exciton binding energy in organic-inorganic lead halide perovskites. As discussed in Chapter 2, electronic, ionic, molecular dipole and ionic migration contribute to the relative permittivity of these materials each having different temperature-dependent behaviour and have a share in the very large values of real part of the permittivity (equal or more than 60) at radio frequencies. A systematic temperature-dependent study of the exciton binding energy and dielectric constants on high-quality polycrystalline and/or single crystal perovskites is deemed necessary to unravel the correct frequency at which the static dielectric constant can be obtained. It is noteworthy that the assessment presented in section 3.2.2 of this thesis, tentatively proposed the microwave frequency, principally associated with the vibrational modes of Pb-I bonds of the PbI_6^{2-} cage, as the relevant range for the measurement of the static dielectric constant taking into account only ionic and electronic screening of the electron-hole system.

In Chapter 3, we provided insights into planar structure $\text{CH}_3\text{NH}_3\text{PbI}_3$ -based solar cells using electroluminescence and photoluminescence imaging techniques. First, the fundamental correlation between luminescence intensity and the open-circuit voltage predicted by the generalised Planck law was confirmed, enabling various quantitative methods for the detection of efficiency limiting defects to be applied to these new types of solar cell structure. Interestingly, it was found that in the devices showing hysteretic behaviour, this fundamental correlation, investigated using PL imaging, is valid only when the device is properly light-soaked. For future studies, it will be insightful to examine the impact of light-soaking preconditioning of the device on the radiative ideality factor extracted using EL imaging.

We further demonstrated the strength of these techniques in screening relatively large area PSCs, correlating the solar cell electrical parameters to the spatially-resolved luminescence images and visualizing the features which contribute to the variation of the parameters extracted from current density-voltage characterizations. It was further used to investigate one of the major concerns about perovskite solar cells; their long term stability and aging. Upon storage in the dark in dry glovebox condition for more than two months, the major parameter found to have deteriorated in electrical performance measurements was the fill factor; this was elucidated via electroluminescence image comparisons which revealed that the contacts quality degrades. Interestingly, by deploying electroluminescence imaging the significance of having a pin-hole free active layer was demonstrated. Pin-holes can grow over time and can cause degradation of the active layer surrounding them even when devices were stored in dry glovebox environment. Moreover, EL imaging was revealed to be a suitable technique to investigate the effect of reversible illumination induced changes in the device. This effect was explored in Chapter 4.

In Chapter 4, fast and spatially-resolved luminescence imaging was applied to demonstrate an intrinsic disadvantage of the compact $\text{TiO}_2/\text{CH}_3\text{NH}_3\text{PbI}_3$ interface. We analysed the effect of illuminated current density-voltage and light-soaking measurements on pristine PSCs by providing visual evidence for the spatial inhomogeneous evolution of device performance. Regions that are exposed to light initially produce stronger electroluminescence signals than surrounding unilluminated regions, mainly due to a lower contact resistance and, possibly, higher charge collection efficiency. Over a period of several days, however, these initially illuminated regions appear to degrade more quickly despite the device being stored in a dark, moisture- and oxygen-free environment. Using transmission electron microscopy, this accelerated degradation was attributed to delamination between the perovskite and the titanium dioxide layer. The delamination between compact TiO_2 and $\text{CH}_3\text{NH}_3\text{PbI}_3$ which was significantly intensified in the light-exposed region would be relevant to any procedure encompassing prolonged illumination of the device or light current-voltage measurement with slow voltage sweep rate. This is because the underlying mechanism is assigned to the inherent

collective migration of the interstitial ions/ion vacancies in the $\text{CH}_3\text{NH}_3\text{PbI}_3$ leading to the perovskite structure buckling over time. It is expected that perovskite compositions (such as the state-of-the-art mixed cation-mixed halide perovskites) which mitigate ionic migration and thus have less hysteresis would be less affected by this effect. We propose that, regardless of the use of mesoporous or compact TiO_2 , the incorporation of stoichiometric $\text{CH}_3\text{NH}_3\text{PbI}_3$ as the active layer will give rise to ion migration and lattice distortion and ultimately device performance degradation. These results have major implications for the design of PSCs from the standpoint of long-term performance and stability.

In the next steps for the future studies, similar investigation needs to be conducted on PSCs with inverted structures using organic selective contacts and also mesoporous metal oxide contacts in order to unravel the potential role of various charge carrier collecting interfaces. Also, the compositionally engineered perovskite materials incorporating mixed-cation (methyammonium, formammidinum and caesium) and mixed-halide (iodide and bromide) which has been shown to reduce the hysteresis in the current-voltage characteristic of PSCs will be considered for the exploration of the light-induced interface versus bulk evolution over time. Integration of a proper concentration of PbI_2 into the archetypical $\text{CH}_3\text{NH}_3\text{PbI}_3$ perovskite material has been demonstrated as another technique to mitigate the hysteresis in the PSC counterparts. Expecting this additive to slow down the transport of the ions in the device, we will perform thorough study to find out PbI_2 role in the long-term opto-electronic response of such devices using the imaging tools used in Chapter 4.

Understanding the fate of the photo-excited charge carriers in the bulk and at the interfaces of the PSCs is another essential step towards designing and incorporating appropriate selective contacts and developing fabrication technique which provide high-quality perovskite active layer. This will be performed using excitation wavelength-dependent and intensity-dependent spatially resolved photoluminescence imaging technique elaborated in Chapter 3 and 4 of this thesis.

As the *final remark*, although several studies have clearly demonstrated different levels of vulnerability of various types of high efficiency PSCs to humidity, oxidation, intense ultra-violet irradiation and high temperatures [6, 216, 229] – which in some cases can be mitigated by employing robust and costly encapsulation techniques or through compositional engineering (such as fully or partially replacement of organic cation by Caesium [29, 230], for thermal stability improvement, which its cost effectiveness needs to be considered) – there seems to be a greater concern about the intrinsic instability of organic-inorganic metal halide perovskites due to the inherent ion migration phenomena even under mild environmental conditions [166, 177, 220]. As in real conditions, where a solar cell is under continuous bias condition, one initial step for the potential deployment of these intriguing types of semiconductors in the PV market could be their laboratory-scale monitoring under prolonged (i.e. tens of hours) continuous electrical and photo-induced charge injection. This would help to understand the fate of mobile ions and the consequence of their accumulation in the space-charge regions of the various device architectures using different perovskite compositions – particularly important is their critical impact on the electrical junctions over long terms.

It is worthwhile to note that in order to achieve more robust outcomes for performance and stability behaviour of perovskite solar cells using luminescence-based imaging techniques employed in this thesis, complementary techniques such as cross-sectional PL mapping by Scanning Near-field Optical Microscopy and methods like series resistance and photocurrent mapping – by analysis of multiple images taken under various charge-carrier injection levels – to be employed in future works.

It seems that comprehensive understanding of the origin of short- and long-term stability of PSCs and tackling these appropriately are crucial steps towards reliable commercial application of perovskite opto-electronic devices.

List of Publications

Perovskite Related Journal Articles

Arman Mahboubi Soufiani, Zhou Yang, Trevor Young, Atsuhiko Miyata, Alessandro Surrente, Alexander Pascoe, Krzysztof Galkowski, Mojtaba Abdi-Jalebi, Roberto Brenes, Joanna Urban, Nan Zhang, Vladimir Bulović, Oliver Portugall, Yi-Bing Cheng, Robin J. Nicholas, Anita Ho-Baillie, Martin A. Green, Paulina Plochocka, Samuel D. Stranks, *Impact of Microstructure on the Electron-hole Interaction in Metal Halide Perovskites*. Energy & Environmental Science, 2017 (DOI: 10.1039/C7EE00685C).

A.M. Soufiani, Z. Hameiri, S. Meyer, S. Lim, M.J.Y. Tayebjee, J.S. Yun, A. Ho-Baillie, G.J. Conibeer, L. Spiccia, M.A. Green, *Lessons Learnt from Spatially-resolved Electro- and Photoluminescence Imaging: Interfacial Delamination in $\text{CH}_3\text{NH}_3\text{PbI}_3$ Planar Perovskite Solar Cells upon Illumination*. Advanced Energy Materials, 2016. p. 1602111.

A.M. Soufiani, M.J.Y. Tayebjee, S. Meyer, A. Ho-Baillie, J.S. Yun, W.R. MacQueen, et al., *Electro- and photoluminescence imaging as fast screening technique of the layer uniformity and device degradation in planar perovskite solar cells*. Journal of Applied Physics, 2016. **120**: p. 035702.

A.M. Soufiani, F. Huang, P. Reece, R. Sheng, A. Ho-Baillie, and M.A. Green, *Polaronic exciton binding energy in iodide and bromide organic-inorganic lead halide perovskites*. Applied Physics Letters, 2015. **107**: p. 231902.

Hameiri, Z., A. Mahboubi Soufiani, M.K. Juhl, L. Jiang, F. Huang, Y.-B. Cheng, et al., *Photoluminescence and electroluminescence imaging of perovskite solar cells*. Progress in Photovoltaics: Research and Applications, 2015. **23**: p. 1697-1705.

Jiang, Y., A.M. Soufiani, A. Gentle, F. Huang, A. Ho-Baillie, and M.A. Green, *Temperature dependent optical properties of $\text{CH}_3\text{NH}_3\text{PbI}_3$ perovskite by spectroscopic ellipsometry*. Applied Physics Letters, 2016. **108**: p. 061905.

Guse, J.A., A.M. Soufiani, L. Jiang, J. Kim, Y.-B. Cheng, T.W. Schmidt, et al., *Spectral dependence of direct and trap-mediated recombination processes in lead halide perovskites using time resolved microwave conductivity*. Physical Chemistry Chemical Physics, 2016. **18**: p. 12043-12049.

Green, M.A., Y. Jiang, **A.M. Soufiani**, and A. Ho-Baillie, *Optical properties of photovoltaic organic–inorganic lead halide perovskites*. The Journal of Physical Chemistry Letters, 2015: p. 4774-4785.

Yun, J.S., J. Seidel, J. Kim, **A.M. Soufiani**, S. Huang, J. Lau, et al., *Critical role of grain boundaries for ion migration in formamidinium and methylammonium lead halide perovskite solar cells*. Advanced Energy Materials, 2016.

Kim, J., J.S. Yun, X. Wen, **A.M. Soufiani**, C.F.J. Lau, B. Wilkinson, et al., *Nucleation and growth control of $\text{HC}(\text{NH}_2)_2\text{PbI}_3$ for planar perovskite solar cell*. The Journal of Physical Chemistry C, 2016.

Non-perovskite Related Journal Articles

Tayebjee, M., **A. Mahboubi Soufiani**, and G. Conibeer, *Semi-empirical limiting efficiency of singlet-fission-capable polyacene/inorganic hybrid solar cells*. The Journal of Physical Chemistry C, 2014. **118**: p. 2298-2305.

Conference Oral Presentations

Arman M. Soufiani, Ziv Hameiri, Murad J. Y. Tayebjee, Liangcong Jiang, Yi-Bing Cheng, Anita Ho-Baillie, Thorsten Trupke, Martin A. Green (2015), *Full Device Photoluminescence and Electroluminescence Imaging of Perovskite Solar Cells*, PSCO 2015, Lausanne, Switzerland.

Arman Mahboubi Soufiani, Ziv Hameiri, Mattias K. Juhl, Fuzhi Huang, Liangcong Jiang, Yi-Bing Cheng, Anita Ho-Baillie, Thorsten Trupke, Martin A. Green (2015), *Full Device Photoluminescence and Electroluminescence Imaging of Organic-Inorganic Perovskite Solar Cells*, SPINS 2015, Santiago de Compostela, Spain.

Arman M. Soufiani, Murad JY Tayebjee, Anita Ho-Baillie, Gavin Conibeer and Martin A. Green (2014), *From Low-Temperature to High-Temperature Phase Exciton Binding Energy and Band Gap Evaluation of $\text{CH}_3\text{NH}_3\text{PbI}_3$ and $\text{CH}_3\text{NH}_3\text{PbI}_3\text{-XCl}_x$ Perovskites*, 2014 Asia-Pacific Solar Research Conference, Sydney, Australia.

Murad J.Y. Tayebjee, Raphaël G.C.R. Clady, Angus A. Gray-Weale, **A. Mahboubi Soufiani**, Gavin J. Conibeer, Timothy W. Schmidt (2013), *The role of entropy in the limiting efficiency of*

exciton fission solar cells: Can tetracene be used?, 28th European Photovoltaic Solar Energy Conference, Paris, France.

Conference Poster Presentations

Arman Mahboubi Soufiani, Fuzhi Huang, Peter Reece, Rui Sheng, Murad Tayebjee, Anita Ho-Baillie, Yi-Bing Cheng, Martin A. Green (2015), *Exciton Binding Energy of Methylammonium Lead Tri-iodide and Tri-bromide Perovskites: The Importance of Polarons*, HOPV 2015, Rome, Italy.

Murad J.Y. Tayebjee, Raphaël G.C.R. Clady, A. Mahboubi Soufiani, Timothy W. Schmidt, Gavin J. Conibeer, (2015) *Singlet fission in polycrystalline tetracene and its application to organic/inorganic hybrid solar cells*, Singlet Fission Workshop, Colorado, USA.

References

1. *The paris agreement*. 2015; Available from: <http://www.c2es.org/international/paris-agreement?gclid=Cj0KEQjw3ZS-BRD1xu3qw8uS2s4BEiQA2bcfM4fy5zE9e90luSg-MohziXHH0GhqQVgyd9tbL153a78aApBF8P8HAQ>.
2. Tsao, J.Y. *Jeff y tsao selected papers, presentation, etc.* 2015; Available from: <http://www.sandia.gov/~jytsao/>.
3. Green, M.A., *Commercial progress and challenges for photovoltaics*. Nature Energy, 2016. **1**: p. 15015.
4. Green, M.A., A. Ho-Baillie, and H.J. Snaith, *The emergence of perovskite solar cells*. Nat Photon, 2014. **8**: p. 506-514.
5. Jørgensen, M., K. Norrman, S.A. Gevorgyan, T. Tromholt, B. Andreasen, and F.C. Krebs, *Stability of polymer solar cells*. Advanced Materials, 2012. **24**: p. 580-612.
6. Wang, D., M. Wright, N.K. Elumalai, and A. Uddin, *Stability of perovskite solar cells*. Solar Energy Materials and Solar Cells, 2016. **147**: p. 255-275.
7. Stranks, S.D. and H.J. Snaith, *Metal-halide perovskites for photovoltaic and light-emitting devices*. Nature Nanotechnology, 2015. **10**: p. 391-402.
8. Green, M.A., K. Emery, Y. Hishikawa, W. Warta, and E.D. Dunlop, *Solar cell efficiency tables (version 46)*. Progress in Photovoltaics: Research and Applications, 2015. **23**: p. 805-812.
9. Kojima, A., K. Teshima, Y. Shirai, and T. Miyasaka, *Organometal halide perovskites as visible-light sensitizers for photovoltaic cells*. Journal of the American Chemical Society, 2009. **131**: p. 6050-6051.
10. Jeon, N.J., J.H. Noh, W.S. Yang, Y.C. Kim, S. Ryu, J. Seo, and S.I. Seok, *Compositional engineering of perovskite materials for high-performance solar cells*. Nature, 2015. **517**: p. 476-480.
11. Li, X., D. Bi, C. Yi, J.-D. Décoppet, J. Luo, S.M. Zakeeruddin, A. Hagfeldt, and M. Grätzel, *A vacuum flash-assisted solution process for high-efficiency large-area perovskite solar cells*. Science, 2016.
12. *Nrel efficiency chart*. 2016 [cited 2016; Available from: http://www.nrel.gov/ncpv/images/efficiency_chart.jpg].
13. Manser, J.S., J.A. Christians, and P.V. Kamat, *Intriguing optoelectronic properties of metal halide perovskites*. Chemical Reviews, 2016.
14. Lin, Q., A. Armin, P.L. Burn, and P. Meredith, *Organohalide perovskites for solar energy conversion*. Accounts of Chemical Research, 2016. **49**: p. 545-553.
15. Kim, J., J.S. Yun, X. Wen, A.M. Soufiani, C.F.J. Lau, B. Wilkinson, J. Seidel, M.A. Green, S. Huang, and A.W.Y. Ho-Baillie, *Nucleation and growth control of $\text{hc}(\text{nh}_2)_2\text{pb}i_3$ for planar perovskite solar cell*. The Journal of Physical Chemistry C, 2016. **120**: p. 11262-11267.
16. Sutton, R.J., G.E. Eperon, L. Miranda, E.S. Parrott, B.A. Kamino, J.B. Patel, M.T. Hörantner, M.B. Johnston, A.A. Haghighirad, D.T. Moore, and H.J. Snaith, *Bandgap-tunable cesium lead halide perovskites with high thermal stability for efficient solar cells*. Advanced Energy Materials, 2016: p. n/a-n/a.
17. Grancini, G., A.R. Srimath Kandada, J.M. Frost, A.J. Barker, M. De Bastiani, M. Gandini, S. Marras, G. Lanzani, A. Walsh, and A. Petrozza, *Role of microstructure in the electron-hole interaction of hybrid lead halide perovskites*. Nat Photon, 2015. **9**: p. 695-701.
18. D'Innocenzo, V., A.R. Srimath Kandada, M. De Bastiani, M. Gandini, and A. Petrozza, *Tuning the light emission properties by band gap engineering in hybrid lead-halide perovskite*. Journal of the American Chemical Society, 2014. **136**: p. 17730-17733.

19. Almansouri, I., A. Ho-Baillie, and M.A. Green, *Ultimate efficiency limit of single-junction perovskite and dual-junction perovskite/silicon two-terminal devices*. Japanese Journal of Applied Physics, 2015. **54**: p. 08KD04.
20. Soufiani, A.M., F. Huang, P. Reece, R. Sheng, A. Ho-Baillie, and M.A. Green, *Polaronic exciton binding energy in iodide and bromide organic-inorganic lead halide perovskites*. Applied Physics Letters, 2015. **107**: p. 231902.
21. Miyata, A., A. Mitoglu, P. Plochocka, O. Portugall, J.T.-W. Wang, S.D. Stranks, H.J. Snaith, and R.J. Nicholas, *Direct measurement of the exciton binding energy and effective masses for charge carriers in organic-inorganic tri-halide perovskites*. Nat Phys, 2015. **11**: p. 582–587.
22. Galkowski, K., A. Mitoglu, a. miyata, p. plochocka, o. Portugall, G.E. Eperon, J.T.-W. Wang, T. Stergiopoulos, S.D. Stranks, H. Snaith, and R.J. Nicholas, *Determination of the exciton binding energy and effective masses for methylammonium and formamidinium lead tri-halide perovskite semiconductors*. Energy & Environmental Science, 2016. **9**: p. 962-970.
23. Ziffer, M.E., J.C. Mohammed, and D.S. Ginger, *Electroabsorption spectroscopy measurements of the exciton binding energy, electron-hole reduced effective mass, and band gap in the perovskite $\text{CH}_3\text{NH}_3\text{PbI}_3$* . ACS Photonics, 2016. **3**: p. 1060–1068.
24. Stranks, S.D., G.E. Eperon, G. Grancini, C. Menelaou, M.J.P. Alcocer, T. Leijtens, L.M. Herz, A. Petrozza, and H.J. Snaith, *Electron-hole diffusion lengths exceeding 1 micrometer in an organometal trihalide perovskite absorber*. Science, 2013. **342**: p. 341-344.
25. Dong, Q., Y. Fang, Y. Shao, P. Mulligan, J. Qiu, L. Cao, and J. Huang, *Electron-hole diffusion lengths > 175 μm in solution-grown $\text{CH}_3\text{NH}_3\text{PbI}_3$ single crystals*. Science, 2015. **347**: p. 967-970.
26. Yusoff, A.R.b.M. and M.K. Nazeeruddin, *Organohalide lead perovskites for photovoltaic applications*. The Journal of Physical Chemistry Letters, 2016. **7**: p. 851-866.
27. Deschler, F., M. Price, S. Pathak, L.E. Klintberg, D.-D. Jarausch, R. Higler, S. Hüttner, T. Leijtens, S.D. Stranks, H.J. Snaith, M. Atatüre, R.T. Phillips, and R.H. Friend, *High photoluminescence efficiency and optically pumped lasing in solution-processed mixed halide perovskite semiconductors*. The Journal of Physical Chemistry Letters, 2014. **5**: p. 1421-1426.
28. Bi, D., W. Tress, M.I. Dar, P. Gao, J. Luo, C. Renevier, K. Schenk, A. Abate, F. Giordano, J.-P. Correa Baena, J.-D. Decoppet, S.M. Zakeeruddin, M.K. Nazeeruddin, M. Grätzel, and A. Hagfeldt, *Efficient luminescent solar cells based on tailored mixed-cation perovskites*. Science Advances, 2016. **2**: p. 1-7.
29. Saliba, M., T. Matsui, J.-Y. Seo, K. Domanski, J.-P. Correa-Baena, N. Mohammad K, S.M. Zakeeruddin, W. Tress, A. Abate, A. Hagfeldt, and M. Gratzel, *Cesium-containing triple cation perovskite solar cells: Improved stability, reproducibility and high efficiency*. Energy & Environmental Science, 2016. **9**: p. 1989-1997.
30. McMeekin, D.P., G. Sadoughi, W. Rehman, G.E. Eperon, M. Saliba, M.T. Hörantner, A. Haghighirad, N. Sakai, L. Korte, B. Rech, M.B. Johnston, L.M. Herz, and H.J. Snaith, *A mixed-cation lead mixed-halide perovskite absorber for tandem solar cells*. Science, 2016. **351**: p. 151-155.
31. Quarti, C., E. Mosconi, J.M. Ball, V. D'Innocenzo, C. Tao, S. Pathak, H.J. Snaith, A. Petrozza, and F. De Angelis, *Structural and optical properties of methylammonium lead iodide across the tetragonal to cubic phase transition: Implications for perovskite solar cells*. Energy & Environmental Science, 2015.
32. Onoda-Yamamuro, N., T. Matsuo, and H. Suga, *Dielectric study of $\text{CH}_3\text{NH}_3\text{PbX}_3$ ($\text{X} = \text{Cl}, \text{Br}, \text{I}$)*. Journal of Physics and Chemistry of Solids, 1992. **53**: p. 935-939.
33. Chen, S., Y. Hou, H. Chen, M. Richter, F. Guo, S. Kahmann, X. Tang, T. Stubhan, H. Zhang, N. Li, N. Gasparini, C.O.R. Quiroz, L.S. Khanzada, G.J. Matt, A. Osvet, and C.J. Brabec, *Exploring the limiting open-circuit voltage and the voltage loss mechanism*

- in planar ch₃nh₃pbbi₃ perovskite solar cells*. Advanced Energy Materials, 2016: p. n/a-n/a.
34. Jiang, Y., A.M. Soufiani, A. Gentle, F. Huang, A. Ho-Baillie, and M.A. Green, *Temperature dependent optical properties of ch₃nh₃pbi₃ perovskite by spectroscopic ellipsometry*. Applied Physics Letters, 2016. **108**: p. 061905.
 35. Lin, Q., A. Armin, R.C.R. Nagiri, P.L. Burn, and P. Meredith, *Electro-optics of perovskite solar cells*. Nature Photonics, 2014. **9**: p. 106–112.
 36. D’Innocenzo, V., G. Grancini, M.J.P. Alcocer, A.R.S. Kandada, S.D. Stranks, M.M. Lee, G. Lanzani, H.J. Snaith, and A. Petrozza, *Excitons versus free charges in organo-lead tri-halide perovskites*. Nat Commun, 2014. **5**: p. 3586.
 37. Hellwarth, R.W. and I. Biaggio, *Mobility of an electron in a multimode polar lattice*. Physical Review B, 1999. **60**: p. 299.
 38. Trupke, T., B. Mitchell, J. Weber, W. McMillan, R. Bardos, and R. Kroeze, *Photoluminescence imaging for photovoltaic applications*. Energy Procedia, 2012. **15**: p. 135-146.
 39. Hameiri, Z., A. Mahboubi Soufiani, M.K. Juhl, L. Jiang, F. Huang, Y.-B. Cheng, H. Kampwerth, J.W. Weber, M.A. Green, and T. Trupke, *Photoluminescence and electroluminescence imaging of perovskite solar cells*. Progress in Photovoltaics: Research and Applications, 2015. **23**: p. 1697-1705.
 40. Diab, H., G. Trippé-Allard, F. Lédée, K. Jemli, C. Vilar, G. Bouchez, V.L. Jacques, A. Tejada, J.-S. Lauret, and E. Deleporte, *Excitonic emission in organic-inorganic lead iodide perovskite single crystals*. arXiv preprint arXiv:1606.01729, 2016.
 41. Tilchin, J., D.N. Dirin, G.I. Maikov, A. Sashchiuk, M.V. Kovalenko, and E. Lifshitz, *Hydrogen-like wannier–mott excitons in single crystal of methylammonium lead bromide perovskite*. ACS Nano, 2016. **10**: p. 6363-6371.
 42. Chen, Q., H. Zhou, Z. Hong, S. Luo, H.-S. Duan, H.-H. Wang, Y. Liu, G. Li, and Y. Yang, *Planar heterojunction perovskite solar cells via vapor assisted solution process*. Journal of the American Chemical Society, 2013.
 43. Liu, M., M.B. Johnston, and H.J. Snaith, *Efficient planar heterojunction perovskite solar cells by vapour deposition*. Nature, 2013. **501**: p. 395-398.
 44. Burschka, J., N. Pellet, S.-J. Moon, R. Humphry-Baker, P. Gao, M.K. Nazeeruddin, and M. Gratzel, *Sequential deposition as a route to high-performance perovskite-sensitized solar cells*. Nature, 2013. **499**: p. 316-319.
 45. Heo, J.H., S.H. Im, J.H. Noh, T.N. Mandal, C.-S. Lim, J.A. Chang, Y.H. Lee, H.-j. Kim, A. Sarkar, K. NazeeruddinMd, M. Gratzel, and S.I. Seok, *Efficient inorganic-organic hybrid heterojunction solar cells containing perovskite compound and polymeric hole conductors*. Nat Photon, 2013. **7**: p. 486-491.
 46. Huang, F., Y. Dkhissi, W. Huang, M. Xiao, I. Benesperi, S. Rubanov, Y. Zhu, X. Lin, L. Jiang, and Y. Zhou, *Gas-assisted preparation of lead iodide perovskite films consisting of a monolayer of single crystalline grains for high efficiency planar solar cells*. Nano Energy, 2014. **10**: p. 10-18.
 47. Tao, C., S. Neutzner, L. Colella, S. Marras, A.R. Srimath Kandada, M. Gandini, M.D. Bastiani, G. Pace, L. Manna, M. Caironi, C. Bertarelli, and A. Petrozza, *17.6% stabilized efficiency in low-temperature processed planar perovskite solar cells*. Energy & Environmental Science, 2015. **8**: p. 2365-2370.
 48. Brown, G., A. Pudov, B. Cardozo, V. Faifer, E. Bykov, and M. Contreras, *Quantitative imaging of electronic nonuniformities in cu (in, ga) se₂ solar cells*. Journal of Applied Physics, 2010. **108**: p. 074516.
 49. Green, M.A., Y. Jiang, A. Mahboubi Soufiani, and A.W.-Y. Ho-Baillie, *Optical properties of photovoltaic organic-inorganic lead halide perovskites*. The Journal of Physical Chemistry Letters, 2015.
 50. Chen, B., M. Yang, X. Zheng, C. Wu, W. Li, Y. Yan, J. Bisquert, G. Garcia-Belmonte, K. Zhu, and S. Priya, *Impact of capacitive effect and ion migration on the hysteretic behavior of perovskite solar cells*. The Journal of Physical Chemistry Letters, 2015.

51. de Quilettes, D.W., S.M. Vorpahl, S.D. Stranks, H. Nagaoka, G.E. Eperon, M.E. Ziffer, H.J. Snaith, and D.S. Ginger, *Impact of microstructure on local carrier lifetime in perovskite solar cells*. Science, 2015. **348**: p. 683-686.
52. Vrućinić, M., C. Matthiesen, A. Sadhanala, G. Divitini, S. Cacovich, S.E. Dutton, C. Ducati, M. Atatüre, H. Snaith, R.H. Friend, H. Sirringhaus, and F. Deschler, *Local versus long-range diffusion effects of photoexcited states on radiative recombination in organic-inorganic lead halide perovskites*. Advanced Science, 2015. **2**: p. 1500136.
53. Berhe, T.A., W.-N. Su, C.-H. Chen, C.-J. Pan, J.-H. Cheng, H.-M. Chen, M.-C. Tsai, L.-Y. Chen, A.A. Dubale, and B.-J. Hwang, *Organometal halide perovskite solar cells: Degradation and stability*. Energy & Environmental Science, 2016. **9**: p. 323-356.
54. Leijtens, T., G.E. Eperon, N.K. Noel, S.N. Habisreutinger, A. Petrozza, and H.J. Snaith, *Stability of metal halide perovskite solar cells*. Advanced Energy Materials, 2015. **5**: p. n/a-n/a.
55. Seeland, M., R. Rösch, and H. Hoppe, *Luminescence imaging of polymer solar cells: Visualization of progressing degradation*. Journal of Applied Physics, 2011. **109**: p. 064513.
56. Rosch, R., D.M. Tanenbaum, M. Jorgensen, M. Seeland, M. Barenklau, M. Hermenau, E. Voroshazi, M.T. Lloyd, Y. Galagan, B. Zimmermann, U. Wurfel, M. Hosel, H.F. Dam, S.A. Gevorgyan, S. Kudret, W. Maes, L. Lutsen, D. Vanderzande, R. Andriessen, G. Teran-Escobar, M. Lira-Cantu, A. Rivaton, G.Y. Uzunoglu, D. Germack, B. Andreasen, M.V. Madsen, K. Norrman, H. Hoppe, and F.C. Krebs, *Investigation of the degradation mechanisms of a variety of organic photovoltaic devices by combination of imaging techniques-the isos-3 inter-laboratory collaboration*. Energy & Environmental Science, 2012. **5**: p. 6521-6540.
57. Klingshirn, C.F., *Semiconductor optics*. Vol. 3. 2007: Springer.
58. Le Toullec, R., N. Piccioli, and J. Chervin, *Optical properties of the band-edge exciton in gas crystals at 10 k*. Physical Review B, 1980. **22**: p. 6162.
59. Passler, R., E. Griehl, H. Riepl, G. Lautner, S. Bauer, H. Preis, W. Gebhardt, B. Buda, D. As, and D. Schikora, *Temperature dependence of exciton peak energies in zns, znse, and znTe epitaxial films*. Journal of applied physics, 1999. **86**: p. 4403-4411.
60. Turner, W., W. Reese, and G. Pettit, *Exciton absorption and emission in inp*. Physical Review, 1964. **136**: p. A1467.
61. Sell, D.D. and P. Lawaetz, *New analysis of direct exciton transitions: Application to gap*. Physical Review Letters, 1971. **26**: p. 311-314.
62. Sturge, M.D., *Optical absorption of gallium arsenide between 0.6 and 2.75 ev*. Physical Review, 1962. **127**.
63. Bernardo, B., D. Cheyns, B. Verreert, R.D. Schaller, B.P. Rand, and N.C. Giebink, *Delocalization and dielectric screening of charge transfer states in organic photovoltaic cells*. Nat Commun, 2014. **5**.
64. Devreese, J., *Polarons*. Encycl. Appl. Phys., 1996. **14**: p. 383-409.
65. Iadonisi, G. and F. Bassani, *Polaronic correction to the exciton effective mass*. Il Nuovo Cimento D, 1987. **9**: p. 703-714.
66. Herz, L.M., *Charge-carrier dynamics in organic-inorganic metal halide perovskites*. Annual Review of Physical Chemistry, 2016. **67**: p. 65-89.
67. Tayebjee, M.J.Y., D.R. McCamey, and T.W. Schmidt, *Beyond shockley-queisser: Molecular approaches to high-efficiency photovoltaics*. The Journal of Physical Chemistry Letters, 2015. **6**: p. 2367-2378.
68. Tayebjee, M., A. Mahboubi Soufiani, and G. Conibeer, *Semi-empirical limiting efficiency of singlet-fission-capable polyacene/inorganic hybrid solar cells*. The Journal of Physical Chemistry C, 2014. **118**: p. 2298-2305.
69. Sheng, C., C. Zhang, Y. Zhai, K. Mielczarek, W. Wang, W. Ma, A. Zakhidov, and Z.V. Vardeny, *Exciton versus free carrier photogeneration in organometal trihalide perovskites probed by broadband ultrafast polarization memory dynamics*. Physical review letters, 2015. **114**: p. 116601.

70. Ponseca Jr, C.S., T.J. Savenije, M. Abdellah, K. Zheng, A. Yartsev, T.r. Pascher, T. Harlang, P. Chabera, T. Pullerits, and A. Stepanov, *Organometal halide perovskite solar cell materials rationalized: Ultrafast charge generation, high and microsecond-long balanced mobilities, and slow recombination*. Journal of the American Chemical Society, 2014. **136**: p. 5189-5192.
71. Wehrenfennig, C., G.E. Eperon, M.B. Johnston, H.J. Snaith, and L.M. Herz, *High charge carrier mobilities and lifetimes in organolead trihalide perovskites*. Advanced Materials, 2013: p. n/a-n/a.
72. Even, J., L. Pedesseau, and C. Katan, *Analysis of multi-valley and multi-bandgap absorption and enhancement of free carriers related to exciton screening in hybrid perovskites*. The Journal of Physical Chemistry C, 2014. **118**: p. 11566–11572.
73. Yamada, Y., T. Nakamura, M. Endo, A. Wakamiya, and Y. Kanemitsu, *Photoelectronic responses in solution-processed perovskite $\text{CH}_3\text{NH}_3\text{PbI}_3$ solar cells studied by photoluminescence and photoabsorption spectroscopy*. IEEE Journal of Photovoltaics, 2014: p. 401 - 405.
74. Green, M.A., Y. Jiang, A.M. Soufiani, and A. Ho-Baillie, *Optical properties of photovoltaic organic–inorganic lead halide perovskites*. The Journal of Physical Chemistry Letters, 2015: p. 4774-4785.
75. Sestu, N., M. Cadelano, V. Sarritzu, F. Chen, D. Marongiu, R. Piras, M. Mainas, F. Quochi, M. Saba, A. Mura, and G. Bongiovanni, *Absorption f-sum rule for the exciton binding energy in methylammonium lead halide perovskites*. The Journal of Physical Chemistry Letters, 2015. **6**: p. 4566-4572.
76. Saba, M., M. Cadelano, D. Marongiu, F. Chen, V. Sarritzu, N. Sestu, C. Figus, M. Aresti, R. Piras, A. Geddo Lehmann, C. Cannas, A. Musinu, F. Quochi, A. Mura, and G. Bongiovanni, *Correlated electron–hole plasma in organometal perovskites*. Nat Commun, 2014. **5**.
77. Yang, Y., M. Yang, Z. Li, R. Crisp, K. Zhu, and M.C. Beard, *Comparison of recombination dynamics in $\text{CH}_3\text{NH}_3\text{PbBr}_3$ and $\text{CH}_3\text{NH}_3\text{PbI}_3$ perovskite films: Influence of exciton binding energy*. The Journal of Physical Chemistry Letters, 2015. **6**: p. 4688-4692.
78. Elliott, R.J., *Intensity of optical absorption by excitons*. Physical Review, 1957. **108**: p. 1384-1389.
79. Ishihara, T., *Optical properties of pbi-based perovskite structures*. Journal of Luminescence, 1994. **60–61**: p. 269-274.
80. Yang, Y., D.P. Ostrowski, R.M. France, K. Zhu, J. van de Lagemaat, J.M. Luther, and M.C. Beard, *Observation of a hot-phonon bottleneck in lead-iodide perovskites*. Nat Photon, 2015. **10**: p. 53–59.
81. Hirasawa, M., T. Ishihara, T. Goto, K. Uchida, and N. Miura, *Magnetoabsorption of the lowest exciton in perovskite-type compound $(\text{CH}_3\text{NH}_3)\text{PbI}_3$* . Physica B: Condensed Matter, 1994. **201**: p. 427-430.
82. Tanaka, K., T. Takahashi, T. Ban, T. Kondo, K. Uchida, and N. Miura, *Comparative study on the excitons in lead-halide-based perovskite-type crystals $\text{CH}_3\text{NH}_3\text{PbBr}_3$ $\text{CH}_3\text{NH}_3\text{PbI}_3$* . Solid State Communications, 2003. **127**: p. 619-623.
83. Poglitsch, A. and D. Weber, *Dynamic disorder in methylammoniumtrihalogenoplumbates (ii) observed by millimeter-wave spectroscopy*. The Journal of Chemical Physics, 1987. **87**: p. 6373-6378.
84. Huang, L.-y. and W.R. Lambrecht, *Electronic band structure, phonons, and exciton binding energies of halide perovskites CsSnI_3 , CsSnBr_3 , and CsSnI_2* . Physical Review B, 2013. **88**: p. 165203.
85. Zheng, K., Q. Zhu, M. Abdellah, M.E. Messing, W. Zhang, A. Generalov, Y. Niu, L. Ribaud, S.E. Canton, and T. Pullerits, *Exciton binding energy and the nature of emissive states in organometal halide perovskites*. The Journal of Physical Chemistry Letters, 2015. **6**: p. 2969-2975.

86. Savenije, T.J., C.S. Ponseca, L.T. Kunneman, M.A. Abdellah, K. Zheng, Y. Tian, Q. Zhu, S.E. Canton, I.G. Scheblykin, T. Pullerits, A.P. Yartsev, and V. Sundstrom, *Thermally activated exciton dissociation and recombination control the organometal halide perovskite carrier dynamics*. The Journal of Physical Chemistry Letters, 2014.
87. Wu, K., A. Bera, C. Ma, Y. Du, Y. Yang, L. Li, and T.T. Wu, *Temperature-dependent excitonic photoluminescence of hybrid organometal halide perovskite films*. Physical Chemistry Chemical Physics, 2014.
88. Sun, S., T. Salim, N. Mathews, M. Duchamp, C. Boothroyd, G. Xing, T.C. Sum, and Y.M. Lam, *The origin of high efficiency in low-temperature solution-processable bilayer organometal halide hybrid solar cells*. Energy & Environmental Science, 2014. **7**: p. 399-407.
89. Milot, R.L., G.E. Eperon, H.J. Snaith, M.B. Johnston, and L.M. Herz, *Temperature-dependent charge-carrier dynamics in $\text{CH}_3\text{NH}_3\text{PbI}_3$ perovskite thin films*. Advanced Functional Materials, 2015. **25**: p. 6218-6227.
90. Srimath Kandada, A.R. and A. Petrozza, *Photophysics of hybrid lead halide perovskites: The role of microstructure*. Accounts of Chemical Research, 2016. **49**: p. 536-544.
91. NahS, SpokoynyB, StoumposC, C.M.M. Soe, KanatzidisM, and HarelE, *Spatially segregated free-carrier and exciton populations in individual lead halide perovskite grains*. Nat Photon, 2017. **advance online publication**.
92. La-o-vorakiat, C., J.M. Kadro, T. Salim, D. Zhao, T. Ahmed, Y.M. Lam, J.-X. Zhu, R.A. Marcus, M.-E. Michel-Beyerle, and E.E.M. Chia, *Phonon mode transformation across the orthorhombic-tetragonal phase transition in a lead-iodide perovskite $\text{CH}_3\text{NH}_3\text{PbI}_3$: A terahertz time-domain spectroscopy approach*. The Journal of Physical Chemistry Letters, 2015.
93. Motta, C., P. Mandal, and S. Sanvito, *Effects of molecular dipole orientation on the exciton binding energy of $\text{CH}_3\text{NH}_3\text{PbI}_3$* . Physical Review B, 2016. **94**: p. 045202.
94. Quarti, C., G. Grancini, E. Mosconi, P. Bruno, J.M. Ball, M.M. Lee, H.J. Snaith, A. Petrozza, and F.D. Angelis, *The raman spectrum of the $\text{CH}_3\text{NH}_3\text{PbI}_3$ hybrid perovskite: Interplay of theory and experiment*. The Journal of Physical Chemistry Letters, 2013. **5**: p. 279-284.
95. Pérez-Osorio, M.A., R.L. Milot, M.R. Filip, J.B. Patel, L.M. Herz, M.B. Johnston, and F. Giustino, *Vibrational properties of the organic-inorganic halide perovskite $\text{CH}_3\text{NH}_3\text{PbI}_3$ from theory and experiment: Factor group analysis, first-principles calculations, and low-temperature infrared spectra*. The Journal of Physical Chemistry C, 2015. **119**: p. 25703-25718.
96. Leguy, A.M.A., A.R. Goni, J.M. Frost, J. Skelton, F. Brivio, X. Rodriguez-Martinez, O.J. Weber, A. Pallipurath, M.I. Alonso, M. Campoy-Quiles, M.T. Weller, J. Nelson, A. Walsh, and P.R.F. Barnes, *Dynamic disorder, phonon lifetimes, and the assignment of modes to the vibrational spectra of methylammonium lead halide perovskites*. Physical Chemistry Chemical Physics, 2016. **18**: p. 27051-27066.
97. Wang, W., Y. Li, X. Wang, Y. Lv, S. Wang, K. Wang, Y. Shi, L. Xiao, Z. Chen, and Q. Gong, *Density-dependent dynamical coexistence of excitons and free carriers in the organolead perovskite $\text{CH}_3\text{NH}_3\text{PbI}_3$* . Physical Review B, 2016. **94**: p. 140302.
98. Sheng, R., A. Ho-Baillie, S. Huang, S. Chen, X. Wen, X. Hao, and M.A. Green, *Methylammonium lead bromide perovskite-based solar cells by vapour-assisted deposition*. The Journal of Physical Chemistry C, 2015.
99. Frost, J.M., K.T. Butler, F. Brivio, C.H. Hendon, M. van Schilfgaarde, and A. Walsh, *Atomistic origins of high-performance in hybrid halide perovskite solar cells*. Nano Letters, 2014.
100. Nanguneri, R. and J. Parkhill, *Relaxation between bright optical wannier excitons in perovskite solar absorber $\text{CH}_3\text{NH}_3\text{PbI}_3$* . arXiv preprint arXiv:1411.1110, 2014.
101. Menéndez-Proupin, E., P. Palacios, P. Wahnón, and J.C. Conesa, *Self-consistent relativistic band structure of the $\text{CH}_3\text{NH}_3\text{PbI}_3$ perovskite*. Physical Review B, 2014. **90**.

102. Di Rocco, H. and A. Cruzado, *The voigt profile as a sum of a gaussian and a lorentzian functions, when the weight coefficient depends only on the widths ratio*. Acta Physica Polonica A, 2012. **122**: p. 666-669.
103. Toyozawa, Y., *Theory of line-shapes of the exciton absorption bands*. Progress of Theoretical Physics, 1958. **20**: p. 53-81.
104. Brivio, F., K.T. Butler, A. Walsh, and M. van Schilfgaarde, *Relativistic quasiparticle self-consistent electronic structure of hybrid halide perovskite photovoltaic absorbers*. Physical Review B, 2014. **89**.
105. Papavassiliou, G.C., G.A. Mousdis, I.B. Koutselas, and G.J. Papaioannou, *Excitonic bands in photoconductivity spectra of some organic-inorganic hybrid compounds based on metal halide units* International Journal of Modern Physics B, 2001. **15**: p. 3727-3731.
106. Hirasawa, M., T. Ishihara, and T. Goto, *Exciton features in 0-, 2-, and 3-dimensional networks of $[pb_i6]^{4-}$ octahedra*. Journal of the Physical Society of Japan, 1994. **63**: p. 3870-3879.
107. Shi, D., V. Adinolfi, R. Comin, M. Yuan, E. Alarousu, A. Buin, Y. Chen, S. Hoogland, A. Rothenberger, and K. Katsiev, *Low trap-state density and long carrier diffusion in organolead trihalide perovskite single crystals*. Science, 2015. **347**: p. 519-522.
108. Le Bahers, T., F. Labat, P. Sautet, and S. Melissen, *Electronic properties of $pbx_3ch_3nh_3$ ($x=cl, br, i$) compounds for photovoltaic and photocatalytic applications*. Physical Chemistry Chemical Physics, 2014.
109. Devreese, J.T. and A.S. Alexandrov, *Fröhlich polaron and bipolaron: Recent developments*. Reports on Progress in Physics, 2009. **72**: p. 066501.
110. Mahan, G., *Polarons in ionic crystals and polar semiconductors*. Proc. 1971 Antwerp Advanced Study Inst, 1972.
111. Kane, E.O., *Pollmann-büttner variational method for excitonic polarons*. Physical Review B, 1978. **18**: p. 6849.
112. Pollmann, J. and H. Büttner, *Effective hamiltonians and bindings energies of wannier excitons in polar semiconductors*. Physical Review B, 1977. **16**: p. 4480.
113. Carabatos-Nédelec, C., M. Oussaid, and K. Nitsch, *Raman scattering investigation of cesium plumbochloride, $cspbcl_3$, phase transitions*. Journal of Raman Spectroscopy, 2003. **34**: p. 388-393.
114. Brivio, F., J.M. Frost, J.M. Skelton, A.J. Jackson, O.J. Weber, M.T. Weller, A.R. Goni, A. Leguy, P.R. Barnes, and A. Walsh, *Lattice dynamics and vibrational spectra of the orthorhombic, tetragonal and cubic phases of methylammonium lead iodide*. arXiv preprint arXiv:1504.07508, 2015.
115. Rousseau, D., R.P. Bauman, and S. Porto, *Normal mode determination in crystals*. Journal of Raman Spectroscopy, 1981. **10**: p. 253-290.
116. Filippetti, A., P. Delugas, and A. Mattoni, *Methylammonium lead-iodide perovskite: Recombination and photoconversion of an inorganic semiconductor within a hybrid body*. The Journal of Physical Chemistry C, 2014.
117. Wehrenfennig, C., M. Liu, H.J. Snaith, M.B. Johnston, and I. Herz, *Charge-carrier dynamics in vapour-deposited films of the organolead halide perovskite $ch_3nh_3pb_i3-xcl_x$* . Energy & Environmental Science, 2014.
118. Giorgi, G., J.-I. Fujisawa, H. Segawa, and K. Yamashita, *Small photocarrier effective masses featuring ambipolar transport in methylammonium lead iodide perovskite: A density functional analysis*. The Journal of Physical Chemistry Letters, 2013. **4**: p. 4213-4216.
119. Evarestov, R.A., E. Blokhin, D. Gryaznov, E.A. Kotomin, and J. Maier, *Phonon calculations in cubic and tetragonal phases of $srtio_3$: A comparative lcao and plane-wave study*. Physical Review B, 2011. **83**: p. 134108.
120. Maalej, A., Y. Abid, A. Kallel, A. Daoud, A. Lautié, and F. Romain, *Phase transitions and crystal dynamics in the cubic perovskite $ch_3nh_3pbcl_3$* . Solid state communications, 1997. **103**: p. 279-284.

121. Ledinsky, M., P. Löper, B. Niesen, J. Holovsky, S.-J. Moon, J.-H. Yum, S. De Wolf, A. Fejfar, and C. Ballif, *Raman spectroscopy of organic-inorganic halide perovskites*. The Journal of Physical Chemistry Letters, 2015.
122. Chaves, A. and S. Porto, *Generalized lyddane-sachs-teller relation*. Solid State Communications, 1973. **13**: p. 865-868.
123. Maeda, M., M. Hattori, A. Hotta, and I. Suzuki, *Dielectric studies on $\text{ch}_3\text{nh}_3\text{pbx}_3$ ($x = \text{cl}$ and br) single crystals*. Journal of the Physical Society of Japan, 1997. **66**: p. 1508-1511.
124. Kumar, P., C. Muthu, V.C. Nair, and K.S. Narayan, *Quantum confinement effects in organic lead tribromide perovskite nanoparticles*. The Journal of Physical Chemistry C, 2016.
125. Kunugita, H., T. Hashimoto, Y. Kiyota, Y. Udagawa, Y. Takeoka, Y. Nakamura, J. Sano, T. Matsushita, T. Kondo, T. Miyasaka, and K. Ema, *Excitonic feature in hybrid perovskite $\text{ch}_3\text{nh}_3\text{pbbr}_3$ single crystals*. Chemistry Letters, 2015. **44**: p. 852-854.
126. Wehrenfennig, C., M. Liu, H.J. Snaith, M.B. Johnston, and L.M. Herz, *Homogeneous emission line broadening in the organo lead halide perovskite $\text{ch}_3\text{nh}_3\text{pb}(\text{I}-\text{x})\text{Cl}_x$* . The Journal of Physical Chemistry Letters, 2014: p. 1300-1306.
127. Wright, A.D., C. Verdi, R.L. Milot, G.E. Eperon, M.A. Perez-Osorio, H.J. Snaith, F. Giustino, M.B. Johnston, and L.M. Herz, *Electron-phonon coupling in hybrid lead halide perovskites*. Nat Commun, 2016. **7**.
128. Vorpahl, S.M., S.D. Stranks, H. Nagaoka, G.E. Eperon, M.E. Ziffer, H.J. Snaith, and D.S. Ginger, *Impact of microstructure on local carrier lifetime in perovskite solar cells*. Science, 2015: p. aaa5333.
129. Würfel, P., S. Finkbeiner, and E. Daub, *Generalized planck's radiation law for luminescence via indirect transitions*. Applied Physics A, 1995. **60**: p. 67-70.
130. Barugkin, C., J. Cong, T. Duong, S. Rahman, H.T. Nguyen, D. Macdonald, T.P. White, and K.R. Catchpole, *Ultralow absorption coefficient and temperature dependence of radiative recombination of $\text{ch}_3\text{nh}_3\text{pb}(\text{I}-\text{x})\text{Cl}_x$ perovskite from photoluminescence*. The Journal of Physical Chemistry Letters, 2015. **6**: p. 767-772.
131. Trupke, T., R. Bardos, M. Schubert, and W. Warta, *Photoluminescence imaging of silicon wafers*. Applied Physics Letters, 2006. **89**: p. 044107.
132. Helbig, A., T. Kirchartz, R. Schaeffler, J.H. Werner, and U. Rau, *Quantitative electroluminescence analysis of resistive losses in Cu(In,Ga)Se_2 thin-film modules*. Solar Energy Materials and Solar Cells, 2010. **94**: p. 979-984.
133. Mastroianni, S., F.D. Heinz, J.H. Im, W. Veurman, M. Padilla, M.C. Schubert, U. Würfel, M. Gratzel, N.G. Park, and A. Hinsch, *Analysing the effect of crystal size and structure in highly efficient $\text{ch}_3\text{nh}_3\text{pb}(\text{I}-\text{x})\text{Cl}_x$ perovskite solar cells by spatially resolved photo- and electroluminescence imaging*. Nanoscale, 2015. **7**: p. 19653-19662.
134. Handa, T., D.M. Tex, A. Shimazaki, T. Aharen, A. Wakamiya, and Y. Kanemitsu, *Optical characterization of voltage-accelerated degradation in $\text{ch}_3\text{nh}_3\text{pb}(\text{I}-\text{x})\text{Cl}_x$ perovskite solar cells*. Optics Express, 2016. **24**: p. A917-A924.
135. El-Hajje, G., C. Momblona, L. Gil-Escrig, J. Avila, T. Guillemot, J.F. Guillemoles, M. Sessolo, H.J. Bolink, and L. Lombez, *Quantification of spatial inhomogeneity in perovskite solar cells by hyperspectral luminescence imaging*. Energy & Environmental Science, 2016.
136. Stranks, S.D., V.M. Burlakov, T. Leijtens, J.M. Ball, A. Goriely, and H.J. Snaith, *Recombination kinetics in organic-inorganic perovskites: Excitons, free charge, and subgap states*. Physical Review Applied, 2014. **2**: p. 034007.
137. Wen, X., Y. Feng, S. Huang, F. Huang, Y.-B. Cheng, M. Green, and A. Ho-Baillie, *Defect trapping states and charge carrier recombination in organic-inorganic halide perovskites*. Journal of Materials Chemistry C, 2016.
138. Shockley, W. and W. Read Jr, *Statistics of the recombinations of holes and electrons*. Physical review, 1952. **87**: p. 835.

139. Shao, Y., Z. Xiao, C. Bi, Y. Yuan, and J. Huang, *Origin and elimination of photocurrent hysteresis by fullerene passivation in $\text{CH}_3\text{NH}_3\text{PbI}_3$ planar heterojunction solar cells*. *Nature communications*, 2014. **5**: p. 5784.
140. Milot, R.L., G.E. Eperon, H.J. Snaith, M.B. Johnston, and L.M. Herz, *Temperature-dependent charge-carrier dynamics in $\text{CH}_3\text{NH}_3\text{PbI}_3$ perovskite thin films*. *Advanced Functional Materials*, 2015.
141. Bothe, K., P. Pohl, J. Schmidt, T. Weber, P. Altermatt, B. Fischer, and R. Brendel. *Electroluminescence imaging as an in-line characterisation tool for solar cell production*. in *21st European Photovoltaic Solar Energy Conference, Dresden*. 2006.
142. Seeland, M., R. Rösch, and H. Hoppe, *Quantitative analysis of electroluminescence images from polymer solar cells*. *Journal of Applied Physics*, 2012. **111**: p. 024505.
143. Han, Y., S. Meyer, Y. Dkhissi, K. Weber, J.M. Pringle, U. Bach, L. Spiccia, and Y.-B. Cheng, *Degradation observations of encapsulated planar $\text{CH}_3\text{NH}_3\text{PbI}_3$ perovskite solar cells at high temperatures and humidity*. *Journal of Materials Chemistry A*, 2015. **3**: p. 8139-8147.
144. Würfel, P., *The chemical potential of radiation*. *Journal of Physics C: Solid State Physics*, 1982. **15**: p. 3967.
145. Trupke, T., P. Würfel, I. Uhlendorf, and I. Lauermann, *Electroluminescence of the dye-sensitized solar cell*. *Journal of Physical Chemistry B*, 1999. **103**: p. 1905-1910.
146. Feuerbacher, B. and P. Würfel, *Verification of a generalised planck law by investigation of the emission from GaAs luminescent diodes*. *Journal of Physics: Condensed Matter*, 1990. **2**: p. 3803.
147. Schick, K., E. Daub, S. Finkbeiner, and P. Würfel, *Verification of a generalized planck law for luminescence radiation from silicon solar cells*. *Applied Physics A*, 1992. **54**: p. 109-114.
148. Daub, E. and P. Würfel, *Ultralow values of the absorption coefficient of Si obtained from luminescence*. *Physical Review Letters*, 1995. **74**: p. 1020-1023.
149. Tress, W., N. Marinova, O. Inganäs, M. Nazeeruddin, S.M. Zakeeruddin, and M. Graetzel, *Predicting the open-circuit voltage of $\text{CH}_3\text{NH}_3\text{PbI}_3$ perovskite solar cells using electroluminescence and photovoltaic quantum efficiency spectra: The role of radiative and non-radiative recombination*. *Advanced Energy Materials*, 2014.
150. Xing, G., N. Mathews, S.S. Lim, N. Yantara, X. Liu, D. Sabba, M. Grätzel, S. Mhaisalkar, and T.C. Sum, *Low-temperature solution-processed wavelength-tunable perovskites for lasing*. *Nat Mater*, 2014. **13**: p. 476-480.
151. Green, M.A., *Do built-in fields improve solar cell performance?* *Progress in Photovoltaics: Research and Applications*, 2009. **17**: p. 57-66.
152. Li, X., X. Wang, W. Zhang, Y. Wu, F. Gao, and J. Fang, *The effect of external electric field on the performance of perovskite solar cells*. *Organic Electronics*, 2015. **18**: p. 107-112.
153. Mosconi, E., D. Meggiolaro, H. Snaith, S.D. Stranks, and F. De Angelis, *Light-induced annihilation of Frenkel defects in organo-lead halide perovskites*. *Energy & Environmental Science*, 2016.
154. Wu, X.X., M.T. Trinh, D. Niesner, H.M. Zhu, Z. Norman, J.S. Owen, O. Yaffe, B.J. Kudisch, and X.Y. Zhu, *Trap states in lead iodide perovskites*. *Journal of the American Chemical Society*, 2015. **137**: p. 2089-2096.
155. Eames, C., J.M. Frost, P.R.F. Barnes, B.C. O'Regan, A. Walsh, and M.S. Islam, *Ionic transport in hybrid lead iodide perovskite solar cells*. *Nat Commun*, 2015. **6**: p. 7497.
156. deQuilettes, D.W., W. Zhang, V.M. Burlakov, D.J. Graham, T. Leijtens, A. Osherov, V. Bulovic, H.J. Snaith, D.S. Ginger, and S.D. Stranks, *Photo-induced halide redistribution in organic-inorganic perovskite films*. *Nat Commun*, 2016. **7**: p. 11683.
157. Deng, Y., Z. Xiao, and J. Huang, *Light-induced self-poling effect on organometal trihalide perovskite solar cells for increased device efficiency and stability*. *Advanced Energy Materials*, 2015.

158. Wurfel, P., *The chemical potential of radiation*. Journal of Physics C: Solid State Physics, 1982. **15**: p. 3967.
159. Rau, U., *Reciprocity relation between photovoltaic quantum efficiency and electroluminescent emission of solar cells*. Physical Review B, 2007. **76**: p. 085303.
160. Jaramillo-Quintero, O.A., R.S. Sanchez, M. Rincon, and I. Mora-Sero, *Bright visible-infrared light emitting diodes based on hybrid halide perovskite with spiro-ometad as a hole-injecting layer*. The Journal of Physical Chemistry Letters, 2015. **6**: p. 1883-1890.
161. Wojciechowski, K., S.D. Stranks, A. Abate, G. Sadoughi, A. Sadhanala, N. Kopidakis, G. Rumbles, C.-Z. Li, R.H. Friend, and A.K.-Y. Jen, *Heterojunction modification for highly efficient organic-inorganic perovskite solar cells*. ACS nano, 2014. **8**: p. 12701-12709.
162. Wojciechowski, K., T. Leijtens, S. Siprova, C. Schlueter, M.T. Hörantner, J.T.-W. Wang, C.-Z. Li, A.K.Y. Jen, T.-L. Lee, and H.J. Snaith, *C60 as an efficient n-type compact layer in perovskite solar cells*. The Journal of Physical Chemistry Letters, 2015. **6**: p. 2399-2405.
163. Okano, M., M. Endo, A. Wakamiya, M. Yoshita, H. Akiyama, and Y. Kanemitsu, *Degradation mechanism of perovskite $\text{CH}_3\text{NH}_3\text{PbI}_3$ diode devices studied by electroluminescence and photoluminescence imaging spectroscopy*. Applied Physics Express, 2015. **8**: p. 102302.
164. Wu, B., K. Fu, N. Yantara, G. Xing, S. Sun, T.C. Sum, and N. Mathews, *Charge accumulation and hysteresis in perovskite-based solar cells: An electro-optical analysis*. Advanced Energy Materials, 2015.
165. Wu, Y., H. Shen, D. Walter, D. Jacobs, T. Duong, J. Peng, L. Jiang, Y.-B. Cheng, and K. Weber, *On the origin of hysteresis in perovskite solar cells*. Advanced Functional Materials, 2016: p. n/a-n/a.
166. Soufiani, A.M., M.J.Y. Tayebjee, S. Meyer, A. Ho-Baillie, J.S. Yun, W.R. MacQueen, L. Spiccia, M.A. Green, and Z. Hameiri, *Electro- and photoluminescence imaging as fast screening technique of the layer uniformity and device degradation in planar perovskite solar cells*. Journal of Applied Physics, 2016. **120**: p. 035702.
167. Guerrero, A., J. You, C. Aranda, Y.S. Kang, G. Garcia-Belmonte, H. Zhou, J. Bisquert, and Y. Yang, *Interfacial degradation of planar lead halide perovskite solar cells*. ACS Nano, 2016. **10**: p. 218-224.
168. Raguse, J., J.T. McGoffin, and J.R. Sites. *Electroluminescence system for analysis of defects in cdte cells and modules*. in *Photovoltaic Specialists Conference (PVSC), 2012 38th IEEE*. 2012.
169. De Bastiani, M., G. Dell'Erba, M. Gandini, V. D'Innocenzo, S. Neutzner, A.R.S. Kandada, G. Grancini, M. Binda, M. Prato, and J.M. Ball, *Ion migration and the role of preconditioning cycles in the stabilization of the j-v characteristics of inverted hybrid perovskite solar cells*. Advanced Energy Materials, 2015. **6**.
170. Tress, W., N. Marinova, T. Moehl, S. Zakeeruddin, M.K. Nazeeruddin, and M. Grätzel, *Understanding the rate-dependent j-v hysteresis, slow time component, and aging in $\text{CH}_3\text{NH}_3\text{PbI}_3$ perovskite solar cells: The role of a compensated electric field*. Energy & Environmental Science, 2015.
171. Qiu, W., T. Merckx, M. Jaysankar, C. Masse de la Huerta, L. Rakocvic, W. Zhang, U.W. Paetzold, R. Gehlhaar, L. Froyen, J. Poortmans, D. Cheyns, H.J. Snaith, and P. Heremans, *Pinhole-free perovskite films for efficient solar modules*. Energy & Environmental Science, 2016. **9**: p. 484-489.
172. Dkhissi, Y., H. Weerasinghe, S. Meyer, I. Benesperi, U. Bach, L. Spiccia, R.A. Caruso, and Y.-B. Cheng, *Parameters responsible for the degradation of $\text{CH}_3\text{NH}_3\text{PbI}_3$ -based solar cells on polymer substrates*. Nano Energy, 2016. **22**: p. 211-222.
173. Jung, M.-C., S.R. Raga, L.K. Ono, and Y. Qi, *Substantial improvement of perovskite solar cells stability by pinhole-free hole transport layer with doping engineering*. Scientific reports, 2015. **5**: p. 9863.

-
174. Galisteo-López, J.F., M. Anaya, M.E. Calvo, and H. Míguez, *Environmental effects on the photophysics of organic–inorganic halide perovskites*. The Journal of Physical Chemistry Letters, 2015. **6**: p. 2200-2205.
175. Bryant, D., N. Aristidou, S. Pont, I. Sanchez-Molina, T. Chotchunangatchaval, S. Wheeler, J.R. Durrant, and S.A. Haque, *Light and oxygen induced degradation limits the operational stability of methylammonium lead triiodide perovskite solar cells*. Energy & Environmental Science, 2016. **9**: p. 1655-1660.
176. Li, B., Y. Li, C. Zheng, D. Gao, and W. Huang, *Advancements in the stability of perovskite solar cells: Degradation mechanisms and improvement approaches*. RSC Advances, 2016. **6**: p. 38079-38091.
177. Carrillo, J., A. Guerrero, S. Rahimnejad, O. Almora, I. Zarazua, E. Mas-Marza, J. Bisquert, and G. Garcia-Belmonte, *Ionic reactivity at contacts and aging of methylammonium lead triiodide perovskite solar cells*. Advanced Energy Materials, 2016. **6**.
178. Seo, J., J.H. Noh, and S.I. Seok, *Rational strategies for efficient perovskite solar cells*. Accounts of Chemical Research, 2016. **49**: p. 562-572.
179. Yang, J. and T.L. Kelly, *Decomposition and cell failure mechanisms in lead halide perovskite solar cells*. Inorganic Chemistry, 2016.
180. Aristidou, N., I. Sanchez-Molina, T. Chotchuangchutchaval, M. Brown, L. Martinez, T. Rath, and S.A. Haque, *The role of oxygen in the degradation of methylammonium lead trihalide perovskite photoactive layers*. Angewandte Chemie International Edition, 2015. **54**: p. 8208-8212.
181. Leijtens, T., G.E. Eperon, S. Pathak, A. Abate, M.M. Lee, and H.J. Snaith, *Overcoming ultraviolet light instability of sensitized tio₂ with meso-superstructured organometal tri-halide perovskite solar cells*. Nat Commun, 2013. **4**.
182. Song, D., J. Ji, Y. Li, G. Li, M. Li, T. Wang, D. Wei, P. Cui, Y. He, and J.M. Mbengue, *Degradation of organometallic perovskite solar cells induced by trap states*. Applied Physics Letters, 2016. **108**: p. 093901.
183. Yang, J., B.D. Siempelkamp, D. Liu, and T.L. Kelly, *Investigation of ch₃nh₃pbi₃ degradation rates and mechanisms in controlled humidity environments using in situ techniques*. ACS Nano, 2015. **9**: p. 1955-1963.
184. Yang, D., W. Ming, H. Shi, L. Zhang, and M.-H. Du, *Fast diffusion of native defects and impurities in perovskite solar cell material ch₃nh₃pbi₃*. Chemistry of Materials, 2016. **28**: p. 4349-4357.
185. Zhang, Y., Y. Wang, Z.-q. Xu, J. Liu, J. Song, Y. Xue, Z. Wang, J. Zheng, L. Jiang, C. Zheng, F. Huang, B. Sun, Y.-B. Cheng, and Q. Bao, *Reversible structural swell-shrink and recoverable optical properties in hybrid inorganic-organic perovskite*. ACS Nano, 2016.
186. Hallam, B., B. Tjahjono, T. Trupke, and S. Wenham, *Photoluminescence imaging for determining the spatially resolved implied open circuit voltage of silicon solar cells*. Journal of Applied Physics, 2014. **115**: p. 044901.
187. Trupke, T., E. Pink, R. Bardos, and M. Abbott, *Spatially resolved series resistance of silicon solar cells obtained from luminescence imaging*. Applied Physics Letters, 2007. **90**: p. 093506.
188. Hahn, G., K. Krauss, F. Fertig, D. Menzel, and S. Rein, *5th international conference on silicon photovoltaics, siliconpv 2015light-induced degradation of silicon solar cells with aluminiumoxide passivated rear side*. Energy Procedia, 2015. **77**: p. 599-606.
189. Liu, Z., M. Peters, V. Shanmugam, Y.S. Khoo, S. Guo, R. Stangl, A.G. Aberle, and J. Wong, *Luminescence imaging analysis of light harvesting from inactive areas in crystalline silicon pv modules*. Solar Energy Materials and Solar Cells, 2016. **144**: p. 523-531.
190. Yamashita, D., T. Handa, T. Ihara, H. Tahara, A. Shimazaki, A. Wakamiya, and Y. Kanemitsu, *Charge injection at the heterointerface in perovskite ch₃nh₃pbi₃ solar cells*

-
- studied by simultaneous microscopic photoluminescence and photocurrent imaging spectroscopy.* The Journal of Physical Chemistry Letters, 2016. **7**: p. 3186-3191.
191. Juhl, M.K., T. Trupke, M. Abbott, and B. Mitchell, *Spatially resolved absorptance of silicon wafers from photoluminescence imaging.* IEEE Journal of Photovoltaics, 2015. **5**: p. 1840-1843.
 192. Wei, J., H. Li, Y. Zhao, W. Zhou, R. Fu, Y. Leprince-Wang, D. Yu, and Q. Zhao, *Suppressed hysteresis and improved stability in perovskite solar cells with conductive organic network.* Nano Energy, 2016. **26**: p. 139-147.
 193. Zhang, T., N. Guo, G. Li, X. Qian, and Y. Zhao, *A controllable fabrication of grain boundary pbi2 nanoplates passivated lead halide perovskites for high performance solar cells.* Nano Energy, 2016. **26**: p. 50-56.
 194. Liu, Z., P. Luo, W. Xia, S. Zhou, J. Cheng, L. Sun, c. xu, and Y.-W. Lu, *Acceleration effect of chlorine in the gas-phase growth process of ch3nh3pbi3(cl) films for efficient perovskite solar cells.* Journal of Materials Chemistry C, 2016.
 195. Chen, C., Y. Cheng, Q. Dai, and H. Song, *Radio frequency magnetron sputtering deposition of tio(2) thin films and their perovskite solar cell applications.* Scientific Reports, 2015. **5**: p. 17684.
 196. Das, S., G. Gu, P.C. Joshi, B. Yang, T. Aytug, C.M. Rouleau, D.B. Geohegan, and K. Xiao, *Low thermal budget, photonic-cured compact tio2 layers for high-efficiency perovskite solar cells.* Journal of Materials Chemistry A, 2016.
 197. Ahn, N., K. Kwak, M.S. Jang, H. Yoon, B.Y. Lee, J.-K. Lee, P.V. Pikhitsa, J. Byun, and M. Choi, *Trapped charge driven degradation of perovskite solar cells.* arXiv preprint arXiv:1604.07912, 2016.
 198. Braly, I.L. and H.W. Hillhouse, *Optoelectronic quality and stability of hybrid perovskites from mapbi3 to mapbi2br using composition spread libraries.* The Journal of Physical Chemistry C, 2016. **120**: p. 893-902.
 199. Dkhissi, Y., S. Meyer, D. Chen, H.C. Weerasinghe, L. Spiccia, Y.-B. Cheng, and R.A. Caruso, *Stability comparison of perovskite solar cells based on zinc oxide and titania on polymer substrates.* ChemSusChem, 2016. **9**: p. 687-695.
 200. Almora, O., C. Aranda, I. Zarazua, A. Guerrero, and G. Garcia-Belmonte, *Noncapacitive hysteresis in perovskite solar cells at room temperature.* ACS Energy Letters, 2016: p. 209-215.
 201. Nie, W., J.-C. Blancon, A.J. Neukirch, K. Appavoo, H. Tsai, M. Chhowalla, M.A. Alam, M.Y. Sfeir, C. Katan, J. Even, S. Tretiak, J.J. Crochet, G. Gupta, and A.D. Mohite, *Light-activated photocurrent degradation and self-healing in perovskite solar cells.* Nat Commun, 2016. **7**.
 202. Soufiani, A.M., Z. Hameiri, S. Meyer, S. Lim, M.J.Y. Tayebjee, J.S. Yun, A. Ho-Baillie, G.J. Conibeer, L. Spiccia, and M.A. Green, *Lessons learnt from spatially resolved electro- and photoluminescence imaging: Interfacial delamination in ch3nh3pbi3 planar perovskite solar cells upon illumination.* Advanced Energy Materials, 2016. **7**: p. 1602111.
 203. Xing, G., B. Wu, S. Chen, J. Chua, N. Yantara, S. Mhaisalkar, N. Mathews, and T.C. Sum, *Interfacial electron transfer barrier at compact tio2/ch3nh3pbi3 heterojunction.* Small, 2015. **11**: p. 3606-3613.
 204. Richardson, G., S. O'Kane, R.G. Niemann, T. Peltola, J.M. Foster, P.J. Cameron, and A. Walker, *Can slow-moving ions explain hysteresis in the current-voltage curves of perovskite solar cells?* Energy & Environmental Science, 2016.
 205. Merdasa, A., M. Bag, Y. Tian, E. Källman, A. Dobrovolsky, and I.G. Scheblykin, *Super-resolution luminescence microspectroscopy reveals the mechanism of photoinduced degradation in ch3nh3pbi3 perovskite nanocrystals.* The Journal of Physical Chemistry C, 2016. **120**: p. 10711-10719.
 206. Zhao, C., B. Chen, X. Qiao, L. Luan, K. Lu, and B. Hu, *Revealing underlying processes involved in light soaking effects and hysteresis phenomena in perovskite solar cells.* Advanced Energy Materials, 2015. **5**: p. n/a-n/a.

207. Zhou, Y., A.L. Vasiliev, W. Wu, M. Yang, S. Pang, K. Zhu, and N.P. Padture, *Crystal morphologies of organolead trihalide in mesoscopic/planar perovskite solar cells*. The Journal of Physical Chemistry Letters, 2015. **6**: p. 2292-2297.
208. Meloni, S., T. Moehl, W. Tress, M. Franckevicius, M. Saliba, Y.H. Lee, P. Gao, M.K. Nazeeruddin, S.M. Zakeeruddin, U. Rothlisberger, and M. Graetzel, *Ionic polarization-induced current-voltage hysteresis in $\text{CH}_3\text{NH}_3\text{PbX}_3$ perovskite solar cells*. Nat Commun, 2016. **7**.
209. Azpiroz, J.M., E. Mosconi, J. Bisquert, and F. De Angelis, *Defect migration in methylammonium lead iodide and its role in perovskite solar cell operation*. Energy & Environmental Science, 2015. **8**: p. 2118-2127.
210. Mosconi, E. and F. De Angelis, *Mobile ions in organohalide perovskites: Interplay of electronic structure and dynamics*. ACS Energy Letters, 2016: p. 182-188.
211. Levine, I., P.K. Nayak, J.T.-W. Wang, N. Sakai, S. Van Reenen, T.M. Brenner, S. Mukhopadhyay, H.J. Snaith, G. Hodes, and D. Cahen, *Interface-dependent ion migration/accumulation controls hysteresis in MAPbI_3 solar cells*. The Journal of Physical Chemistry C, 2016.
212. Yuan, Y. and J. Huang, *Ion migration in organometal trihalide perovskite and its impact on photovoltaic efficiency and stability*. Accounts of Chemical Research, 2016. **49**: p. 286-293.
213. Yun, J.S., J. Seidel, J. Kim, A.M. Soufiani, S. Huang, J. Lau, N.J. Jeon, S.I. Seok, M.A. Green, and A. Ho-Baillie, *Critical role of grain boundaries for ion migration in formamidinium and methylammonium lead halide perovskite solar cells*. Advanced Energy Materials, 2016: p. n/a-n/a.
214. Yuan, Y., J. Chae, Y. Shao, Q. Wang, Z. Xiao, A. Centrone, and J. Huang, *Photovoltaic switching mechanism in lateral structure hybrid perovskite solar cells*. Advanced Energy Materials, 2015.
215. Huang, F., L. Jiang, A.R. Pascoe, Y. Yan, U. Bach, L. Spiccia, and Y.-B. Cheng, *Fatigue behavior of planar $\text{CH}_3\text{NH}_3\text{PbI}_3$ perovskite solar cells revealed by light on/off diurnal cycling*. Nano Energy, 2016. **27**: p. 509-514.
216. Li, W., W. Zhang, S. Van Reenen, R.J. Sutton, J. Fan, A.A. Haghighirad, M.B. Johnston, L. Wang, and H.J. Snaith, *Enhanced uv-light stability of planar heterojunction perovskite solar cells with caesium bromide interface modification*. Energy & Environmental Science, 2016. **9**: p. 490-498.
217. Yuan, Y., Q. Wang, Y. Shao, H. Lu, T. Li, A. Gruverman, and J. Huang, *Electric-field-driven reversible conversion between methylammonium lead triiodide perovskites and lead iodide at elevated temperatures*. Advanced Energy Materials, 2015: p. n/a-n/a.
218. Shao, Y., Y. Fang, T. Li, Q. Wang, Q. Dong, Y. Deng, Y. Yuan, H. Wei, M. Wang, A. Gruverman, J. Shield, and J. Huang, *Grain boundary dominated ion migration in polycrystalline organic-inorganic halide perovskite films*. Energy & Environmental Science, 2016. **9**: p. 1752-1759.
219. Li, C., S. Tscheuschner, F. Paulus, P.E. Hopkinson, J. Kießling, A. Köhler, Y. Vaynzof, and S. Huettnner, *Iodine migration and its effect on hysteresis in perovskite solar cells*. Advanced Materials, 2016. **28**: p. 2446-2454.
220. Bae, S., S. Kim, S.-W. Lee, K.J. Cho, S. Park, S. Lee, Y. Kang, H.-S. Lee, and D. Kim, *Electric-field-induced degradation of methylammonium lead iodide perovskite solar cells*. The Journal of Physical Chemistry Letters, 2016: p. 3091-3096.
221. Mosconi, E., D. Meggiolaro, H.J. Snaith, S.D. Stranks, and F. De Angelis, *Light-induced annihilation of frenkel defects in organo-lead halide perovskites*. Energy & Environmental Science, 2016. **9**: p. 3180-3187.
222. Domanski, K., B. Roose, T. Matsui, M. Saliba, S.-H. Turren-Cruz, J.-P. Correa-Baena, C.R. Carmona, G. Richardson, J.M. Foster, F. De Angelis, J.M. Ball, A. Petrozza, N. Mine, M.K. Nazeeruddin, W. Tress, M. Gratzel, U. Steiner, A. Hagfeldt, and A. Abate, *Migration of cations induces reversible performance losses over day/night cycling in perovskite solar cells*. Energy & Environmental Science, 2017.

-
223. Jacobs, D.A., Y. Wu, H. Shen, C. Barugkin, F.J. Beck, T.P. White, K. Weber, and K.R. Catchpole, *Hysteresis phenomena in perovskite solar cells: The many and varied effects of ionic accumulation*. Physical Chemistry Chemical Physics, 2017.
224. Minns, J.L., P. Zajdel, D. Chernyshov, W. van Beek, and M.A. Green, *Structure and interstitial iodide migration in hybrid perovskite methylammonium lead iodide*. Nature Communications, 2017. **8**: p. 15152.
225. Lopez-Varo, P., L. Bertoluzzi, J. Bisquert, M. Alexe, M. Coll, J. Huang, J.A. Jimenez-Tejada, T. Kirchartz, R. Nechache, F. Rosei, and Y. Yuan, *Physical aspects of ferroelectric semiconductors for photovoltaic solar energy conversion*. Physics Reports.
226. Green, M.A. and J. Shewchun, *Current multiplication in metal-insulator-semiconductor (mis) tunnel diodes*. Solid-State Electronics, 1974. **17**: p. 349-365.
227. Green, M.A., *Depletion region recombination in silicon thin-film multilayer solar cells*. Progress in Photovoltaics: Research and Applications, 1996. **4**: p. 375-380.
228. Pockett, A., G.E. Eperon, N. Sakai, H.J. Snaith, L.M. Peter, and P.J. Cameron, *Microseconds, milliseconds and seconds: Deconvoluting the dynamic behaviour of planar perovskite solar cells*. Physical Chemistry Chemical Physics, 2017. **19**: p. 5959-5970.
229. Wang, F., J. Ma, F. Xie, L. Li, J. Chen, J. Fan, and N. Zhao, *Organic cation-dependent degradation mechanism of organotin halide perovskites*. Advanced Functional Materials, 2016: p. n/a-n/a.
230. Sutton, R.J., G.E. Eperon, L. Miranda, E.S. Parrott, B.A. Kamino, J.B. Patel, M.T. Hörantner, M.B. Johnston, A.A. Haghighirad, D.T. Moore, and H.J. Snaith, *Bandgap-tunable cesium lead halide perovskites with high thermal stability for efficient solar cells*. Advanced Energy Materials, 2016. **6**: p. n/a-n/a.